Acoustic charge manipulation in semiconductor nanostructures for optical applications

Stefan Völk
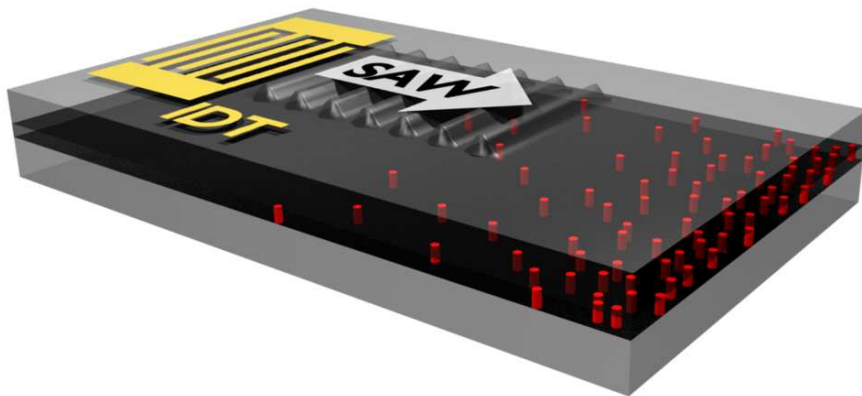
Abstract

Within this thesis, the influence of a surface acoustic wave (SAW) on the luminescence of semiconductor nanostructures is investigated. The main intention of this thesis is to use SAWs, in order to acoustically trigger the luminescence of a single quantum dot (QD) structure.

Beginning with the physics of low-dimensional semiconductor structures, the quantum mechanical and optical properties of QD systems are discussed. In particular, intrinsic parameters of QDs such as morphology, composition, strain and occupation with carriers are taken into account. Subsequently, the influence of an applied electric field and externally induced strain are introduced. From this general approach, the discussion is focused to quantum posts (QPs) which are columnar shaped semiconductor nanostructures. In contrast to conventional self-assembled QDs, the height of the QPs can be controlled by the epitaxial growth process. Due to the adjustable height, electronic states and therefore the exciton transition energies can be tailored. Furthermore, QPs are embedded in a matrix-quantum-well structure which has important influence on the carrier dynamic if a SAW is excited on the sample.

In order to characterize the optical properties of single QPs, photoluminescence (PL) spectra are measured under different excitation schemes. A single QP shows several PL lines which correspond to particular exciton transitions. Since the intensities of these lines depend on the applied laser power, laser intensity series are helpful to assign the different PL lines to particular exciton states. Additional information is obtained from different excitation schemes (cw and pulsed laser) and by comparing typical PL energies with theoretical models and earlier experiments on similar structures.

SAWs are used in this work in order to manipulate the PL emission of semiconductor structures. A SAW is a mechanical wave propagating on the surface of a substrate. On piezoelectric substrates, such as GaAs, SAWs can be excited using interdigital transducers (IDTs). The IDT efficiency depends particularly on the geometrical design parameters of these planar lithographically fabricated metal contacts. These parameters are optimized using an analytical model in order to improve the transducer efficiency.

Mainly, two effects have to be considered regarding the interaction of charge carriers with SAWs. The first effect is called deformation potential coupling

and takes into account the deformation of the crystal lattice which alters the band gap of semiconductors. The deformation potential of a SAW gives rise to a type I band modulation. The second effect induced by a SAW is acousto-electric coupling and takes into account the piezoelectric field. For the used SAW frequencies, acousto-electric coupling dominates the interaction between charges and SAW. In contrast to the deformation potential, a type II modulation is observed. The dynamic acousto-electric band modulation can be used to dissociate excitons and subsequently impede radiative recombination. For a quantum well (QW) structure, the periodic type II band modulation dissociates excitons into sequential stripes of electrons and holes which then are conveyed by the SAW. This so called bipolar transport or charge conveyance effect can be used to inject carriers into remote QD structures and has already been demonstrated for QD ensembles.

The semiconductor nanostructures are studied with a low temperature μ-PL setup allowing for time-integrated and spectrally resolved luminescence measurements. Apart from spectral measurements, spatial resolution and a combination of spatial and spectral resolution can be achieved. Temporally resolved PL data is obtained by synchronizing the trigger of a pulsed laser with the frequency of the SAW. This so-called phase locking method offers multi-channel detection and is highly sensitive, since the same detector can be used as for time-integrated measurements.

In the experimental part of this thesis, two configurations are used. For direct excitation, the laser focus and the studied nanostructure are aligned, whereas for remote excitation, the position of the nanostructure is outside of the laser focus. In the case of the QP sample, a quenching behaviour is observed for the matrix-QW luminescence. Then, the luminescence of individual QPs is investigated with SAWs applied. Surprisingly, a switching of PL lines is observed which cannot be obtained by varying other parameters, e.g. the laser intensity. This switching behaviour sets in at a well-defined critical SAW power.

Since the SAW induces a bipolar charge transport within the surrounding QW-matrix, a SAW driven carrier capture process from the matrix into the post is assumed. Some structures on the QP sample show an unusual line splitting behaviour which is probably attributed to dot-like structures. Finally, the QP system is compared with conventional self-assembled QDs. A pronounced hysteresis is observed for a single QD when the SAW power is increased and subsequently decreased, whereas the QP luminescence has a non-hysteretic characteristic. The different experimental observations are explained by the widths of the 2-dimensional layers to which the nanostructures are coupled. The matrix-QW of the QP sample is relatively wide compared to the thin wetting layer of the QD sample giving rise to different carrier mobilities within these structures.

The matrix-QW and individual QP luminescence is detected temporally resolved using phase locking. For an entire SAW cycle, both signals show a $\Delta\phi = 2\pi$ modulation in intensity which is not expected if electrons and holes

are comparably influenced by the piezoelectric field of a SAW. However, the different effective masses and mobilities of electrons and holes introduce an asymmetry which could explain the modulation period.

Due to the enhanced carrier mobilities in the matrix-QW compared to the wetting layer of QD structures, QP systems are suited for experiments showing charge conveyance over macroscopic distances and remote carrier injection into single nanostructures. Within this work, remote carrier injection into individual QPs is successfully demonstrated for the first time. This is supported by spatially and spectrally resolved PL measurements. For both configurations, direct and remote excitation, SAW power series are performed measuring the luminescence of the same QP. For power levels above the critical SAW power, identical PL lines are observed in both configurations which confirms the crucial role of the 2-dimensional matrix-QW for SAW assisted PL switching.

Finally, spatially resolved measurements are provided, showing both luminescence from the locally excited matrix-QW and from remotely injected QPs. A stripe pattern is observed for the QW luminescence. The period of the observed stripes corresponds to a half SAW wavelength. Since this kind of experiment is performed under continuous wave (cw) operation of the SAW, the observed period can be explained by standing acoustic waves which probably arise due to reflections caused by a second IDT.

Contents

8

Introduction

Photons are the quanta of light [20]. The control and generation of single photons are attractive for future applications in quantum cryptography [7], teleportation [11] and quantum computing [37]. Quantum algorithms take advantage of the quantum mechanical properties of particles involved in such processes. Whereas a classical bit can only encode the two states 0 and 1, a quantum computer uses the superposition of quantum mechanical states, a so-called quantum bit (qubit). A qubit can be realized in principle by any system with two defined quantum states $|\,0\rangle$ and $|\,1\rangle$, provided that the time consumed for the quantum operation is much shorter than the decoherence time of the system. For an optical approach, the individual qubits are represented by different polarization states. Compared to other approaches such as spins and charges, photons interact weakly with the environment which allows for long decoherence times and their transmission over long distances, for example using optical fibers.

Key requirements for photon based quantum algorithms are reliable and efficient single photon sources (SPS) and sources of entangled photon pairs [47]. An ideal SPS provides single photon states on demand and in response to an external trigger. Furthermore, these photons should be indistinguishable. Various approaches have been realized with their own advantages and disadvantages. Figure 1 illustrates three prominent systems.

Atoms of a given isotope are exactly indistinguishable. Using single atoms or ions as SPSs is therefore a quite elemental approach and was realized the first time in the late seventies of the last century [35]. However, the experimental setups required for trapping and observing single atoms or ions are rather bulky. For larger setups involving many qubits, this approach is no longer practicable. Another very promising implementation of SPSs are single defects in crystals.
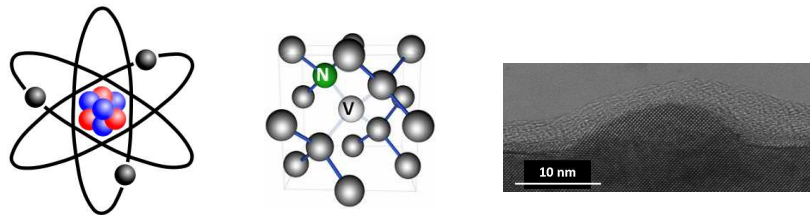

Figure 1: Systems for the realization of single photon sources: Single atoms, single defects and semiconductor quantum dots.

Mainly nitrogen-vacancy centers in diamond have been investigated [43]. The defects are very stable and devices with large numbers of positioned defects could in principle be fabricated. On the other hand, the maximum single photon emission rate is limited by the relatively long radiative lifetimes of the order of $\tau = 10$ ns and an integration into existing single device structures is difficult to achieve.

SPS have also been demonstrated using individual semiconductor quantum dots (QD) [52]. In QDs, lower bandgap material is embedded into a matrix of higher bandgap material. Although a semiconductor QD typically consists of about 10^3 to 10^6 lattice atoms, this kind of structure can be considered as an "artificial atom" since the combination of different bandgap materials gives rise to quantized states which can be occupied by charges similar to atoms. A main advantage of this approach is the implementation in semiconductor systems compatible with existing optoelectronics and fiber-based communication networks. Furthermore, the radiative quantum efficiency is very high and carriers can be injected electrically. To date, the generation of single photons out of QDs is only possible at low temperatures. Due to the high refraction index of these materials, the photon extraction remains also a challenge. Several types of semiconductor QDs have been realized. The most extensively investigated and most prominent systems are self-assembled InGaAs QDs.

Related to QDs are so-called quantum posts (QP), in literature also known as closely stacked QDs, quantum rods or columnar shaped QDs [31]. Their optical properties are similar to self assembled InGaAs QDs, but their geometrical shape is not. By successively growing InAs and GaAs layers, a stack of QDs can be achieved changing the aspect ratio of the entire structure and resulting in an additional degree of freedom in vertical direction. By applying an electric field toward the opposite ends of the QPs, excited carriers can be separated within these structures and after a defined time the controlled emission of photons can be induced by switching the electric field [40].

Instead of applying static electric fields to semiconductor nanostructures, a different approach is investigated. Surface acoustic waves (SAW) allow for applying high electric fields to the optically active area without any contacts and with high operation rates. The contactless operation circumvents experimental difficulties involved with contacting the sample surface such as undefined charging and screening effects, poor light extraction and high capacitances of the contacts. Additionally, SAWs can be used to convey charge carriers over macroscopic distances giving rise to an additional possibility of manipulating charge carriers [63].

This thesis is organized as follows:

- In chapter 1, the fundamental properties of semiconductor QDs are reviewed. Particularly, the influence of inherent parameters such as shape, composition and strain are explained. Furthermore, few particle interactions are taken into account. The fabrication of QD structures is generally described and extended to QPs which have mainly been investigated in this work. Then, the optical properties of these structures and the influence of external parameters such as applied electric field and mechanical strain are described.

- Chapter 2 summarizes the basic properties of SAWs and their generation through IDTs. This chapter points out the possible interaction mechanisms between SAWs and charges in the semiconductor structures. Basically, two effects are observed, the so-called deformation potential coupling and acousto-electric coupling. The latter accounts for a lateral type II band modulation within QW structures which can be used for charge conveyance and remote carrier injection into 0-dimensional structures.

- Chapter 3 describes the experimental setup which has been used for PL spectroscopy. The setup allows also for spatial and temporal resolution. For the temporally resolved measurements, the SAW and the pulsed laser are synchronized resulting in a stroboscopic excitation of the sample (phase locking).

- In chapter 4, the luminescence originating from individual nanostructures is investigated with SAWs applied. The luminescence of the matrix-QW surrounding the QPs quenches. Single QPs show a switching behaviour, i.e. a SAW induces a redistribution of luminescence from PL lines with lower energy to transitions with higher energy. The lines of some nanostructures show an extraordinary splitting behaviour. One section of this chapter compares the optical properties of QPs with those of conventional self-assembled QDs. For both structures, the SAW power is increased and subsequently decreased. In contrast to the QP sample, a hysteretic behaviour is found for the QD and wetting layer luminescence. Using phase locking, the PL of an individual QP and of the matrix-QW are temporally and spectrally monitored. Both PL signals show a modulation period which corresponds to the frequency of the SAW. Finally, SAW assisted remote carrier injection into individual QPs is demonstrated for the first time and spatial PL measurements are provided revealing the "footprints" of SAWs.

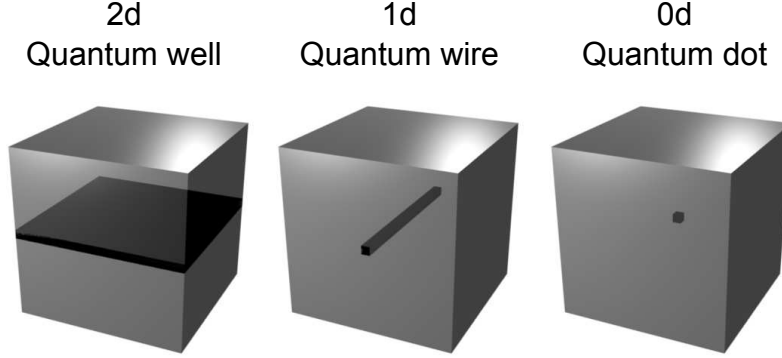# Chapter 1

Quantum dots and posts

Figure 1.1: Illustration of low-dimensional heterostructures. The numbers correspond to degrees of freedom D_f.

1.1   Low-dimensional semiconductor structures

The experimentally investigated self-assembled QDs and QPs are semiconductor structures of reduced dimensionality. Such structures can be fabricated by molecular beam epitaxy (MBE) allowing for epitaxial growth of different materials of the same crystal structure. The reduced dimensionality of these heterostructures gives rise to unique electronic and optical properties. In the following, general quantum mechanical properties are described.

From a quantum mechanical point of view, the energy states and solutions of the wave functions of a QD or QP can be achieved by successively reducing the dimensions of a semiconductor system. Table 1.1 overviews the basic dimensionalities possible in semiconductor systems. It is more common to label reduced dimensionality systems by the remaining degrees of freedom D_f than by the number of confined directions D_c.

Table 1.1: Number of confined directions D_c and number of degrees of freedom D_f for the four dimensionality systems.

System	D_c	D_f
Bulk	0	3
Quantum well	1	2
Quantum wire	2	1
Quantum dot	3	0

In order to evaluate the energy states of the low-dimensionality systems, the time-independent Schrödinger equation has to be solved. To simplify, we first calculate the solutions for one particle (electron), neglect anisotropy of the semiconductor and restrict ourselves to infinite barriers. The Schrödinger equation in space coordinates reads:

$$-\frac{\hbar^2}{2m^*}\nabla^2\Psi + V = E\Psi \tag{1.1}$$

where m^* is the effective mass of the electron. For a bulk semiconductor the potential V equals zero. Thus, the energy solutions take a parabolic form and all energy states are distributed continuously.

$$E = \frac{\hbar^2 k^2}{2m^*} \tag{1.2}$$

For a **quantum well** of width l_z, the potential V and the eigenvalues of the Schrödinger equation 1.1 within the well are:

$$
\begin{aligned}
V(x,y,z) &= V(z) \\
V(z) &= \begin{cases} 0 & \text{for} -\frac{l_z}{2} \leq z \leq +\frac{l_z}{2} \\ \infty & \text{else} \end{cases} \\
E_z &= \frac{\hbar^2 \pi^2}{2m^*} \frac{n_z^2}{l_z^2}
\end{aligned}
\tag{1.3}
$$

where n_z is an integer number. If the dimensionality of the system is further reduced, the outcome is a **quantum wire** (figure 1.1). The potential V of a rectangular infinite quantum wire and the corresponding eigenvalues of the Schrödinger equation read:

$$
\begin{aligned}
V(x,y,z) &= V(y,z) \\
V(y,z) &= \begin{cases} 0 & \text{for} -\frac{l_y}{2} \leq y \leq +\frac{l_y}{2} \\ & \wedge -\frac{l_z}{2} \leq z \leq +\frac{l_z}{2} \\ \infty & \text{else} \end{cases} \\
E_{y,z} &= \frac{\hbar^2 \pi^2}{2m^*} \left(\frac{n_y^2}{l_y^2} + \frac{n_z^2}{l_z^2} \right)
\end{aligned}
\tag{1.4}
$$

Removing all three degrees of freedom D_f, the strongest confinement is achieved. In the simplest approximation, the system is called a **quantum box** or **cuboid quantum dot** with potentials and energies analogous to the 2-dimensional and 1-dimensional systems:

$$
\begin{aligned}
V(x,y,z) &= V(x,y,z) \\
V(x,y,z) &= \begin{cases} 0 & \text{for} -\frac{l_x}{2} \leq x \leq +\frac{l_x}{2} \\ & \wedge -\frac{l_y}{2} \leq y \leq +\frac{l_y}{2} \\ & \wedge -\frac{l_z}{2} \leq z \leq +\frac{l_z}{2} \\ \infty & \text{else} \end{cases} \\
E_{x,y,z} &= \frac{\hbar^2 \pi^2}{2m^*} \left(\frac{n_x^2}{l_x^2} + \frac{n_y^2}{l_y^2} + \frac{n_z^2}{l_z^2} \right)
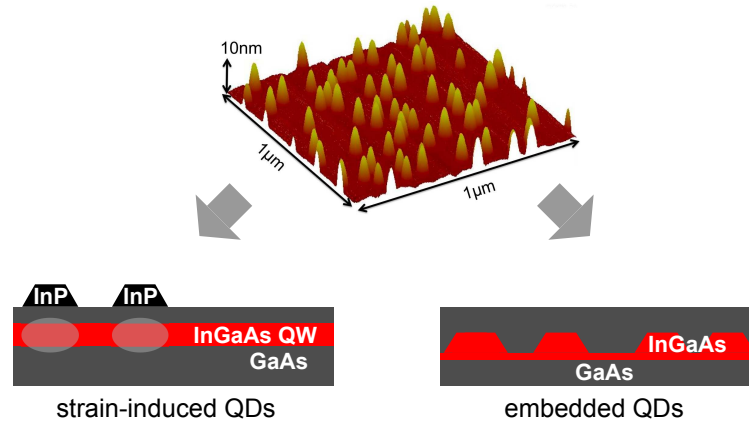\end{aligned}
\tag{1.5}
$$

Figure 1.2: Upper picture: AFM image of self-assembled QDs. Lower left: Strain induced QDs, InP stressor dots on top of the QW structure give rise to locally lowered potentials in the QW beneath. Lower right: Self-assembled embedded QDs, fabricated by an additional deposition of GaAs on top of the QD layer.

1.2   Growth of QD systems

A common technique for the fabrication of QD systems is molecular beam epitaxy (MBE). For the epitaxy process, an ultra-high vacuum chamber is necessary. The epitaxy material is evaporated in effusion cells and deposited on a substrate. Thereby, the epitaxy material is aligned in molecular beams which can be opened or interrupted by mechanical shutters allowing for a controlled deposition of different materials and in a designated sequence. With the MBE technique even individual atomic layers can be deposited. The growth rate is monitored using in-situ techniques, e.g. RHEED (reflection high energy electron diffraction). By heating or cooling the substrate, additional control of the growth process is obtained. Very often, the substrate is mounted on a rotatable plate in order to avoid inhomogeneous growth. Vice versa, by switching off the rotation, a growth gradient along the substrate is achieved.

For the fabrication of self-assembled QDs, very frequently Stranski-Krastanow growth is used [76]. This growth mode follows a two step process. Initially, the adsorbate grows as a complete film on the substrate. Due to lattice mismatch of the deposited material and the substrate, the strain of the structure increases. Starting from a critical thickness of the deposited film, the formation of little islands is energetically preferred to a growth of a continuous film. The upper picture in figure 1.2 shows an AFM image of these so-called self-assembled QDs. In the lower pictures of figure 1.2, two prominent types of self-assembled QDs are displayed. The right picture shows self-assembled embedded QDs. This configuration is obtained by additionally growing a capping layer on top of the QD layer. Then, the material with lower band gap (InGaAs) is embedded in a matrix of higher band gap (GaAs). On the left side, strain-induced QDs are depicted [50]. Here, charges are not confined due to the lower band gap material, but via the strain which is introduced by InP islands on top of the

structure. The strain locally lowers the energetic potential within a surface-near InGaAs/GaAs QW leading to a 0-dimensional confinement of carriers. In both examples, the QDs are coupled to a 2-dimensional layer, which is a QW in the case of strain-induced QDs and a so-called wetting layer (WL) in the case of the embedded QDs.

1.3 Lens shaped quantum dot

For a realistic treatment of self-assembled QDs within a theoretical model, the geometric shape of the dot has to be considered. The quantum mechanical solutions achieved by the quantum box model are only approximations to realistic QDs. Several geometries taking into account finite barriers have been proposed. The most prominent are spherical [28], pyramidal [13, 14, 16, 26] and lens shaped [29] QDs.

Depending on the material system and particular growth conditions, one of these models might be suitable. For self-assembled InGaAs QDs, often the lens shaped geometry is considered. A parabolic confinement potential in both directions x and y is assumed, whereas for the z-direction (growth direction), a box like potential is used. The height of a QD is usually $d_{\mathrm{QD}} < 5$ nm whereas the diameter is $D_{\mathrm{QD}} > 10$ nm. Hence, the z-quantization is larger than the lateral quantization. Therefore, higher bound eigenstates in z-direction are usually neglected and the problem reduces to a 2-dimensional harmonic oscillator with electronic energies E_{lm}^{e} and angular momenta L_{lm}^{e}:

$$
\begin{aligned}
E_{lm}^{\mathrm{e}} &= \Omega_+^{\mathrm{e}}(l + \frac{1}{2}) + \Omega_-^{\mathrm{e}}(m + \frac{1}{2}) & (1.6)\\
L_{lm}^{\mathrm{e}} &= l - m & (1.7)\\
& & (1.8)
\end{aligned}
$$

where $\Omega_{+/-}^{\mathrm{e}}$ are the oscillator energies of an electron. In a single band effective mass approximation the energy eigenstates of a hole can be described analogous to the electron eigenstates by substituting the electron oscillator energies with the hole energies $\Omega_{+/-}^{\mathrm{h}}$. The angular momentum of the hole $L_{lm}^{\mathrm{h}} = -L_{lm}^{\mathrm{e}}$ is opposite to the momentum of the electron. Thus, the eigenstates of electrons and holes are fully defined by their quantum numbers l and m which correspond to the motion in the two spatial directions x and y. According to atom physics, a shell notation is introduced. Beginning with the lowest oscillator energy, the QD is in the s-shell configuration (shell index $n = 1$) if both quantum numbers l and m equal zero. For the p-shell, there exist two combinations $lm = 01$ and $lm = 10$. Including the spin states of electrons and holes and Pauli exclusion principle, the total degeneracy of each shell is $2n$. The situation is sketched schematically in figure 1.3 for conduction and valence band. Due to selection rules, optical transitions are only possible for identical principle quantum numbers lm for electrons and holes which is indicated by vertical arrows in figure 1.3.
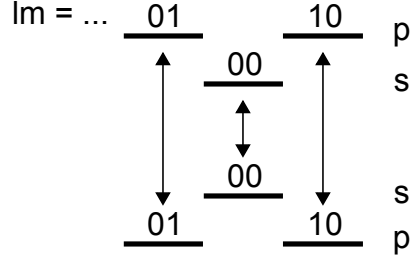
Figure 1.3: Energy level diagram of a two shell quantum dot. The quantum numbers *lm* fully define the electron and hole eigenstates. Additionally, s- and p-shells are denoted. Arrows indicate optically allowed transitions.

For the calculation of transition energies, not only the single particle states are important, i.e. the eigenvalues of the Schrödinger equation. Furthermore, the occupation of the dot by charges must be considered.

1.4   Few particle interactions

Since a QD is a structure of reduced dimensionality, the interaction of trapped charges becomes stronger than in bulk materials. Coulomb and exchange interaction give rise to additional terms in the Hamiltonian and finally to optical transitions which are shifted with respect to the single particle states. In this section, a short overview of the different occupation schemes is given.

When the quantum mechanical eigenstates of a QD are occupied by charge carriers, the interaction of these charges is included by additional terms in the resulting Hamiltonian [29]:

$$
\begin{aligned}
H &= \sum_i E_i^{\mathrm{e}} c_i^+ c_i + \sum_i E_i^{\mathrm{h}} d_i^+ d_i - \sum_{ijkl} \langle ij \mid V_{\mathrm{eh}} \mid kl \rangle c_i^+ d_j^+ d_k c_l \qquad (1.9) \\
&+ \frac{1}{2} \sum_{ijkl} \langle ij \mid V_{\mathrm{ee}} \mid kl \rangle c_i^+ c_j^+ c_k c_l + \frac{1}{2} \langle ij \mid V_{\mathrm{hh}} \mid kl \rangle d_i^+ d_j^+ d_k d_l
\end{aligned}
$$

where i, j, k, l are composite indices consisting of the fundamental quantum numbers of one particle, i.e. $i = [l, m, \sigma]$. c_i^+ and d_i^+ (c_i and d_i) are the creation (annihilation) operators for electrons and holes, respectively. $E_i^{\mathrm{e/h}}$ are the electron/hole single particle energies (equation 1.6) and V_{xy} the inter-particle interactions. It should be noted that the operators V_{xy} mediate both direct Coulomb interaction and exchange interaction which becomes important as electrons and holes are particles with spin $\frac{1}{2}$. By solving the Schrödinger equation including the Hamiltonian 1.9, the eigenstates are obtained.

Starting with a configuration of one electron and one hole occupying the QD, the eigenenergy of the system is:

$$
E_{\mathrm{s}}^0 = \Omega^{\mathrm{e}} + \Omega^{\mathrm{h}} - \langle 00; 00 \mid V_{\mathrm{e,h}} \mid 00; 00 \rangle \qquad (1.10)
$$

The first two terms correspond to the single particle energies, and the third term expresses the mutual Coulomb attraction between electron and hole. The attractive interaction between both species results in an extra binding energy $E_\mathrm{b} = \langle 00; 00 \mid V_\mathrm{e,h} \mid 00; 00 \rangle$ and the electron-hole complex is called an *exciton.*

If the exciton recombines, a photon is emitted. The energy of this photon E corresponds to the energy of the excitonic state. Therefore, excitons occupying a QD system, can be studied by analyzing the emitted light. In a *photoluminescence* (PL) experiment, the structure is first excited by (laser) light. The energy of the incoming light has to be high enough, in order to excite the particular states. If the laser energy is exactly the energy of the studied transition, then the excitation scheme is called *resonant.* For higher excitation energies, first *hot* carriers are generated. These carriers are scattered by diverse physical mechanisms and relax to particular excitonic states. After the relaxation processes, a spontaneous radiative recombination becomes possible giving rise to the emission of luminescence light which can be studied via spectroscopic techniques.

1.4.1 Neutral exciton complexes

In the following, various scenarios of exciton occupation of QDs are discussed. First, the QD is assumed to be occupied by the same number of electrons and holes. That is a charge neutral configuration. Assuming an initial state of N excitons, the QD system reaches a state of $N - 1$ excitons if one exciton recombines and one photon is emitted. Then, the final state is again in a neutral configuration. The energy values of initial and final states result from the Schödinger equation 1.1 and the probabilities of possible transitions are calculated by Fermi's golden rule:

$$S_N(\omega) = \sum_f \mid \langle N - 1, f \mid P^- \mid i, N \rangle \mid^2 \cdot \delta(E_N^i - E_{N-1}^f - \hbar\omega) \qquad (1.11)$$

where $P^- = \sum_i d_i c_i$ is the polarization operator which annihilates an electron-hole pair and creates a photon. i and f correspond to the initial and final state of the QD. Bayer et. al. calculated the eigenenergies and the transition probabilities for different neutral exciton occupations [6] as a function of the excitation power P_L (left panel of figure 1.4). For low excitation power P_L, only one transition is observed which corresponds to a single exciton $1X^0$ occupying the lowest bound eigenstate in the s-shell. This is also observed experimentally, as shown in the spectral data in the right panel of figure 1.4. For the lowest excitation power, only a single line is apparent.

When P_L is increased, the s-shell is completely filled and the biexciton $2X^0$ state is prepared which is observed in the experimental and calculated data of figure 1.4 showing a second line close to the $1X^0$ state. Compared to the $1X^0$ exciton, additional Coulomb interactions have to be taken into account. Thus, the energy of the corresponding biexciton decay is shifted relatively to the single
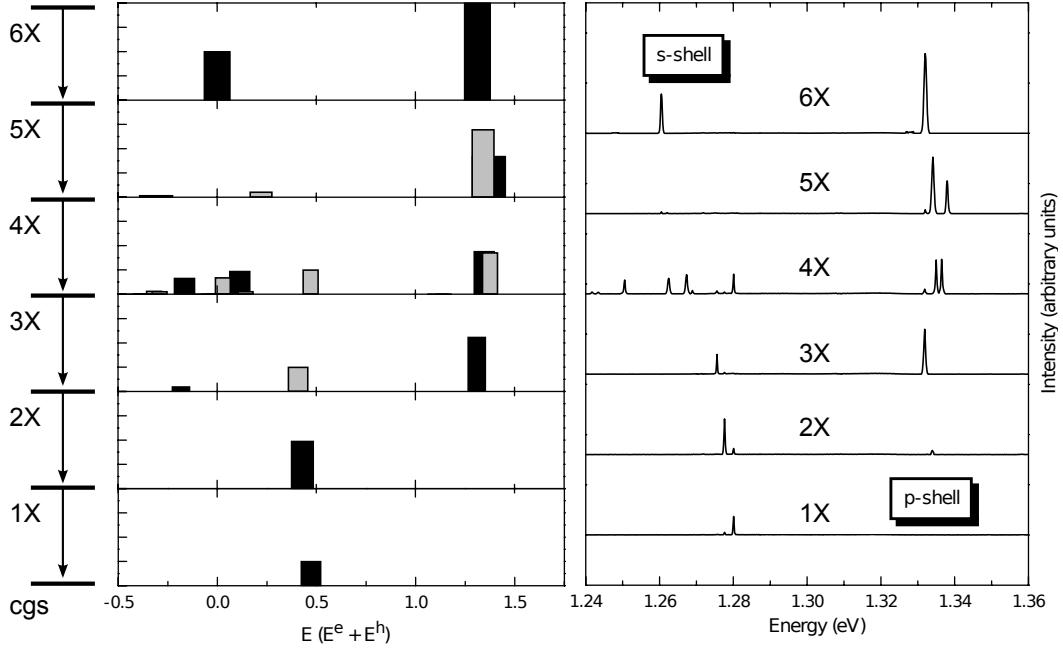
Figure 1.4: Emission spectra of an InGaAs QD as a function of excitation power. Left: calculated transition energies and probabilities of neutral exciton complexes. The heights of the columns encode the transition probability. Black (grey) columns indicate transitions to singlet (triplet) states. Right: measured spectra of a single InGaAs QD as excitation power is increased successively. Reproduced after [6].

exciton transition. The absolute value of the biexciton transition depends on many parameters such as quantum mechanical confinement and effective masses of electrons and holes, but in the resulting spectra only one biexciton line is apparent as in the case of a single exciton (see figure 1.4). For QDs, the biexciton line is typically shifted $\Delta E = 2.5$ meV towards lower energies. This value is enhanced compared to the biexciton binding energies in QWs ($E_b \approx 1$ meV) and in bulk material ($E_b \approx 0.13$ meV) because of the stronger confinement [45].

When the QD is occupied by more than two excitons, the corresponding spectra show various lines. Furthermore, exchange interaction due to electronic spin states has to be considered. Depending on the recombination order, the final state forms either a singlet or a triplet. Exchange interaction lifts the degeneracy resulting in different spectral lines, as indicated by black and grey columns in the left panel of figure 1.4. A well known characteristic of PL emission from individual QDs is the cascaded exciton recombination. As depicted in the schematic on the left side of figure 1.4, first the $6X$ exciton recombines, then the $5X$ exciton and so on. At the end of this cascade, the $1X$ exciton recombines leaving the crystal ground state (cgs).
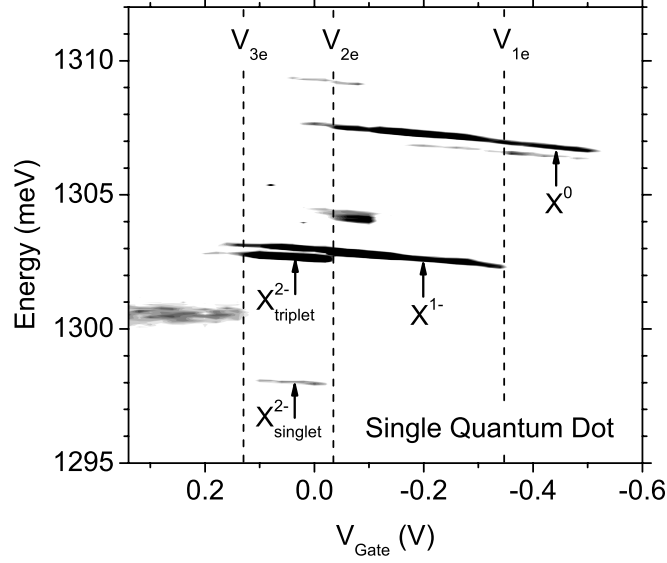
Figure 1.5: Charged exciton emission from a single QD. For increasing gate voltage, electrons are controllably added giving rise to the emission of neutral (X^0), singly (X^{1-}) and doubly negatively (X^{2-}) charged excitons. Reproduced after [22].

1.4.2 Charged excitons

If the number of electrons and holes occupying a QD is not equal, the QD is in a charged exciton state. Such states can be prepared in electric field tunable QDs or in QD systems where the capture probabilities of electrons and holes are distinct. Figure 1.5 shows a photoluminescence experiment performed on a single self-assembled InGaAs QD embedded in charge-tunable n-i Schottky diode. For large reverse bias $V < V_1$, a single emission line from the X^0 exciton is observed. As the reverse voltage is decreased, emission from a singly negatively charged exciton X^{1-} is observed. For gate voltages $V_2 < V < V_3$, the original X^0 line vanishes and two new lines denoted as X^{2-}_{singlet} and X^{2-}_{triplet} appear in the spectrum. In these types of experiments, charged exciton complexes are prepared depending on an applied voltage. For a n-i diode device, electrons are injected from the n-contact giving rise to the preferential emission of negatively charged complexes. Emission from neutral excitons X^0 is detected if the electron injection is compensated by a reverse bias. Remarkably, a single line is observed for the X^{1-} transition, whereas two lines belong to the X^{2-} state. Similar to neutral exciton complexes, possible final states of multiple exciton complexes can be non-degenerated due to different spin configurations.

Assuming strong quantum mechanical confinement, the Coulomb interactions between charge carriers can be calculated using perturbation theory. Warburton et. al. calculated the energy shifts in the spectra depending on the number of electrons (holes) added to a neutral exciton configuration [80]. Interestingly, an asymmetry for the negatively charged $1X^-$ and the positively charged $1X^+$ exciton occurs since the effective masses and lengths of the two charge species differ. In the case of a negatively charged exciton, the electron of the electron-

hole pair is repelled by the extra electron in the QD, whereas the hole of the electron-hole pair is attracted. Because of the asymmetry in effective lengths, the attraction of the hole dominates over the repulsion of the electron, and the resulting spectral line $1X^-$ is shifted towards lower energies. Vice versa, the transition of a positively charged exciton $1X^+$ is blue-shifted relatively to the neutral exciton recombination.

1.5   Composition and strain

So far, in order to predict PL energies of self-assembled QDs, the dimensionality, the geometrical shape and the occupation with charges have been considered. This already gives a good theoretical model for QDs. However, this model is no longer valid when the QD is too inhomogeneous. QDs usually show inhomogeneities in their composition, i.e. the indium content changes locally throughout the dot. The inhomogeneous composition locally alters the electronic band potentials and also leads to strain effects because of different lattice constants of the materials.

A common technique for fabricating self-assembled QDs is MBE. In the MBE process, the principal constituents InAs and GaAs are deposited on a substrate. Due to segregation effects, the indium content is never uniform throughout the whole dot. The heterostructure usually shows significant composition gradients [33,34,51,72,84] in the QD and a reduced indium concentration in both, the QDs and the WL, which consequently alters the electronic levels. For smaller QDs, the wave functions of bound electrons and holes are elongated over a large part of the dot. Thus, a local inhomogeneity in composition alters the wave functions only weakly. This is not true for larger nanostructures where a locally enhanced or lowered indium content can cause a localization of charge carriers inside such structures. A crucial parameter which determines the composition is the growth rate during the epitaxy process. It was found that for lower growth rates the indium content gets higher whereas higher growth rates yield QDs with broader distribution of composition and geometrical size and an overall lower indium content [32]. This can be explained by diffusion and segregation processes. A higher indium concentration inside the QDs means effectively smaller band gaps causing optical transitions at lower energies. Therefore, the growth rate plays an important role for the control of optical properties of self-assembled QDs.

Due to different lattice constants, epitactically grown materials are subject to strain. The strain causes a deformation potential altering the energy levels of conduction and valence band [5]. The formalism developed by Bardeen et. al. was extended by Zhang [83] taking into account inhomogeneous strain and degenerated band structures. Especially for QDs, the influence of the deformation potential on electrons and holes cannot be neglected since there the variation of strain is comparable to the scale of envelope functions. Grundmann et. al. calculated the detailed strain distributions, energy levels and wave functions for
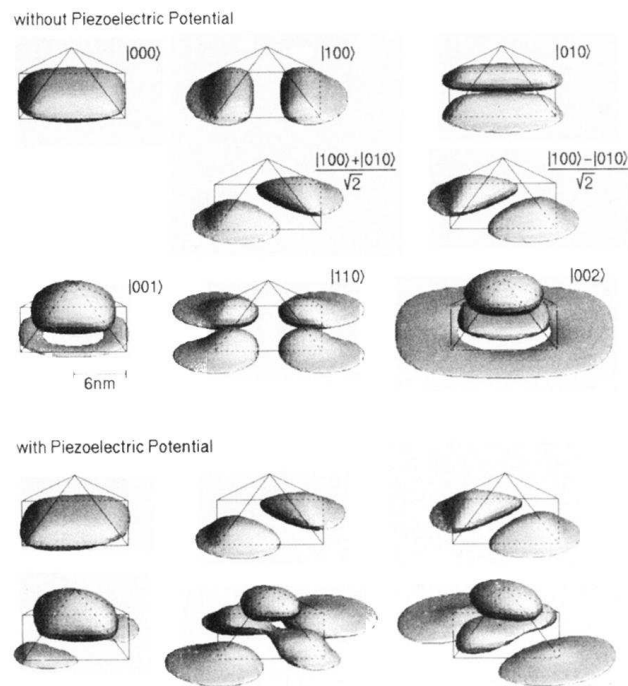
Figure 1.6: Isosurfaces of squared heavy-hole wave functions without (upper part) and with (lower part) inclusion of the piezoelectric potential. The $|100\rangle$ and $|010\rangle$ states are degenerated if piezoelectricity is neglected. For finite piezoelectric potentials, this degeneracy is lifted. From [26].

the case of pyramidal shaped QDs. In figure 1.6, the isosurfaces of the squared heavy-hole wave functions are shown for different eigenstates. The isosurfaces of electronic wave functions are not shown since electrons are more delocalized compared to holes due to their lower effective masses. The strain-induced deformation potential squeezes the hole ground state $|000\rangle$ to the bottom of the QD. The first excited heavy-hole levels $|100\rangle$ and $|010\rangle$ are twofold degenerated if only the deformation potential is taken into account. This degeneracy is lifted if an additional piezoelectric potential is considered. The splitting of the two energy levels is increased for larger nanostructures as the dipole moment scales with the geometrical dimensions of the QD. For small QDs, this splitting can be less than $\Delta E = 1$ meV.

1.6   Quantum posts

So far, the properties of self-assembled QDs have been discussed. QDs are heterostructures which have been studied extensively both theoretically and experimentally. In this thesis, mainly Quantum Posts (QPs) are investigated. These are columnar nanostructures which are laterally embedded in a QW matrix. QPs combine excellent optical properties and an additional degree of freedom in vertical direction. The main difference lies in the controllable height of the QPs in contrast to QDs. Due to these unique properties, QPs are attractive candidates for several applications, e.g. lasers [49, 78] and THz/intrasubband devices. Moreover, enhanced control over the polarization of emitted light can be achieved [36]. The fabrication process of QPs is related to that of self-assembled QDs. In the following, further details for the fabrication of QP structures are provided. Afterwards, the electronic properties of QPs are discussed.

1.6.1   Fabrication and morphology

The influence of composition, strain and piezoelectricity on the electronic levels and successively on the corresponding PL spectra depends strongly on the particular geometrical shape of the nanostructure. QPs are formed by multiple repetitions of a deposition sequence with growth interruptions [30, 31, 78]. A sketch of the growth procedure is provided in figure 1.7. First, InAs is deposited on the GaAs substrate to form seed QDs. These QDs act as nucleation centers for the following deposition sequences. After formation of the first QD layer, GaAs and InAs are deposited alternately. Growth interruptions between each deposition step support further diffusion of the two components Ga and In. Due to lattice mismatch, it is energetically favorable for the gallium atoms to detach from the InAs islands whereas indium atoms prefer these sites. Therefore, columnar shaped and indium rich nanostructures are formed by such a deposition sequence. The indium concentration in these structures depends on the particular growth conditions. The QP samples studied for this thesis have an indium concentration of $c_{\mathrm{In}} = 45$ % inside the QPs and $c_{\mathrm{In}} = 10$ % in the matrix surrounding the posts. These values have been determined by energy
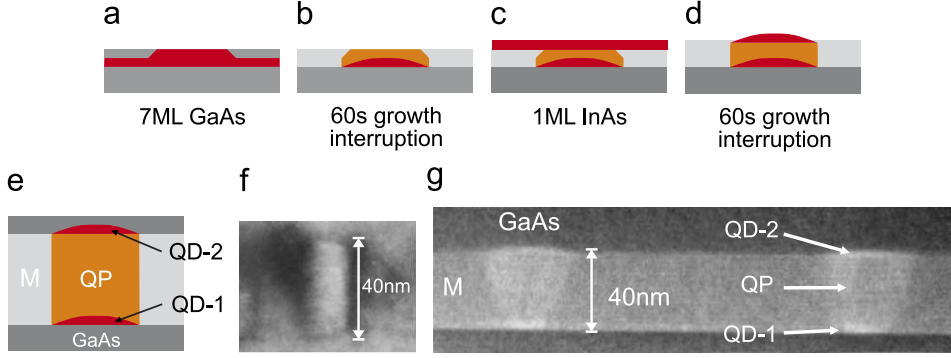
Figure 1.7: (a-d): Schematic of the QP growth process. (e): Schematic of resulting QP. Dark grey: pure GaAs, light grey: matrix-QW ($c_{\text{In}} = 10$ %), orange: QP ($c_{\text{In}} = 43$ %), red: seed and cap QD ($c_{\text{In}} = 48$ % and $c_{\text{In}} = 45$ %, respectively). (f-g) X-TEM images. From [41].

dispersive X-ray (EDX) [30]. It should be noted that the measured indium content inside the posts is not distributed uniformly but is enhanced at the two ends of the QPs [41] leading to the formation of dot like structures inside the QPs. Figure 1.7 shows a sketch of the resulting QP and two cross-sectional transmission electron microscopy (X-TEM) images of a $d_{\text{QP}} = 40$ nm high QP. The height of the QP is controlled by the number of deposition cycles. 16 repetitions have been used in the case of the $d_{\text{QP}} = 40$ nm QP, 8 repetitions in the case of the sample with $d_{\text{QP}} = 23$ nm high QPs. The dislocation free formation of QPs with heights $d_{\text{QP}} > 60$ nm have been demonstrated without modifying the growth protocol.

1.6.2 Single particle levels

The QPs differ from self-assembled QDs in many aspects, e.g. geometrical dimensions, composition, strain and piezoelectricity. Therefore, different electronic levels and wave functions are expected. The upper diagrams of figure 1.8 show single particle energies and probability densities which are computed using an 8-band strain-dependent $k \cdot p$ model for the $d_{\text{QP}} = 23$ nm and $d_{\text{QP}} = 40$ nm high QP [41]. For the computation, the aforementioned QP composition is assumed.

The single particle levels depend strongly on the geometrical dimensions of the nanostructure. For QPs, the height becomes comparable to the lateral dimensions. Therefore, higher lying bound eigenstates are also present for the z-quantization which was not the case for QDs. For the $d_{\text{QP}} = 23$ nm high QP, the first and second excited electron levels lying $\Delta E = 18$ meV above the ground state are almost degenerate reflecting similar confinement lengths for the vertical and radial directions. For the $d_{\text{QP}} = 40$ nm QP, one of these electronic states, corresponding to the vertical quantization, is shifted downward to a level lying $\Delta E = 7$ meV above the ground state. Thus, the shift of the
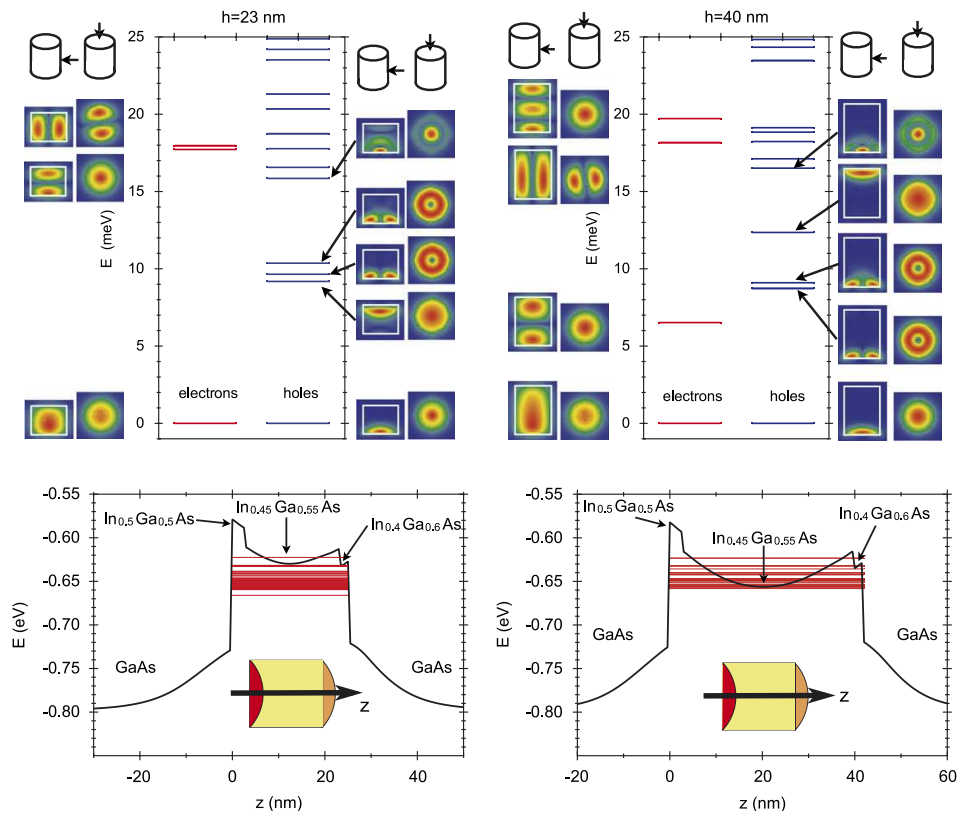
Figure 1.8: Upper panels: Computed single particle states for 23 nm (left) and 40 nm (right) QPs. The probability densities are shown in a plane containing the symmetry axis and a plane perpendicular to the growth direction. Lower panels: Valence band edges and confined hole states plotted against the symmetry axis of the post. From [41].

vertical quantization state can be tailored by controlling the QP height d_{QP}. This opens a wide field of applications for mid-infrared and THz applications and devices. The radial-excitation state remains at the same energetic level since the lateral dimension of the QP is not altered.

The lower diagrams in figure 1.8 show the valence band edges and the hole eigenstates plotted along the symmetry axis of the post. Due to different effective masses, the electrons are spread out wider over the entire QP whereas the heavier holes are localized at the two ends of the QP. Therefore, the local strain influences the valence band structure stronger than the conduction band structure.

1.7 PL spectroscopy on single quantum posts

In the previous section, the fabrication and the resulting single particle states for electrons and holes are introduced. Like in QDs, electrons and holes occupying a QP form exciton complexes. The radiative decay of excitons can be measured by standard PL spectroscopy. In this section, PL spectra of individual QPs are presented. By varying the excitation parameters, particular peaks can be assigned to their corresponding exciton transitions. First, the laser intensity is varied and the integrated peak intensities are compared. Second, the PL of a single QP is compared under different excitation schemes, i.e. pulsed excitation and continuous wave (cw) mode. From these two experiments much information can be drawn about the different excitonic states involved.

Experiments on single QPs are only possible in regions of the sample where the QP surface density is low enough. In order to isolate such region, a special procedure is applied as explained in section 3.5. To ensure that one single QP is detected, the laser intensity is decreased to a low level. Then, a single quantum emitter shows only one or few spectral lines. An additional test is performed by reading out the entire CCD chip of the spectrometer camera which is explained below (see section 3.2). When the PL is detected in first order of diffraction, then, spatial information along one direction of the sample is restored. This can be used to distinguish the signals of different QPs and furthermore to isolate a single QP.

For a first characterization of a single QP, the laser intensity is varied and the corresponding PL spectra are investigated. An example of such laser intensity series is shown in figure 1.9 where a laser with center wavelength $\lambda_{\mathrm{L}} = 661$ nm is used emitting short laser pulses with a duration of $\Delta t_{\mathrm{L}} \approx 50$ ps. The repetition rate of this laser is $f_{\mathrm{L}} = 80$ MHz. For the lowest laser intensity, only one single peak at $E = 1297.5$ meV is observed indicating the emission of a single QP. For increasing laser intensity, a second peak ($E = 1296.7$ meV) close to the first one arises. The doublet marked as $1X^{-}$ is also present at higher intensities. For a laser intensity of $P_{\mathrm{L}} = 7.2$ nW, a small peak at $E = 1306.25$ meV arises. This peak is accompanied by another even smaller
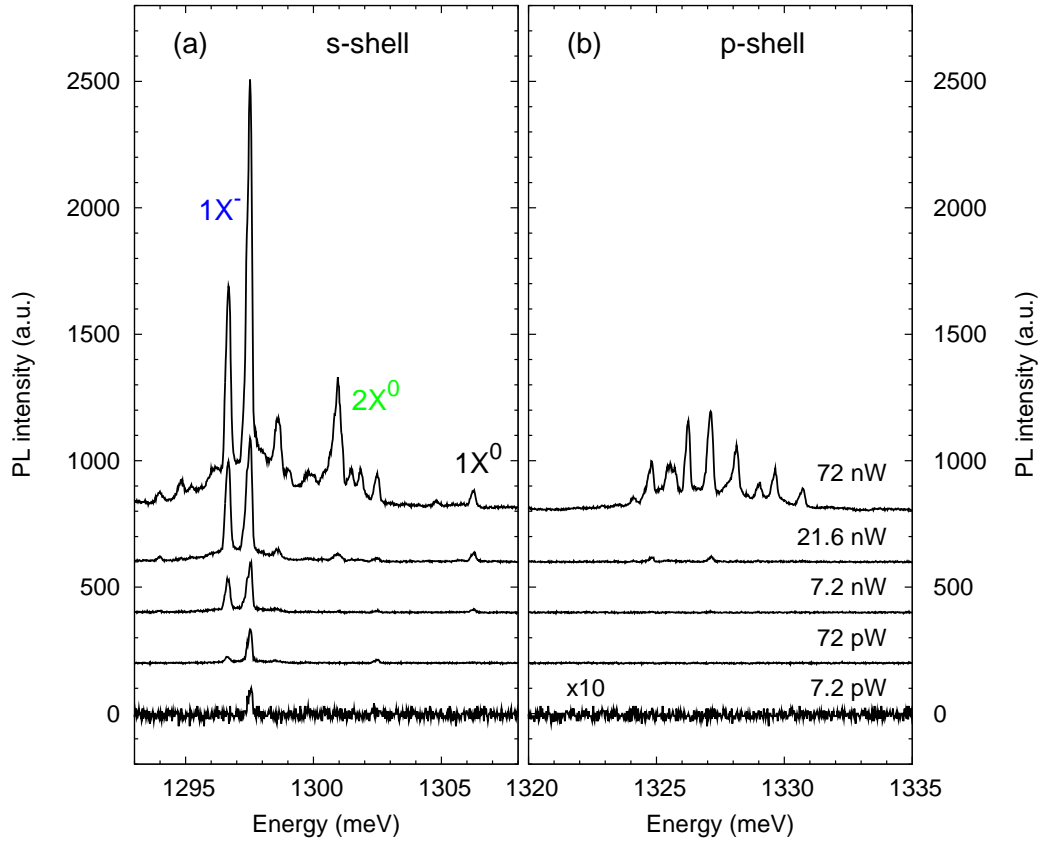
Figure 1.9: Laser intensity series of a single QP. A pulsed laser with center wavelength $\lambda_L = 661$ nm is used. The peaks on the left belong to s-shell transitions, the peaks on the right to p-shell transitions. The PL spectrum measured for the lowest laser intensity is multiplied by a factor of 10 in order to point out the remaining $1X^-$ emission.

peak at $E = 1304.8$ meV. The energetic shift between the two doublets labeled as $1X^-$ and $1X^0$ is $\Delta E = 8.4$ meV. This value is characteristic for spectral shifts reported for the splitting between an $1X^0$ exciton and a singly charged exciton in QDs [23, 81]. This does not yet justify the assignments made in figure 1.9, but below more evidence is supplied. At a laser intensity of $P_\mathrm{L} = 21.6$ nW new lines appear shifted by $\Delta E = 22$ meV from the $1X^0$ doublet towards higher energies apparent in the right panel of figure 1.9. This energy shift is significant for transitions from p-shell states of a QP. For the highest laser intensity of $P_\mathrm{L} = 72$ nW, a multiplet of PL lines is detected. Between the $1X^0$ and the $1X^-$ lines another group of lines around $E = 1301.5$ meV labeled as $2X^0$ appear as the laser intensity is increased. The splitting between these peaks and the $1X^0$ doublet is approximately $\Delta E = 4$ meV.

Despite the structural differences between QPs and QDs, their PL spectra are similar. This can be explained by the dominant interaction of charges occupying the post or dot system. Therefore, the spectra of both systems can be compared at least qualitatively. The low energy lines of the s-shell transitions are all attributed to charged excitons or multiple neutral excitons. For QDs, the biexciton emission and the $1X^-$ lines are mostly shifted towards lower energies with respect to the $1X^0$ exciton [6, 80]. Similar optical properties of QPs and QDs allow for comparing the spectral lines with assignments made in QD systems. The observed splittings and attributions are consistent with previous experimental and theoretical studies of various QD systems [12, 61, 67, 68, 70, 71, 81].

To support the assignments made so far, the integrated PL of the different lines is plotted against the laser intensity. In the right panel of figure 1.10, the integrated PL of three different groups of spectral lines, namely $1X^0$, $2X^0$ and $1X^-$, is displayed. In the double logarithmic plot, the slopes give the power laws of the different curves. For the $2X^0$ exciton, the steepest slope of all three transitions is observed indicating a radiative biexciton decay. In the literature, the PL of the biexciton transition shows a quadratic behaviour as the laser intensity is increased, but this is only true for a continuous excitation source which is not the case here. For a pulsed laser excitation, the slopes differ from continuous excitation but the steepest slope is also attributed to the $2X^0$ luminescence [69]. The slopes in figure 1.10 are calculated within a intensity range of $P_\mathrm{L} = 2 - 75$ nW. For higher intensities, the PL shows a rather saturating characteristic and for even higher intensities (not shown) the entire luminescence spectrum rises exponentially.

Comparing the left panels of figure 1.9 and 1.10, an important difference is obvious. For the lowest excitation intensities, the $1X^0$ emission is present in the case of figure 1.10 whereas in figure 1.9 the neutral exciton transition is absent, instead emission from the $1X^-$ exciton is detected. This observation is attributed to the heterogeneous composition of distinct posts. Therefore, the probability to capture one charge species can be different from post to post giving rise to the observation of predominantly charged or neutral exciton complexes, respectively.
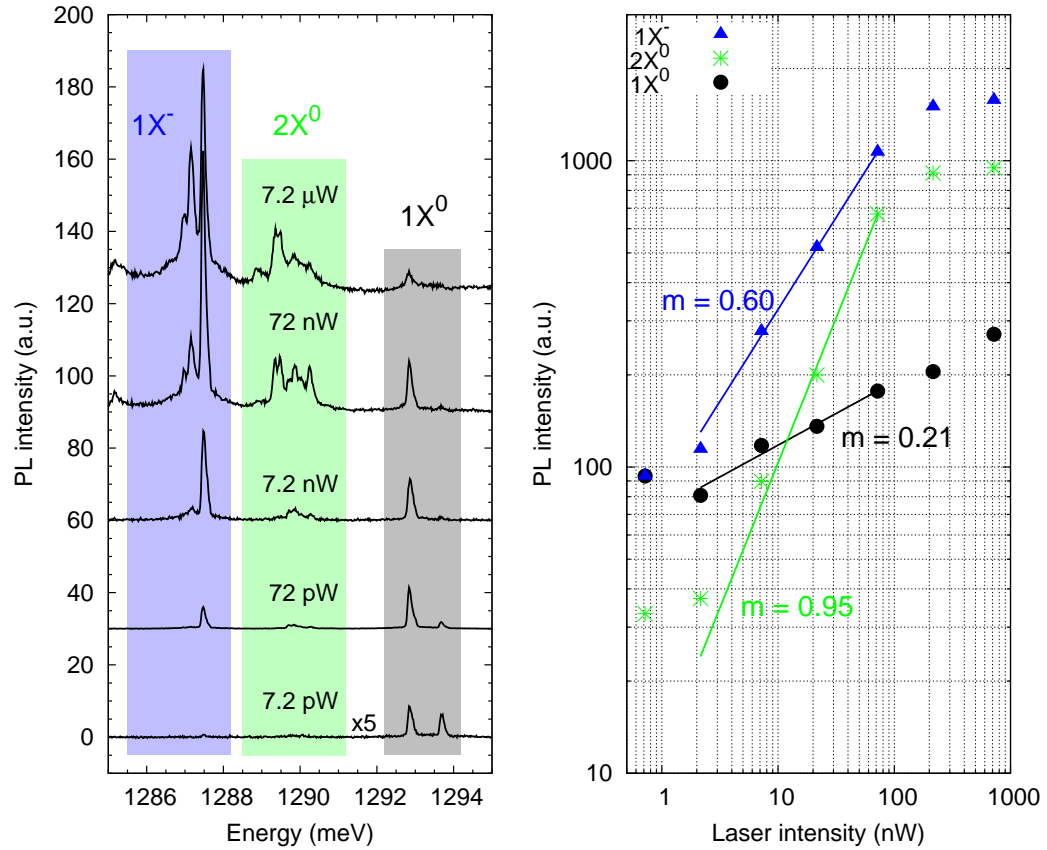
Figure 1.10: Left panel: Laser intensity series of a single QP. A pulsed laser with center wavelength $\lambda_\mathrm{L} = 661$ nm is used. Each spectrum is normalized taking into account the integration time. The spectrum with lowest excitation intensity is multiplied by a factor of 5 for clarity. Right panel: Integrated PL of $1X^-$, $2X^0$ and $1X^0$. The integration is realized by summing up all counts between the wavelength/energy ranges belonging to the particular transitions indicated by the shaded areas.

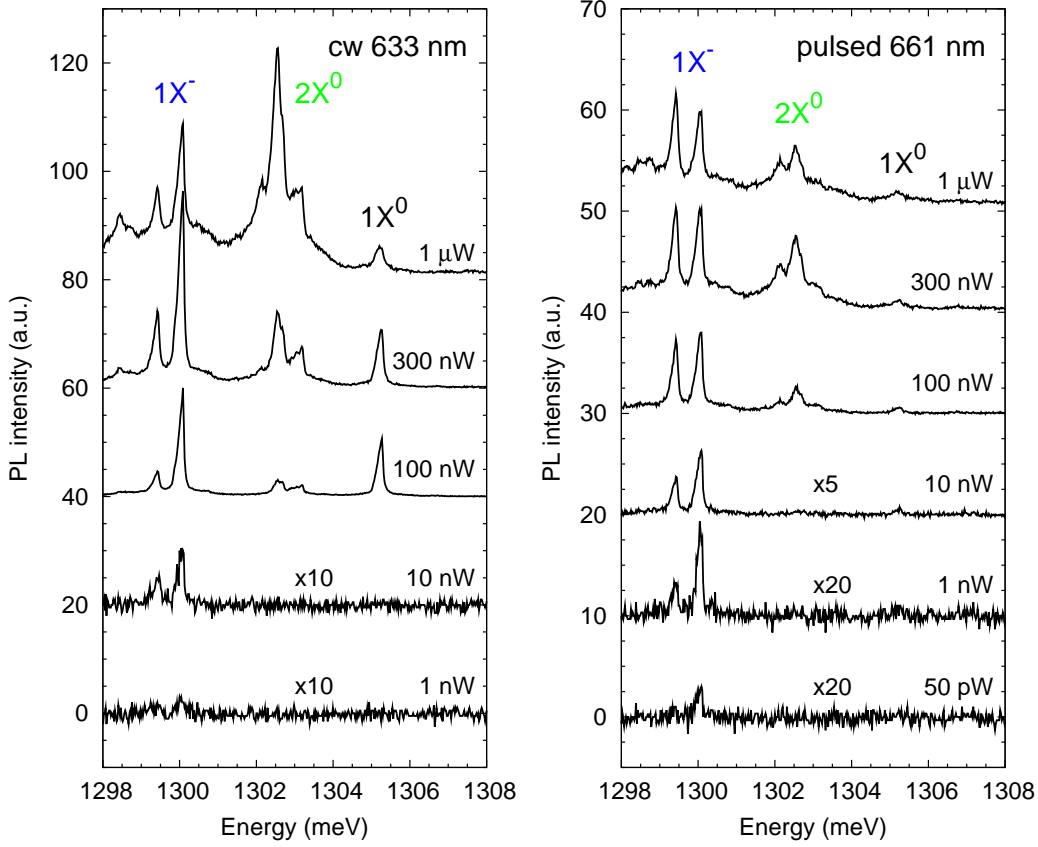Figure 1.11: Comparison of PL emission from the same QP under different excitation schemes. Left panel: HeNe Laser, continuous wave mode. Right panel: Diode Laser, pulsed mode, $\Delta t_L \approx 50$ps, $f_L = 80$ MHz.

Both spectra exhibit doublets for the $1X^0$ and the $1X^-$ signal which can be explained by a strong localization of holes and a non-uniformly distributed indium concentration inside the post structure. After reference [41], the indium content is enhanced at the two ends of the post forming dot like structures. Therefore, the holes prefer to occupy the two ends whereas the electrons are delocalized across the entire post due to their lighter effective masses. Moreover, the two dot like ends have different indium contents ($c_{In} = 48$ % and $c_{In} = 45$ %, respectively) which was measured by EDX [41]. Consequently two lines are observed for each transition resulting from the recombination at the upper and lower end. The splitting energy of the observed doublets is in the order of $\Delta E = 1$ meV.

As mentioned before, the occupation of the different energy levels in the QP depends also on the operation mode of the laser. Here, mostly a pulsed laser with a center wavelength $\lambda_L = 661$ nm and a maximum repetition rate $f_L = 80$ MHz is used. The pulse width of the laser is $\Delta t_L \approx 50$ ps which is shorter than the average exciton recombination times. For a pulsed excitation, recombination

takes place in a cascaded manner. First, higher occupied levels and multiexciton complexes decay radiatively, then, emission from lower levels is detected. Even for higher laser intensities, the QP runs through an entire recombination cascade. Thus, a pulsed excitation scheme generates emission from higher levels if the laser intensity is increased, but at the same time emission from lower levels is still present and comparable with former. This trend can be observed for example in the laser intensity series shown in the right panel of figure 1.11.

If a QP is excited in continuous wave mode, the situation becomes different. Then, the levels are filled constantly and a steady state of occupation is achieved. For higher laser intensities, the recombination of multiexciton complexes is preferred and the emission from lower levels is inhibited. The spectra in the left panel of figure 1.11 are measured under continuous wave excitation. At high laser intensities, the biexciton emission clearly dominates over emission from $1X^-$ and $1X^0$. These observations confirm the assignments made to the particular transitions and demonstrate that in PL experiments the QP system behaves similar to other QD systems.

1.8   External parameters

The PL transition energies are strongly influenced by *internal* parameters of the QDs or QPs, meaning the dimensionality of the nanostructure, the geometrical shape, the composition, strain and piezoelectricity. In this section, the effect of an *external* field is considered. Since nanostructures can be occupied by charges, a magnetic or electric field interacts with these charges via Coulomb forces giving rise to a change of transition energy. In this thesis, the investigated nanostructures are exposed to external electric fields and to mechanical strain. Both parameters influence excitonic PL spectra. Therefore, a short introduction into the interaction between excitons and external electric field is given. Subsequently, strain-induced changes of the emitted PL are discussed.

1.8.1   Electric field

Although excitons are charge neutral, there is an interaction between electric field and exciton because of the dipole character of the electron-hole pair. For a QD or QP, the signature of external electric fields on the PL spectrum can be quite complex since many internal parameters, e.g. occupation with charges, composition, strain, piezoelectricity and geometrical shape of the nanostructure, have to be considered. If the influence of such inhomogeneities is small and only a single exciton $1X^0$ is present in the nanostructure, then the situation can be simplified. In a first approximation, the 0-dimensional structure is considered as a quantum box. A quantum box behaves like a quantum well in each direction. Therefore, the formalism of the well known *Quantum Confined Stark Effect* (QCSE) can be applied [53]. The QCSE is depicted schematically in figure 1.12. The applied electric field tilts the band edges and pulls apart the centers of the wave functions of electron and hole. Overall a reduction of the transition energy
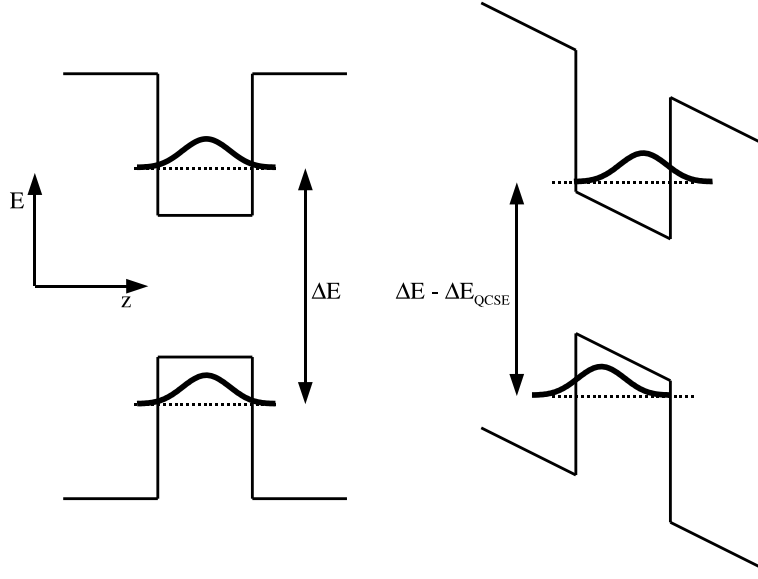
Figure 1.12: Illustration of Quantum Confined Stark Effect. Left: without electric field, flat conduction and valence bands. Right: external electric field applied, band edges are tilted and transition energy is lowered by ΔE_{QCSE}. Thick curves represent probability densities.

is detected. The dipole moment $\mathbf{p}$ of the exciton couples to the electric field $\mathbf{F}$ and the shift towards lower energies is defined through:

$$\Delta E_{\mathrm{QCSE}} = -\mathbf{p} \cdot \mathbf{F} \tag{1.12}$$

The dipole moment $\mathbf{p}$ consists of a built-in dipole moment $\mathbf{p}_0 = e\mathbf{s}_0$, where $\mathbf{s}_0$ is the displacement of electron and hole at zero-field, and an induced dipole moment $\mathbf{p}_{\mathrm{ind}} = e\mathbf{s}_{\mathrm{ind}}$ which arises from an additional displacement caused by the field. The induced dipole moment depends in a first approximation linearly on the electric field:

$$\mathbf{p} = \mathbf{p}_0 + \beta\mathbf{F} \tag{1.13}$$

Here, β is the polarizability of the exciton. The resulting red shift caused by the QCSE depends quadratically on the electric field:

$$\Delta E_{\mathrm{QCSE}} = -\mathbf{p}_0 \cdot \mathbf{F} - \beta F^2 \tag{1.14}$$

The induced dipole moment $\mathbf{p}_{\mathrm{ind}}$ increases linearly with electric field, but for smaller nanostructures, the additional displacement $\mathbf{s}_{\mathrm{ind}}$ is limited by the size of the structure. Therefore, at high electric fields, $\mathbf{s}_{\mathrm{ind}}$ remains constant and as a consequence, the QCSE energy shift is no longer quadratic but depends linearly on the electric field.
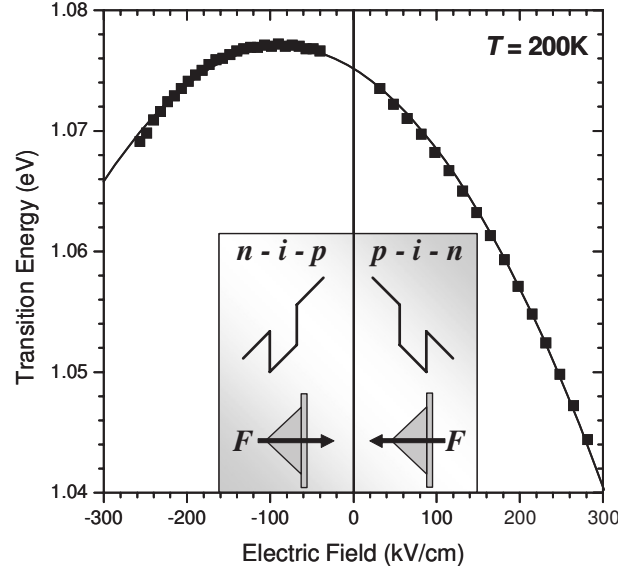
Figure 1.13: Transition energy of self-assembled InAs QDs as a function of an external electric field F. The inset indicates the orientation of the applied electric field with respect to the QD for the two different device structures. From [56].

In figure 1.13, the energy of the s-shell transition of InAs self-assembled QDs is plotted as a function of an applied electric field F. Remarkably, the maximum of the transition energy is not observed at $F = 0$, but is shifted towards negative electric fields, indicating a nonzero value of the built-in dipole moment $\mathbf{p}_0$. This observation can be explained by the inhomogeneous composition of the studied QDs. Since electrons have smaller effective masses m^* than holes, their wave functions are delocalized over the entire QD. Vice versa, holes are more sensitive to morphology and local composition. Thus, holes are localized in areas of deeper effective confinement. This asymmetric behaviour gives rise to a spatial separation of the wave function centers resulting in a small permanent dipole moment. The parabolic characteristic of the transition energy observed in figure 1.13 is in accordance with equation 1.14.

1.8.2   Strain

As already discussed in section 1.5, QD structures are subject to mechanical strain due to different lattice constants of the grown materials. The mechanical strain induces a deformation potential altering the eigenstates of electrons and holes. Since this strain contribution is caused by the structure itself, the shift of eigenstates and wave functions with respect to this type of strain is constant. Nakaoka et. al. fabricated a micro-electromechanical system, in which QDs are embedded and external strain can applied to this system [57, 58]. The device consists of an air-bridge which is produced using electron beam lithography and reactive ion etching techniques. A scanning electron microscopy (SEM) image of such air-bridge is provided in figure 1.14.
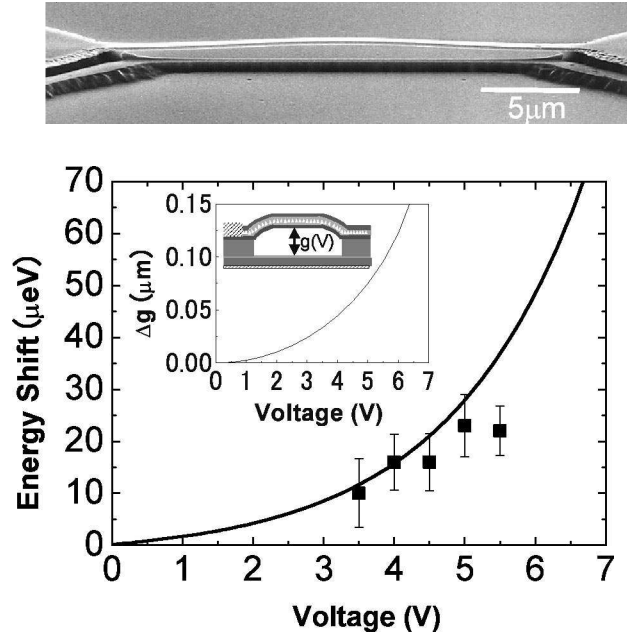
Figure 1.14: Upper picture: SEM image of the air-bridge. The deformation is caused by applying a voltage between bridge and substrate. Lower diagram: Calculated (solid line) and measured (solid squares) energy shift of an individual self-assembled InGaAs QD as a function of the bias voltage. The inset shows the calculated air-gap at the center of the air-bridge. Reproduced after [57].

A layer of self-assembled InGaAs QDs close to the top surface of this bridge emits luminescence which is detected by a μ-PL setup (compare also section 3.1). By applying a voltage between the substrate and a p-doped layer below the QD layer, the bridge is pulled down towards the substrate. The mechanical deformation of the bridge induces additional strain which alters the wave functions and the eigenstates of electrons and holes occupying the QDs. The lower diagram in figure 1.14 shows the shift of transition energy as a function of the applied voltage causing the deformation of the bridge. The experimental data is supported by a mathematical model (solid curve). The model takes into account the deformation as a function of applied voltage and the energy level shifts following the bridge deformation which are obtained by solving the 3-dimensional Schrödinger equation [57].

Chapter 2

Surface Acoustic Waves

2.1 Basic properties

Surface acoustic waves (SAWs) are used in this thesis in order to manipulate the luminescence of GaAs based semiconductor heterostructures. SAWs are mechanical waves. However, on piezoelectric substrates like GaAs, Lithiumniobat (LiNbO$_3$) or quartz (SiO$_2$) the mechanical wave is accompanied by a "electric wave", i.e. a dynamically modulated piezoelectric field. In contrast to LiNbO$_3$ or SiO$_2$, however, GaAs has semiconducting properties. Moreover, by epitaxial growth, GaAs can be combined with other III-V semiconductors. Therefore, GaAs based heterostructures have unique properties and are very interesting candidates for SAW experiments.

Here, the piezoelectric field of a SAW is used to manipulate laser excited charge carriers. For applying an electric field to semiconductor structures, usually a different approach is used and the nanostructures are embedded in a diode junction. However, the switching speed of such type of device is limited due to its finite capacitance. Moreover, the diode has to be contacted electrically requiring contact pads. These contacts are disadvantageous since light exciting the sample and the luminescence emitted by the sample are partly blocked. These drawbacks are circumvented by using SAWs which allow for high frequencies (up to several GHz) and free surfaces. In the following, an introduction into the properties of SAWs is given.

2.1.1 Bulk acoustic modes

The theory of elastic waves in solids can be very complex. Fortunately, some principles can be deduced from bulk acoustic modes which are described here. A homogeneous and isotropic material with density ρ is subdivided in infinitesimal small volume elements. To begin with, no external forces or piezoelectricity are considered. When the volume elements are displaced mechanically, they exert force on adjacent volume elements which are also displaced from their rest positions. The displacement $\mathbf{u}(\mathbf{x})$ of such volume element is depicted schematically in figure 2.1. The working forces are described mathematically by a symmetric stress tensor T_{ij} which is linked to the displacements by the equation of motion:

$$\rho\frac{\partial^2 u_i}{\partial t^2} = \frac{\partial T_{ij}}{\partial x_j} \tag{2.1}$$

where ρ is the density of the material. The displacements of the infinitesimal volume elements determine the deformation of the material. Small mechanical displacements can be described by the deformation tensor S_{kl} :

$$S_{kl} = \frac{1}{2}\left(\frac{\partial u_k}{\partial x_l} + \frac{\partial u_l}{\partial x_k}\right) \tag{2.2}$$

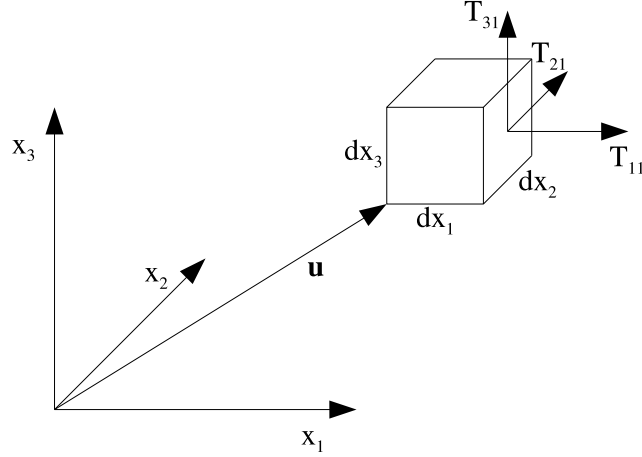Deformation and stress tensor are linked via *Hooke's law*:

Figure 2.1: Infinitesimal volume element displaced by $\mathbf{u}(\mathbf{x})$ from its rest position. Compressive and tensile forces (T_{11}) and shear forces (T_{21} and T_{31}) are also depicted.

$$T_{ij} = c_{ijkl}S_{kl} \tag{2.3}$$

where c_{ijkl} are elastic constants of the elasticity modulus. By substituting equations 2.2 and 2.3 into equation 2.1, a system of coupled differential equations is obtained:

$$\rho\frac{\partial^2 u_i}{\partial t^2} - c_{ijkl}\frac{\partial^2 u_k}{\partial x_j \partial x_l} = 0 \tag{2.4}$$

Equations 2.4 are wave equations. Solutions are plane waves with transversal and longitudinal propagation modes.

For piezoelectric materials, electric restoring forces have to be considered additionally. The piezoelectric properties are caused by the crystal structure showing no inversion symmetry. In order to account for piezoelectricity, Hooke's law has to be expanded by another term introducing the electric field $\mathbf{E}$ and the dielectric displacement $\mathbf{D}$. Then, the so-called constitutive equations are obtained:

$$\begin{aligned} T_{ij} &= c_{ijkl}S_{kl} - p_{kij}E_k \\ D_i &= p_{ijk}S_{jk} + \epsilon_{ij}E_j \end{aligned} \tag{2.5}$$

p_{ijk} and ϵ_{ij} are elements of the piezoelectric and dielectric tensor, respectively. Basically, also electrodynamic effects have to be considered. However, the huge difference in propagation velocities of mechanical and electromagnetic waves allows for a quasi static approximation of the electric field. Finally, wave equations are obtained for bulk acoustic modes in piezoelectric materials taking into

account the equation of motion 2.1, the deformation tensor 2.2, the constitutive equations 2.5, the quasi-static approximation and the Maxwell equations (Coulomb):

$$\rho\frac{\partial^2 u_j}{\partial t^2} - c_{ijkl}\frac{\partial^2 u_k}{\partial x_i \partial x_l} - p_{kij}\frac{\partial^2 \phi}{\partial x_i \partial x_k} = 0 \tag{2.6}$$

$$p_{ikl}\frac{\partial^2 u_k}{\partial x_i \partial x_l} - \epsilon_{ik}\frac{\partial^2 \phi}{\partial x_i \partial x_k} = 0$$

Equation 2.6 can be simplified considerably if the special case of longitudinal waves is assumed. Technically, equation 2.6 can be reduced to a one-dimensional form:

$$\rho\frac{\partial^2 u}{\partial t^2} - c^*\frac{\partial^2 u}{\partial x^2} = 0 \tag{2.7}$$

where c^* is the effective elastic constant:

$$\begin{aligned} c^* &= c\left(1 + \frac{p^2}{\epsilon c}\right) \\ &= c\left(1 + K^2\right) \end{aligned} \tag{2.8}$$

K is the electromagnetic coupling constant. Since $K^2 > 0$, it is also required that the effective elastic constant is larger than the corresponding value without piezoelectricity:

$$c^* > c \tag{2.9}$$

Generally speaking, piezoelectric materials appear to be stiffer than non-piezoelectric materials. Moreover, the propagation velocity v^* of the mechanical wave is increased as compared to non-piezoelectric materials.

$$\begin{aligned} v^* &= \sqrt{\frac{c^*}{\rho}} \\ &= \sqrt{\frac{c(1 + K^2)}{\rho}} \\ &\approx v\left(1 + \frac{1}{2}K^2\right) \end{aligned} \tag{2.10}$$

2.1.2 Surface Acoustic Waves

The formalism developed so far can be applied to SAWs taking into account mechanical and electric boundary conditions. The medium, where the SAW
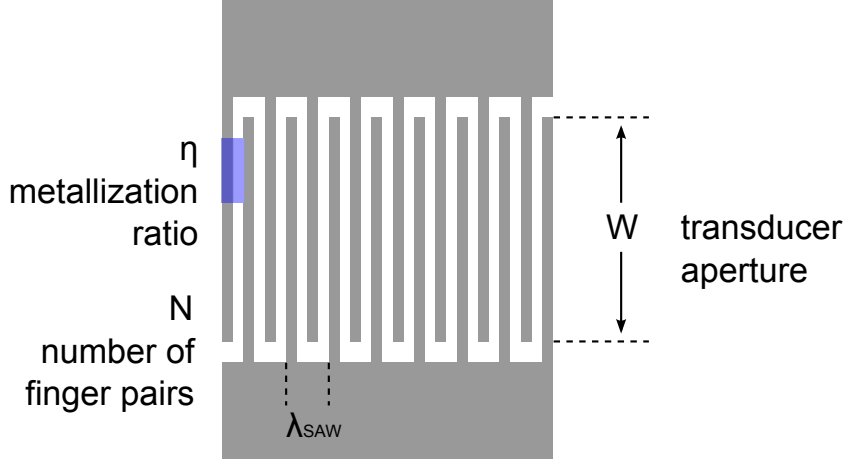
Figure 2.2: Schematic view of an Interdigital Transducer (IDT). The wavelength of the generated SAW λ_{SAW} is determined by the finger period. The metallization ratio η is the ratio of the finger width to $\lambda_{\text{SAW}}/2$. The overlapping of the fingers is called transducer aperture W. The horizontal areas are used as contact pads.

propagates, is extended infinitely along the x_1 and x_2 axes and for $x_3 < 0$. Therefore, the force components perpendicular to the surface vanish:

$$T_{31} = T_{32} = T_{33} = 0 \quad |_{x_3=0} \tag{2.11}$$

There are two ideal cases for electric boundary conditions:

- electrically free surface

- massless metallized surface

Taking into account one of these mechanical and electric boundary conditions, equation 2.6 cannot be solved analytically. Numerical calculations show that there are several propagation modes possible. The so-called *Rayleigh wave* is a prominent mode and a pure surface wave. A predominant part of its energy is concentrated to a thin layer ranging from the surface to a depth of the order of one wavelength λ_{SAW}. The mechanical and electrical amplitudes of the wave decrease exponentially with depth.

Apart from theoretical aspects, the generation of SAWs is of fundamental interest. A common technique for the generation are so-called Interdigital Transducers (IDTs) which are structures that can be fabricated by lithographic methods. An IDT consists of a thin metal film deposited on top of the piezoelectric material. The geometric shape looks like two combs with interpenetrating fingers as depicted in figure 2.2.

An IDT uses the inverse piezoelectric effect for the generation of SAWs. By applying an AC voltage to both contact pads, a deformation of the material beneath is caused. If the frequency of the applied voltage matches the resonance

frequency of the IDT structure, then, the deformations interfere constructively and a SAW is launched from the IDT. The IDT resonance f_{SAW} is linked to the wavelength of the SAW λ_{SAW} via the propagation velocity v_{SAW}:

$$f_{\mathrm{SAW}} = \frac{v_{\mathrm{SAW}}}{\lambda_{\mathrm{SAW}}} \tag{2.12}$$

For the effective generation of SAWs it is very important to align the IDT relative to the crystallographic orientation. IDTs can be used as emitters and receivers of SAWs. A common configuration is the arrangement of two opposing IDTs, a so-called *delay line*. Then, one IDT acts as emitter of SAWs, whereas, the other receives the acoustic wave and converts it to an electric signal. Therefore, IDTs are commonly used as frequency filters, for example in cell phones.

The IDT type shown in figure 2.2 is called a normal finger transducer. Important geometrical parameters are the number of finger pairs N, the period of the transducer λ_{SAW}, the metallization ratio η and the transducer aperture which determines the width of the sound path. Apart from this simple IDT layout, there exist more complex layouts, e.g. with varying finger periods (in-line/dispersive/tapered) or with fingers of same polarity side by side (split). These layouts allow for using several resonance frequencies or frequency bands. Within this work, exclusively normal finger transducers are used. For further reading see for example references [18, 55, 59].

2.2 IDT design

A key requirement to IDTs is the efficient conversion of electric power to acoustic power. This issue is not trivial and a lot of efforts have been done to improve the IDT efficiency (see for instance references [18, 55, 59]). A particular problem is the matching of impedances in the circuit. An IDT performs ideally, if the impedance of the voltage source R_{g} is the same as the impedance of the IDT itself. Here, HF sources are used with a constant impedance of $R_{\mathrm{g}} = 50$ Ω. For best matching, the load has to be as close as possible to R_{g}. Compared to other piezoelectric materials such as $LiNbO_3$, GaAs has a small electromagnetic coupling constant ($K^2_{\mathrm{GaAs}} = 6.4 \cdot 10^{-4}$, $K^2_{\mathrm{LiNbO_3}} = 0.054$). Therefore, the capacitance of the IDT dominates the high frequency properties on GaAs. That is the imaginary part of the IDT admittance. In order to compensate the capacitance of the IDT, an external inductor can be connected in parallel to the IDT. The additional inductance may even be integrated into the sample design via lithographic structures, e.g. planar spiral inductances [62]. This approach improves the efficiency of the IDT, however, additional space on the sample is required.

Due to the layout of the sample carrier, the samples studied in this thesis have to be relatively small ($A \approx$ 5x5 mm^2). Furthermore, more effort has been dedicated to process various IDTs with different frequencies, instead of processing additional circuits on the sample. The design of the IDT itself also influences the
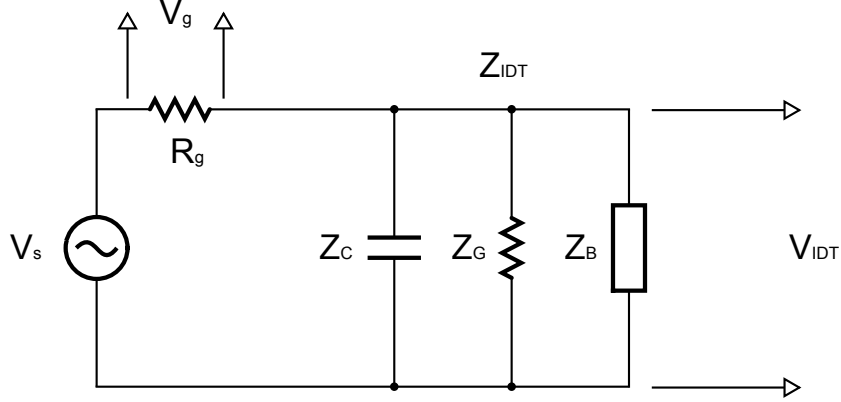
Figure 2.3: Equivalent circuit of IDT with voltage source. The complex IDT resistance comprises an imaginary capacitive part, a real radiation conductance and an imaginary susceptance. The impedance of the source is R_g.

insertion efficiency. In particular, the number of finger pairs N and the metallization ratio η strongly determine the high frequency properties. By adjusting these parameters an improvement of the insertion of acoustic power is achieved.

The electric properties of an IDT connected to a voltage source are represented by an equivalent circuit shown in figure 2.3. A source generates a voltage V_s. Because of a voltage drop in the impedance of the source R_g, the actual voltage across the IDT V_IDT is less than V_s. Mesh rule and knot rule yield:

$$V_\mathrm{s} = V_\mathrm{g} + V_\mathrm{IDT} \tag{2.13}$$

$$\frac{V_\mathrm{g}}{R_\mathrm{g}} = V_\mathrm{IDT}\left(\frac{1}{Z_C} + \frac{1}{Z_G} + \frac{1}{Z_B}\right) \tag{2.14}$$

The reciprocals of the complex resistances Z are the corresponding admittances:

$$Y_C = \frac{1}{Z_C} = \mathrm{i}2\pi f C_\mathrm{IDT} \tag{2.15}$$

$$Y_G = \frac{1}{Z_G} = G(f) \tag{2.16}$$

$$Y_B = \frac{1}{Z_B} = \mathrm{i}B(f) \tag{2.17}$$

$$Y_\mathrm{IDT} = \frac{1}{Z_\mathrm{IDT}} = Y_C + Y_G + Y_B \tag{2.18}$$

where C_IDT is the capacitance of the transducer, $G(f)$ the radiation conductance and $B(f)$ the susceptance of the circuit. Combining equation 2.13 and equation 2.14, the ratio between the voltage appearing across the IDT V_IDT and the voltage of the source V_s can be derived to:

$$\frac{V_\mathrm{IDT}}{V_\mathrm{s}} = \frac{1}{1 + Y_\mathrm{IDT}(f)R_\mathrm{g}} \tag{2.19}$$

In the equivalent circuit model, the acoustic power is the part which is transfered to Z_G. Therefore, the acoustic power is obtained as follows:

$$P_{\text{SAW}} = \frac{1}{2} V_{\text{IDT}}^2 G \tag{2.20}$$

The factor $\frac{1}{2}$ is due to the fact that the IDT emits SAWs in two directions, unless it is an unidirectional transducer. The maximal available power P_{av} is calculated under matched conditions, i.e. instead of the IDT a load with an impedance of exactly R_{g} is assumed:

$$P_{\text{av}} = \frac{V_{\text{s}}^2}{4R_{\text{g}}} \tag{2.21}$$

For the IDT design, the insertion loss IL is an important quantity. The insertion loss is the ratio between the available power P_{av} and the acoustic power P_{SAW} and is quantified on a logarithmic scale (in dB):

$$\begin{aligned} IL &= -10\log_{10}\frac{P_{\text{SAW}}}{P_{\text{av}}} \\ &= -10\log_{10}\frac{2GR_{\text{g}}}{(1+GR_{\text{g}})^2 + [R_{\text{g}}(2\pi f C_{\text{IDT}}) + B]^2} \end{aligned} \tag{2.22}$$

Under matched conditions, the insertion loss would be $IL = 0$ dB. Since $P_{\text{SAW}} < P_{\text{av}}$, positive values for IL are expected. A further important parameter of IDT performance is the acoustic quality Q represented by the ratio between the capacitive admittance and the radiation conductance:

$$Q = \frac{2\pi f_{\text{c}} C_{\text{IDT}}}{G(f_{\text{c}})} \tag{2.23}$$

The acoustic quality Q is defined for the center frequency f_{c}, i.e. the resonance frequency. When the capacitive part dominates, then the system is called *weak coupled*. When the radiation conductance dominates, the system is called *strong coupled*.

Basically, there are two free parameters which can be varied in order to optimize the IDT properties. One is the number of finger pairs N and the other is the metallization ratio η which determines the widths of the fingers and the spacings in between. The parameters transducer aperture W which defines the width of the sound path and center frequency f_{c} are determined beforehand. The frequency f_{c} is chosen to meet experimental considerations and the aperture W is limited by the marker spacing. Markers provide a orientation on the sample and are metallized structures on the surface. In order to prevent short circuits, IDTs are positioned such that the fingers lie in between two marker rows.
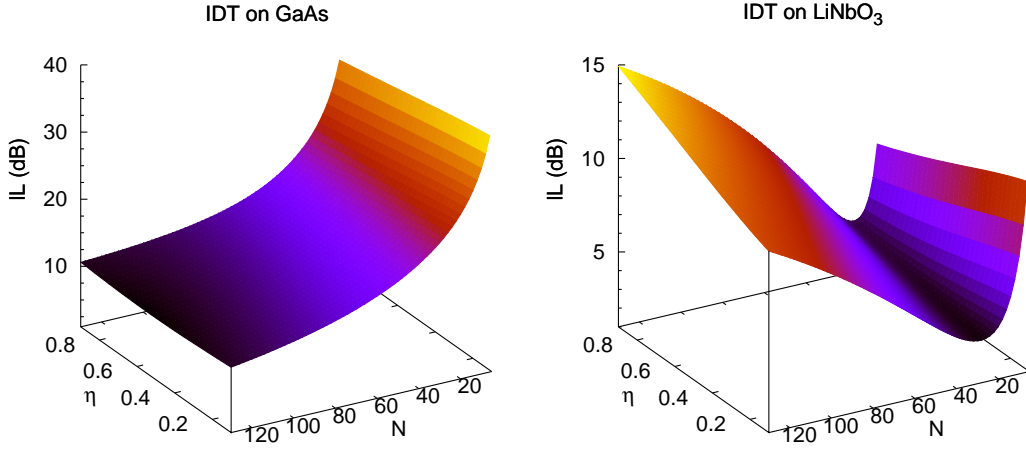
Figure 2.4: Simulation of IDT properties. On the diagrams the insertion loss IL is displayed in false color representation depending on the parameters metallization ratio η and number of finger pairs N for the two materials GaAs and LiNbO$_3$. For both systems, a fixed transducer aperture of $W = 350$ µm and a center frequency of $f_c = 500$ MHz are assumed.

By inserting all known parameters in equation 2.22 and varying the two free parameters N and η, a 2-dimensional data array is obtained which can be plotted in false color representation. Figure 2.4 shows two data sets for IDTs on the materials GaAs and LiNbO$_3$, respectively. The transducer aperture $W = 350$ µm and the center frequency $f_c = 500$ MHz are the same for both systems. According to the definition of the insertion loss IL in equation 2.22, the efficiency of the IDT increases for smaller values of IL. Although the IDTs on both materials are comparable, the insertion losses differ remarkably. Overall, the IDT on LiNbO$_3$ is more efficient showing a lower IL level than the IDT on GaAs. Furthermore, there is a minimum in IL at $N \approx 30$ finger pairs giving the best IDT performance. For the IDT on GaAs, no minimum is observed. There, the matching of impedance becomes better, the more finger pairs N are processed. The metallization ratio η influences IL only marginally for IDTs on GaAs and moderately for IDTs on LiNbO$_3$. Apart from the impedance matching, also lithographic limitations must be considered. Too low or too high metallization ratios η can cause difficulties during the lift-off process and a high number of finger pairs N can result in misalignments which subsequently lower the IDT efficiency.

For the experimental characterization of fabricated IDTs, a network analyzer (*ZVC, Rohde&Schwarz*) is used. A network analyzer sends a HF signal to the device under test and receives a response signal from the device. Depending on the particular configuration, the response is a reflection or transmission signal. The network analyzer relates the output signal to the input signal and displays the ratio as a function of the frequency. For a delay line consisting of two aligned
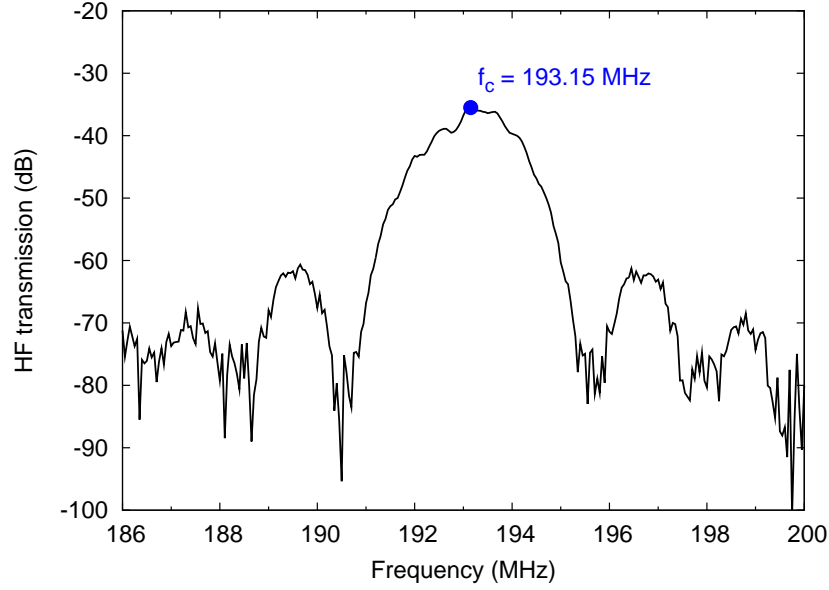
Figure 2.5: HF transmission of transducer delay line measured at $T = 6$ K. The measured response follows a $\mathrm{sinc}(f) = \sin(f)/f$ characteristic.

IDTs, the HF transmission can be measured by applying the input signal to one IDT and measuring the electrical response of the other IDT. Figure 2.5 shows a typical HF transmission response of a transducer delay line with resonance frequency f_{c}.

In summary, adjusting the parameters N and η optimizes the impedance matching and therefore increases the IDT efficiency. Since the optimization process is realized through a theoretical model taking into account the insertion loss IL and the design parameters, no further circuits or devices are required for this kind of optimization. In addition to impedance matching, issues regarding the lithographic processes and frequency response have to be considered carefully. The frequency response is measured by a network analyzer obtaining the center frequency of the transducer f_{c}, the bandwidth and the insertion loss.

2.3   Acoustic charge conveyance and carrier injection

In this section, the influence of SAWs on charge carriers in semiconductor heterostructures is explained. SAWs on piezoelectric materials cause mechanical deformation and dynamically modulated piezoelectric fields. Both, mechanical and electric modulation influence charge carriers directly. The two effects are called *deformation potential coupling* and *acousto-electric coupling*, respectively. Here, the deformation potential coupling turns out to be too weak in order to have significant influence on excited charges. The changes in PL emission caused by SAWs are mainly due to acousto-electric coupling. In the following, both effects are explained and evidence is given for the distinct contributions to charge carrier manipulation.
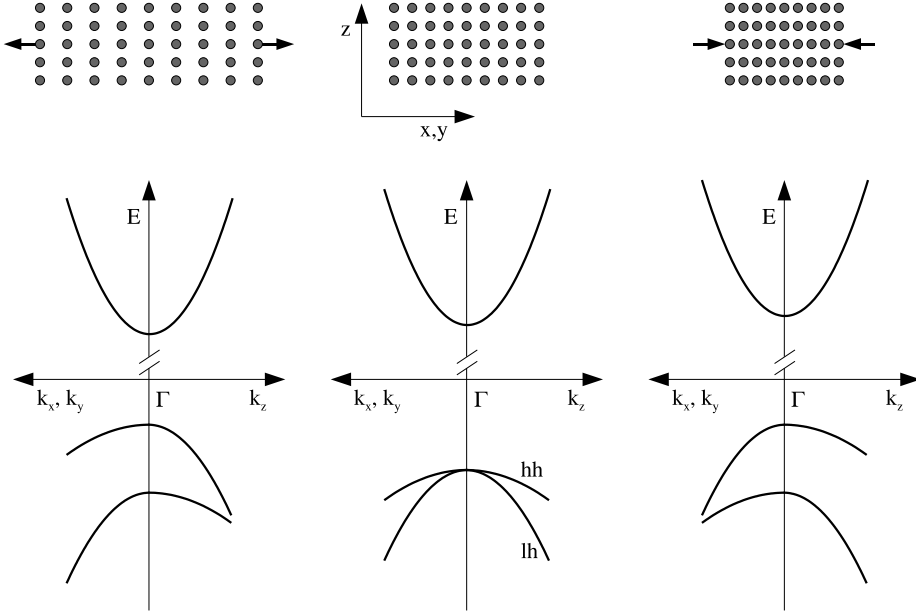
Figure 2.6: Conduction and valence bands of a semiconductor exposed to lateral mechanical stress. Left: tensile stress, non-symmetric splitting of heavy hole and light hole bands. Center: relaxed crystal lattice, symmetric valence bands. Right: compressive stress, non-symmetric splitting of valence bands. After [19, 60].

2.3.1 Deformation potential coupling

Mechanical compression and tension deform the crystal unit cells depending on its relative position to the SAW phase and change their volumes. The relative change of volume of an unit cell is given by the trace of the deformation tensor:

$$\frac{\Delta\Omega}{\Omega} = \sum_{i=1}^{3} S_{ii} \tag{2.24}$$

The relative change of volume causes a modulation of the band gap which is the *hydrostatic* part of deformation. In contrast, the deformation of the unit cell without changing the absolute volume lifts the symmetry of the system and the heavy hole and light hole bands are no longer degenerated. In figure 2.6, the splitting of the two bands is depicted which is caused by non-hydrostatic deformation. The upper part of figure 2.6 shows the crystal lattice when it is stretched, relaxed and compressed resulting in a non-symmetric splitting for the stretched and compressed lattice. For the relaxed lattice no splitting is observed at $\mathbf{k} = 0$. Overall, the hydrostatic and the non-hydrostatic part have to be considered and sum up as follows [9]:

$$\Delta E_{l,h}(S_{ij}) = a\frac{\Delta\Omega}{\Omega} \pm \epsilon_{\mathrm{s}} \tag{2.25}$$

The constant a is called *deformation potential* and is characteristic for the material. The non-hydrostatic part ϵ_{s} depends on non-diagonal components of
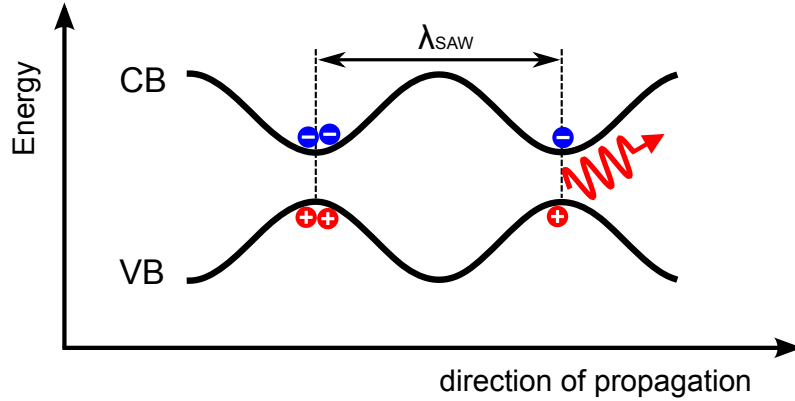
Figure 2.7: Type I band modulation caused by the deformation potential of a SAW. Conduction and valence bands are modulated dynamically, i.e. the modulation pattern moves into the direction of SAW propagation.

the deformation tensor. In accordance to the convention for band alignment in semiconductor heterostructures, the overall deformation potential modulation which is caused by a SAW is called *type I modulation*. Characteristic for the strain-induced type I modulation is that CB minima and VB maxima coincidence and both carrier species are confined to the same locations. In the case of SAWs, the band gap modulation is dynamic, i.e. it depends on space and time coordinates and is directly coupled to the SAW propagation.

A schematic of the SAW induced type I modulation is given in figure 2.7 where the electronic potentials inside a QW are considered. The QW confines charge carriers vertically. Therefore, charges excited in the QW can move only in the in-plane directions. Each energy value in diagram 2.7 corresponds to the Γ-point in k-space, meaning $\mathbf{k} = 0$. Energies are plotted against the direction of propagation.

As shown in figure 2.7, the type I modulation is such that conduction and valence bands are opposite in phase. When a laser excites electrons into the conduction band and holes into the valence band, then, the electrons preferably relax to the minima of the conduction band, whereas the holes preferably relax to the maxima of the valence band. The minima of the conduction band and the maxima of the valence band coincidence. Therefore, an enhanced recombination probability of electrons and holes is expected indicated by the red arrow in figure 2.7. Rudolph et. al. demonstrated that this recombination probability can be reduced, when a double QW structure is used instead of a single QW. Long-living indirect excitons can be transported in these structures over macroscopic distances using the deformation potential [65].

Figure 2.8 shows a sectrum of a single InAs QD which was measured without a SAW (blue line), and a spectrum with a SAW applied (red line) [24]. Clearly, the SAW changes the intensities and relative shapes of the different emission lines. Apart from a general broadening, each line shows two peaks. The two
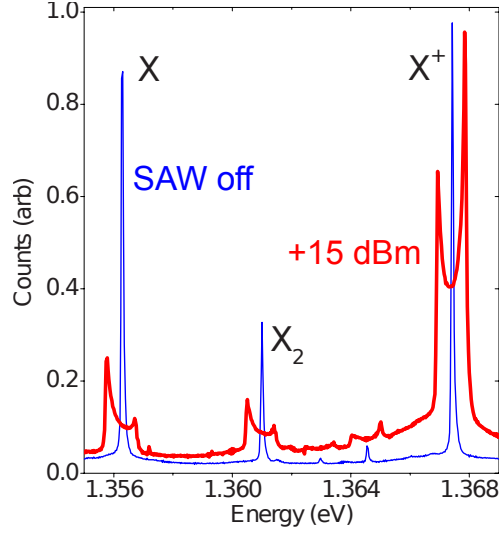
Figure 2.8: PL spectra of an individual InAs QD without SAW (thin blue line) and in the presence of a SAW (thick red line). Reproduced after [24].

peaks of the X^+ transition have been studied separately in a time-resolved experiment and showed a oscillatory behaviour with phase shift $\Delta\phi = \pi$ and frequency f_{SAW}. Gell et. al. attributed this oscillatory modulation of PL energy to a strain-induced effect. In contrast to the experiments presented in this thesis, higher SAW frequencies $f_{\text{SAW}} > 1$ GHz have been used.

2.3.2 Acousto-electric coupling

Apart from the mechanical deformation, SAWs are also accompanied by piezoelectric fields. These fields are described by the constitutive equations 2.5 which link electric field and dielectric displacement with the mechanical dimensions stress and deformation tensor. For Rayleigh waves on GaAs, the mechanical displacements and the piezoelectric components lie in the so-called sagittal plane. That is the plane spanned by the direction of propagation and the surface normal. The frequency of the mechanical and electric modulation is the frequency f_{SAW} of the SAW. However, both oscillations are not in phase, and even the phases of the lateral ($\mathbf{u}_\parallel$ and $\mathbf{E}_\parallel$) and vertical ($\mathbf{u}_\perp$ and $\mathbf{E}_\perp$) components are not in phase (see for example [62, 77]).

When charges are confined to a QW, the vertical piezoelectric field component $\mathbf{E}_\perp$ cannot separate electrons and holes in this QW, assuming, the electric field is moderate and the QW is not too wide. However, the vertical component can alter the PL emission energy, e.g. through the QCSE explained in section 1.8.1. Since charges in a QW are free to move in the in-plane directions, the lateral piezoelectric component $\mathbf{E}_\parallel$ may displace electrons and holes. The lateral field component alters the electronic potentials as displayed in figure 2.9. In contrast to the deformation potential modulation, the potential minima of electrons and holes do not coincidence, but are separated by $\lambda_{\text{SAW}}/2$. The IDTs used in this
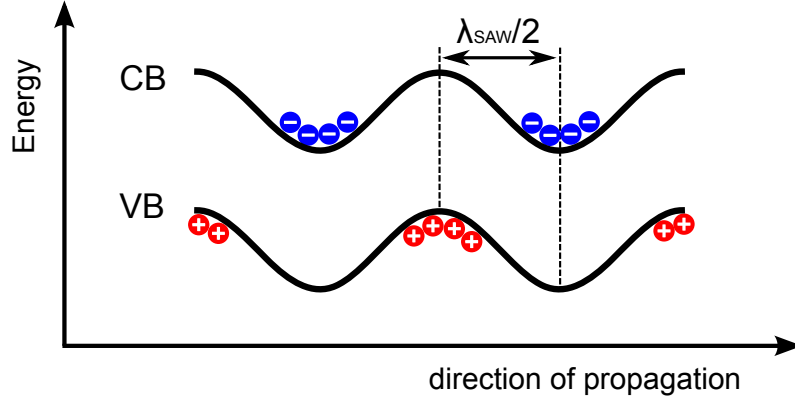
Figure 2.9: Type II band modulation caused by the acousto-electric coupling induced by a SAW. Conduction and valence band are modulated dynamically, i.e. the modulation pattern moves into the direction of SAW propagation. The charge species electrons and holes are spatially separated by $\lambda_{\mathrm{SAW}}/2$.

work have periodicities λ_{SAW} in the order of several microns which is large compared to exciton Bohr radii $r_{\mathrm{B}} \approx 10$ nm (see for example [28]). Therefore, electrons and holes are spatially separated and interaction between both species is impeded resulting in a reduced recombination rate. The modulation caused by the piezoelectric field of the SAW is a *type II modulation*. Typical amplitudes of the potential modulation are $\Delta E = 50 - 150$ meV for SAWs on GaAs with frequencies in the order of $f_{\mathrm{SAW}} = 1$ GHz and an acoustic power of about $P_{\mathrm{SAW}} = +10$ dBm [82]. This SAW power is sufficient for exciton dissociation in QWs which occurs for field strengths in the order of $\mid \mathbf{E} \mid = 10^3$ V/cm.

Both the deformation potential and the acousto-electric coupling modulate the energy band structure. In the case of a type II modulation, the oscillating CB and VB potentials are in phase, whereas both bands are inversely phased for type I modulation. Therefore, charge carriers are displaced differently, as shown in figures 2.7 and 2.9, respectively. On piezoelectric materials, both modulation types have to be considered. However, the two modulations contribute differently. Calculations show that for SAW frequencies in the order of $f_{\mathrm{SAW}} = 1$ GHz, the deformation potential effects much less modulation than the piezoelectric part [62].[1] The two modulation types become comparable at SAW frequencies exceeding $f_{\mathrm{SAW}} = 50$ GHz.

Since the strain induced part of band modulation can be neglected for the SAW parameters and materials used, only the acousto-electric modulation contributes significantly to the modulation. An important feature of the type II band modulation is that the piezoelectric field of the SAW dissociates optically generated excitons. As a consequence, the PL light emitted by a QW is quenched [62, 63]. The dissociated excitons are separated into electrons and

---

[1]A SAW with frequency $f_{\mathrm{SAW}} = 840$ MHz and a power of $P_{\mathrm{SAW}} = +13$ dBm generates a modulation of $\Delta E = 15$ meV caused by the mechanical deformation, whereas the piezoelectric modulation $\Delta E = 0.78$ eV is about 50 times larger [62].

holes which relax to their energetically favorable "stripes" of the SAW. The recombination of charges is impeded because the stripes for the two carrier species are separated by $\lambda_{\text{SAW}}/2$. Furthermore, the stripes themselves move with the propagating SAW giving rise to a transport of both charge species. This type of transport is called *bipolar charge transport* or *charge conveyance effect.*

The transport of charges is stopped if the band modulation is lifted. This can be realized for example by a metal electrode located in the sound path of the SAW. The metallic layer forms an equipotential which screens the piezoelectric potential modulation. This results in flat conduction and valence bands neglecting the weak perturbation due to deformation potentials. Therefore, the spatial separation of carriers is lifted giving rise to radiative recombination and PL emission at the edge of the metallization [63].

2.3.3 Remote carrier injection into QD nanostructures

In the previous section, the bipolar charge transport in QWs is explained. This type of SAW induced charge transport can be used to extract PL light from locations which are distinct to the area of exciton generation. Wiele et. al. proposed this transport mechanism in order to inject charges into a remote QD [82].

In figure 2.10, the mechanism of remote carrier injection is explained illustratively. At the left side of the schematic, excitons are generated by a laser. The piezoelectric field of the SAW dissociates the excitons and both carrier species relax to their respective potential minima. Because of a type II band modulation, the two carrier species are separated by $\lambda_{\text{SAW}}/2$ and move with the propagating SAW. At the right side of figure 2.10, a QD locally distorts the electronic bands resulting in little potential dips. In the illustration, the QD is first occupied by a single electron. After a half SAW period $T_{\text{SAW}}/2$, the subsequent stripe filled with carriers of opposite charge arrives and a hole is captured by the QD. Subsequently, the QD emits a single photon. The procedure recurs every SAW cycle resulting in a periodic emission of single photons. In the case of a single QD or QP, a non-classical light source is implemented.

Limitations of this single photon source arise from the carrier capture process. If the density of charges per stripe is too low, the probability for the capture process decreases. Both the laser intensity and also the SAW power determine the carrier densities. Therefore, these parameters have to be chosen carefully. Furthermore, the occupation of the QD with multiple charges have to be considered. In figure 2.10, the occupation with only one electron and one hole is sketched. Depending on the charge density, multi-exciton complexes are generated resulting in multiple PL lines. Moreover, the jitter of the SAW degrades the deterministic character of the SPS causing variations in the light emission in the order of several percent [82].

Significant experimental work has been pioneered by Bödefeld et. al. achieving remote carrier injection into an ensemble of strain-induced QDs [10]. Since
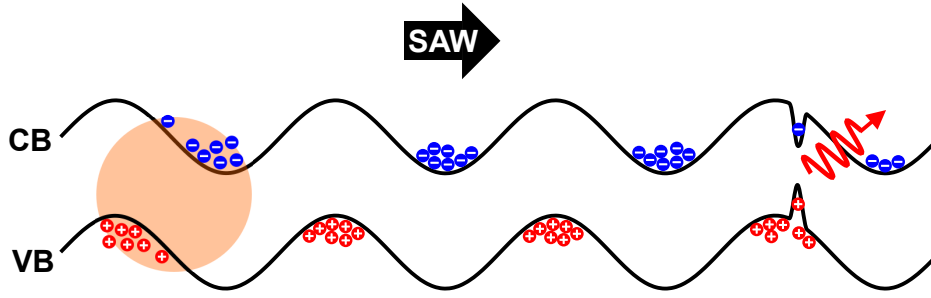
Figure 2.10: Schematic of remote carrier injection. The orange circle depicts the laser spot, i.e. the area of exciton generation. The piezoelectric field of the SAW dissociates the excitons and induces a bipolar charge transport. The band potentials are locally lowered at the QD position giving rise to a subsequent capture of electrons and holes into the nanostructure and a SAW triggered emission of PL light.

strain-induced QDs are fabricated by the deposition of InP islands on top of the substrate surface, the stressor islands can be removed selectively after the growth process using wet chemical etching. Thus, areas with and without strain-induced QDs can be defined on the sample. Additionally, a focusing transducer was used. This type of IDT focuses the sound path to a small spot on the sample. By focusing SAWs on the boundary of an unetched area, the deterministic injection of ensembles consisting of approximately 100 strain-induced QDs was achieved.

Instead of using focusing transducers, the area of remotely pumped QDs can be restricted by combining chemical etching of stressor dots with lithographically defined masks [70]. Hence, small fields of strain-induced QDs can be defined with field sizes of several µm. Figure 2.11 shows the PL emission of an ensemble consisting of approximately 750 strain-induced QDs. The white dashed square indicates the total dimensions of the QD field. PL emission is only detected from areas in the field facing towards the SAW and the laser spot.

Another approach for the injection of charges into remote nanostructures was realized by Cuoto et. al. [15] using a substrate which was pre-patterned with triangular 2 µm wide mesas. In the subsequent epitaxy process, the deposited material preferentially accumulates at specific oriented mesa edges forming short quantum wires (SQWR) embedded in a QW. Like in the aforementioned QD systems, the QW is used as a channel for a SAW assisted bipolar carrier transport. Subsequently, the carriers are captured by the SQWRs emitting characteristic PL lines. Since the SQWRs are defined due to pre-pattering, their positions can be determined deliberately.

In contrast to self-assembled embedded QDs and QPs, the localization of strain-induced QDs and SQWRs can be controlled. In the case of strain-induced QDs, post-growth isolation by selective removal of the stressor islands is possible, and the position of a SQWR is defined by pre-patterning. The investigated self-assembled QDs and QPs lack these unique properties. On the other hand, the
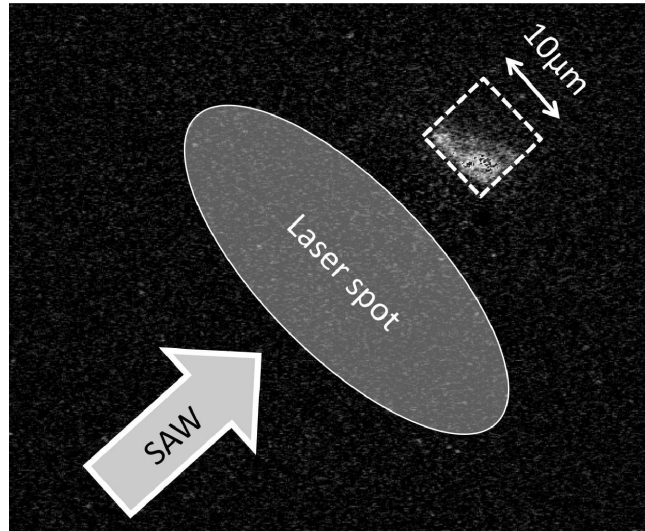
Figure 2.11: Injection of carriers into an ensemble of stress-induced QDs. The entire area of the QD field, the position of the laser spot and the propagation direction of the SAW are marked accordingly. From [69].

studied self-assembled embedded structures show excellent optical properties reflected by sharp and intense PL lines which can be assigned to specific exciton transitions. Furthermore, individual QDs/QPs can be isolated in regions of low surface density using a microscope objective of high optical magnification. Alternatively, QDs belonging to a small ensemble can be distinguished by their emission lines. Since there is a statistical distribution of QD compositions, geometrical aspects, strain etc., the particular transition energies are also statistically distributed. That makes it probable to have QDs emitting luminescence at different wavelengths. Particularly, the high optical qualities of self-assembled embedded dots/posts in combination with a 2-dimensional transport channel make them ideal candidates for the demonstration of remote carrier injection.

Chapter 3

Setup and sample layout

In this chapter, technical issues concernig the experimental setup, measurement techniques and sample preparation are explained. For the measurements, basically a µ-PL setup together with a cold-finger cryostat is used. The used setup is organized in a modular and versatile way allowing for different measurement methods. These methods integrate spectral, spatial and temporal resolution of the experiment which are described in the following section. Since the wafer material shows gradients of nanostructure densities, a suitable sample piece must be isolated. The required procedure for the isolation are explained at the end of this chapter.

3.1   µ-PL setup

In figure 3.1, a schematic of the experimental setup is provided. Since the occupation probability of electronic levels depends on temperature, low temperatures are required for spectroscopy on semiconductor QDs and QPs. Here, a continuous flow cryostat *ST-500 (Janis Research)* is used which offers a short working distance between sample and magnification optics. The sample is not immersed in the cryogen helium, but sits on a cold finger which is cooled by a continuous helium flow inside. This type of cryostat is relatively compact allowing for mounting on stages for coarse positioning. Moreover, helium is only consumed during operation and samples can be changed relatively fast. The helium flow is maintained by using a pump at the vent of the cryostat. In this configuration, temperatures less than the temperature of liquid helium $T = 4.2$ K can be achieved. For the measurements presented in this thesis, mostly temperatures in the range of $T = 4 - 10$ K are used. A window sitting approximately $d = 1$ mm above the sample allows for entering the laser light and leaving the emitted PL light. The cryostat is equipped by four coaxial transmission lines allowing for the transmission of high-frequency electric signals.

Laser light is used for the excitation of the sample. A helium-neon laser emitting light at $\lambda_\text{L} = 632.8$ nm and several diode lasers can be integrated in the setup by tilting mirrors. The intensity of the helium-neon laser is not tunable. Instead, a set of neutral density filters is used in order to attenuate the intensity to the desired level. Figure 3.1 shows a configuration with a diode laser operated in pulse mode. Two laser heads *LDH-P-660* and *LDH-P-850 (PicoQuant)* emitting light at $\lambda_\text{L} = 661$ nm and $\lambda_\text{L} = 855$ nm can be used for the generation of $\Delta t_\text{L} \approx 50$ ps short laser pulses. The intensities of both lasers can be tuned and the emitted laser pulses can be synchronized with the SAW oscillation. Because of the greater flexibility, mostly, a pulsed laser is used in a configuration which is shown in figure 3.1. If not stated differently in the plots, the red diode laser ($\lambda_\text{L} = 661$ nm) is used.

Several filters are part of the setup. The incoming laser light passes through a bandpass filter (BP) which is transparent only for a small wavelength range around the laser line λ_L. A power meter, which is attached to the optical
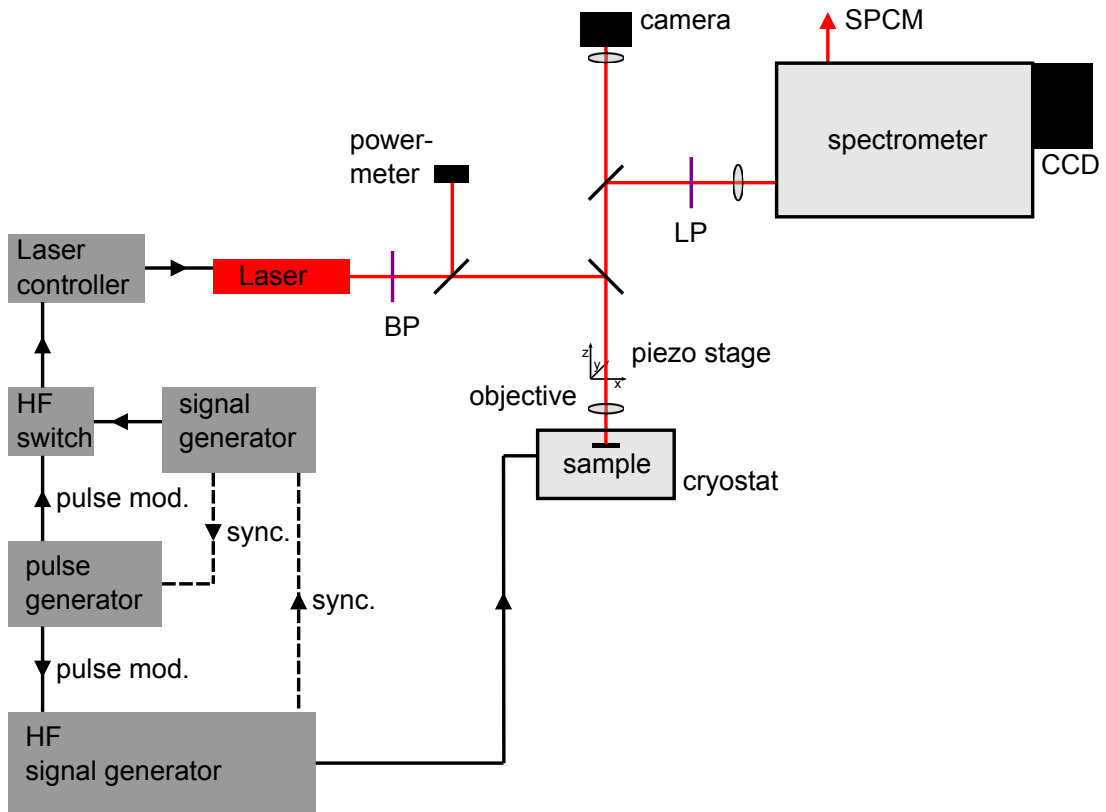
Figure 3.1: µ-PL setup in the commonly used configuration. The laser is a diode laser operated in pulse mode. A power meter attached to the light path monitors the laser intensity. The laser focus is positioned relatively to the sample by a piezo stage which moves the microscope objective. The sample is mounted inside a continuous flow cryostat. A HF signal generator supplies the signal for the IDTs. The emitted PL light is dispersed by a spectrometer and recorded by a CCD-array. Optionally, a live image of the sample can be recorded by a conventional camera.

path by a beam splitter, monitors the laser intensity. Then, the laser light is reflected by a second beam splitter which is mounted inside a *Olympus* microscope setup. This beam splitter is dichroic, i.e. the short-wave laser light is preferably reflected and the long-wave PL light is preferably transmitted. The laser light is focused on the sample by a microscope objective with a magnification of $M = 50$ and a numerical aperture of $NA = 0.55$. A piezo stage supports the microscope objective allowing for fine positioning. The emitted PL light is collected and collimated by the same objective. Then, it is transmitted by the aforementioned beam splitter and detected by the spectrometer or an optional camera. The additional camera is used for monitoring and selecting a suitable region on the sample and provides a live image of the sample.

For spectral analysis of the PL emission, a 0.5 m single monochromator (*SP2500i, Princeton Instruments*) is used. The spectrometer has a liquid-N_2 cooled Si charge-coupled device (CCD) attached for multichannel detection (*Spec-10:2K, Princeton Instruments*). Optionally, the dispersed PL light is coupled to a glass fiber and detected by a Single Photon Counting Module (*SPCM-AQRH-13-FC, Perkin-Elmer*). For time-resolved experiments, a time-correlated single photon counting board (*TimeHarp 200, PicoQuant*) is available providing time resolution of better than $\Delta t = 40$ ps.

In order to synchronize laser and SAW, a HF signal generator *SME03 (Rohde&Schwarz)* feeding the IDT gives a $f = 10$ MHz reference signal to a second signal generator *33250A (Agilent)* triggering the laser. Then, both generators are coupled allowing for phase locked measurements described in section 3.4. By operating the IDTs, heat is dissipated on the sample altering the PL signal emitted by the sample. In order to minimize heating effects, both the laser and the SAW trigger signals are modulated by a *DG535 (Stanford Research Systems)* pulse generator obtaining a duty cycle with the laser and the SAW turned off 90 % of the time (see section 3.3). The rectangular pulse for the SAW signal is directly fed to the modulation input of the HF signal generator. The signal generator providing the trigger for the laser cannot be modulated directly. Therefore, an additional HF switch is used in order to mix the trigger signal and the rectangular pulse. For the phase locked measurements, the pulse generator is additionally synchronized by the $f = 10$ MHz reference signal of a second signal generator. This second synchronization ensures that the number of emitted laser pulses per duty cycle is independent from the adjusted relative phase between laser and SAW.

3.2   Image mode

For spectral analysis, the emitted light is dispersed by a spectrometer and then detected by a CCD. An 1-dimensional data array of PL counts is obtained and spectral information is provided by a calibration which assigns the data points to particular wavelengths. In principle, an 1-dimensional array of pixels would
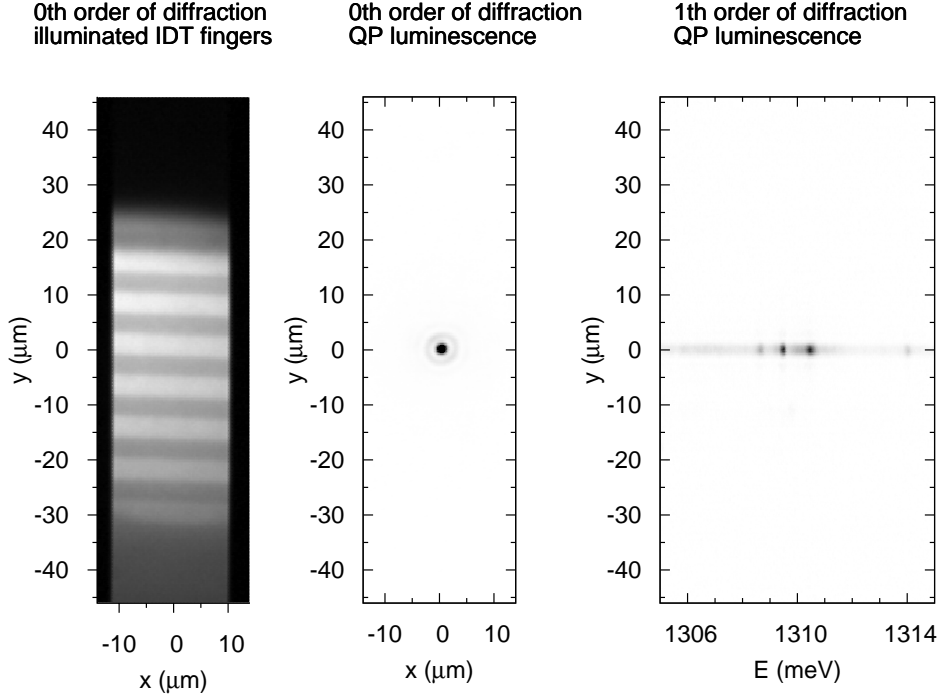
Figure 3.2: Three examples of *image mode* recordings. Left: Grating is set to the 0th order of diffraction. The CCD is used as a conventional camera. Here, the finger of an illuminated IDT are displayed. Center: Same settings as in the left image. Instead of imaging an illuminated object, PL light of a single QP is detected. Right: Grating is set to the 1th order of diffraction yielding a combination of spectral and spatial resolution.

suffice in order to provide spectral information. The CCD of the spectrometer used here is a 2-dimensional array of pixels (2048x512). For spectral recordings, the counts of vertically aligned pixels are integrated (*binned*) achieving higher signal-to-noise ratios and shorter integration times compared to 1-dimensional pixel arrays. Instead of integrating the pixel rows, the entire CCD array can be read out pixel by pixel obtaining a 2-dimensional intensity array. This method is called *image mode*.

Depending on the grating position, different cases must be considered. If the grating is positioned to the 0th order of diffraction, the light is reflected as from a mirror. Thus, no spectral information is obtained and the CCD provides a spatially resolved image from the sample as from a conventional camera. An example of such an image is shown in figure 3.2 (left panel) displaying the fingers of an IDT illuminated by a white light source. Moreover, objects emitting light themselves can be displayed by this technique. In the center panel, the PL emission of an individual QP is shown. There, the laser line exciting the post and the PL emission from the matrix-QW are blocked by a long-pass filter.
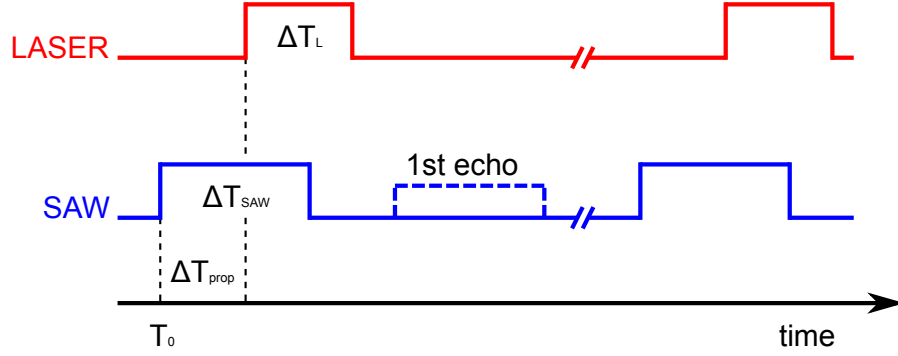
Figure 3.3: Schematic of the duty cycle used to avoid heating of the sample. The start point of the laser trigger is shifted relative to the start point of the SAW trigger taking into account the delay caused by the propagation of the SAW.

If the grating is positioned to the 1th order of diffraction as for common spectral recordings, spatial resolution is lost in one direction of the intensity array, instead a combination of spectral and spatial resolution is obtained. This is shown in the right panel of figure 3.2. Again, luminescence from an individual QP is displayed and several spectral lines of different exciton transitions are observed which are hidden in the previous image.

In summary, the *image mode* is presented which is based on a simultaneous readout of the entire spectrometer CCD-chip. In contrast to pure spectral recordings, spatial information and a combination of spectral and spatial information can be obtained by using this method.

3.3 SAW duty cycle

SAWs can cause significant heating of the sample. On piezoelectric materials this is mainly due to acousto-electric losses. The heating of the sample can be neglected if the power of the SAW P_{SAW} is moderate. However, for high SAW power, the resulting thermal energy easily raises the temperature about several degree Kelvin. Such heating modifies the PL emission causing for example red shifts due to reduced band gaps and broadening of spectral lines. These side effects have to be separated from the influence of the piezoelectric field of the SAW. Therefore, the SAW is mostly applied in a pulsed mode with a repetition rate of $f_{\mathrm{rep}} = 100$ kHz and a duty cycle of 1:9, i.e. the SAW is off 90 % of the time. This timing sequence significantly reduces the amount of transferred heat to the sample. As a consequence, the laser has to be synchronized to this duty cycle, otherwise the PL would be measured when no SAW is applied.

In figure 3.3, one trigger cycle of this duty cycle is depicted. As shown in the schematic 3.1, a pulse generator (*DG535, Stanford Research*) provides rectangular signals to the HF generator operating the IDT and to a second frequency generator triggering the laser. At T_0 the SAW is switched on for a duration of

ΔT_{SAW}. The SAW propagates with sound velocity ($v_{\mathrm{SAW}} = 2900$ m/s) over the sample. Therefore, a time delay ΔT_{prop} has to be considered which is required for the propagation from the IDT to the point on the sample where the detection takes place. Hence, the laser is switched on at a subsequent time to make sure that the wave front of the SAW has already reached this point. The width of the interval ΔT_{L} determines the time over which PL is measured from the sample.

Apart from the unwanted heating of the sample, another effect has to be considered when the durations of the two intervals ΔT_{SAW} and ΔT_{L} are increased. As described before, the IDT on the sample are arranged pairwise, constituting delay lines. One IDT of this pair is used to generate SAWs. During the PL experiments the second IDT acts as a reflector of SAWs. Therefore, the lengths of both intervals ΔT_{SAW} and ΔT_{L} are chosen such that interferences of the SAW originating from the generating IDT and from the counter propagating echo of the second IDT are excluded during the laser interval. (parameters used for sample P10: $\Delta T_{\mathrm{SAW}} = 720$ ns, $\Delta T_{\mathrm{L}} = 530$ ns, $\Delta T_{\mathrm{prop}} = 460$ ns and $f_{\mathrm{rep}} = 100$ kHz).

3.4 Phase locking

A SAW generates piezoelectric fields oscillating with a frequency f_{SAW} at a fixed point on the sample. Here, frequencies of several hundreds of MHz are used. The piezoelectric field modifies the PL of the studied nanostructures. The CCD of the spectrometer typically requires integration times $T > 1$ s. Therefore, the detected PL signal is the average over an entire SAW period. For a time resolved measurement, fast detectors such as Avalanche Photo Diodes (APD) are required. These are highly sensitive semiconductor electronic devices exploiting the photoelectric effect to convert light into electric signals and allow for detection of fast processes such as PL changes caused by a SAW. In the setup, an APD is attached to the spectrometer and spectral resolution is obtained by varying the position of the grating. Since an APD is a single-channel detector, only one particular wavelength can be monitored at the same time. Fast multichannel detectors such as streak cameras and intensified CCDs lack sensitivity due to the photocathodes and phosphorus screen.

This is a disadvantage compared to time integrated spectral measurements. However, this drawback of fast detection techniques can be circumvented if time resolution is preserved at the excitation side of the experiment. Instead of using a fast detector, a pulsed laser with pulses Δt_{L} shorter than the required time resolution is synchronized to the SAW. The so-called *phase locking* method can be applied to reiterating processes such as the oscillating piezoelectric field of a SAW. This method is a stroboscopic technique where a short light flash illuminates the sample at particular points in time. In the following, details of the *phase locking* method are provided.

Figure 3.4: Illustration of phase locked mode. The SAW and the laser pulses are synchronized having a fixed relative phase. Because of the limited repetition rate of the laser f_L, the frequency of the SAW f_{SAW} is a multiple of the laser trigger rate.

The schematic of an excitation based time resolved measurement is depicted in figure 3.4. A laser with pulse lengths $\Delta t_L \approx 50$ ps excites the sample and is synchronized with the SAW oscillation. In a standard experiment, the internal oscillator of the laser driver sets the repetition rate to $f_L = 80$ MHz which is significantly smaller than typical SAW frequencies ($f_{SAW} > 150$ MHz). Hence, laser and SAW cannot be synchronized by using same frequencies. However, synchronization is also achieved for the relation:

$$f_{SAW} = n * f_L \tag{3.1}$$

where n is an integer. It is convenient to choose the highest possible laser repetition rate $f_L < 80$ MHz such that an integer multiple results in the resonance frequency of the IDT f_{SAW}. As already explained in section 3.3, typically a duty cycle of the SAW and the laser are used to avoid heating effects. Therefore, both timing schemes have to combined if the SAW power is high enough to cause significant heating or if SAW reflections from a second IDT or the sample edge are expected.

3.5   Sample layout

In this section, the process flow of sample fabrication is described. This procedure can be readily applied for both systems, QD and QP. In the following, the discussion is restricted to QPs.

In order to perform spectroscopy on single QPs in a μ-PL setup, low surface densities of these quantum structures are required. The density should be low enough to isolate a single QP, but not too low in order to locate a QP in an adequate time. A convenient approach to fabricate material with a suitable surface density is to realize a gradient along one axis of the substrate by stopping the wafer rotation during deposition of the QP layers [42, 48]. To find the right density in-between, first an approx. 20 mm long and 5 mm wide piece is
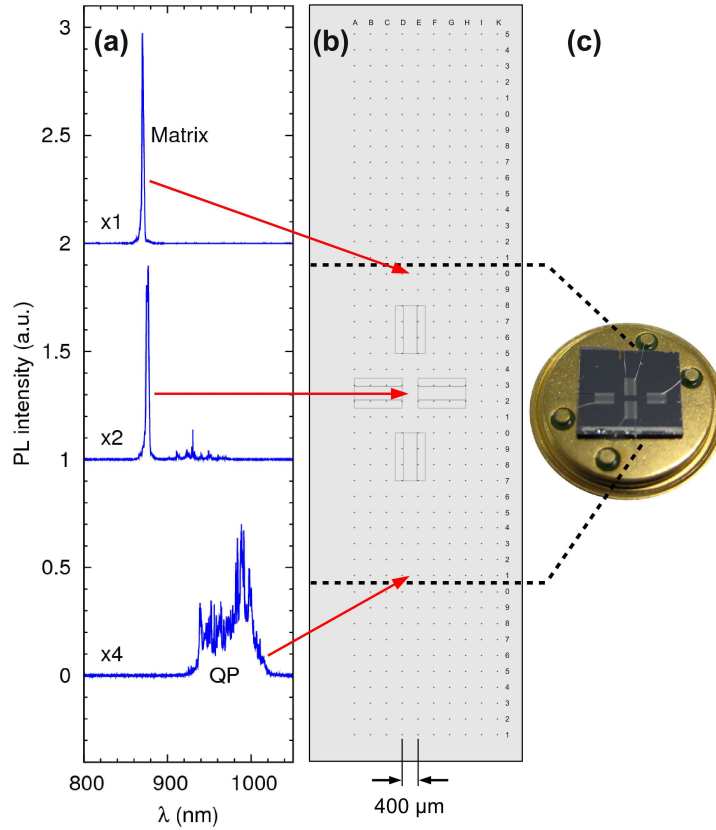
Figure 3.5: (a) PL spectra taken with respect to a lithographically defined grid. (b) Alignment of IDTs with respect to a QP surface density gradient. (c) Photograph of the mounted sample.

cleaved out of the wafer on which the suitable region is expected. Using electron beam lithography, cross-hair markers are processed on this wafer piece. These markers are positioned on a grid with a sufficiently wide spacing for the IDTs which are fabricated in the following step. An example of such a layout is shown in figure 3.5 for which the distance between two single markers is $\Delta d = 400$ µm. The entire piece is scanned from the bottom to the top and PL spectra are recorded for every point on the grid. Figure 3.5 (a) shows three example spectra in the high surface density area (lower spectrum), the low surface density area (middle spectrum) and a region without QPs (upper spectrum), respectively. Arrows in figure 3.5 indicate the positions at which these spectra were taken. As the sample is traversed, the characteristic exchange between the emission of the QPs and the surrounding matrix is observed. In the center part, a few individual sharp emission lines are observed which originate from isolated QPs which can be studied individually.

After this characterization, the region of low QP density is isolated from the wafer piece and IDTs are fabricated in a third step. The outlines of four IDTs forming two delay lines are shown in figure 3.5 (b). The IDTs were fabricated

aligned to the grid used for determining the low surface density region. The
vertical delay line is longer than the horizontal one to cover a wider range of
QP density. Finally, the sample is mounted on a sample holder and the contact
pads of the IDTs are wire bonded to the contact pins of the standard transistor
sample holder. A photograph of the final sample is presented in figure 3.5 (c).

Chapter 4

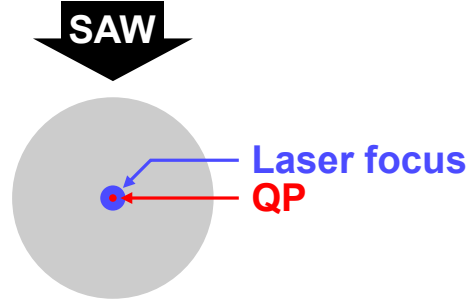# Single nanostructures and SAWs

Figure 4.1: Schematic of a directly excited QP. The grey circle illustrates the microscope aperture.

4.1 Directly excited QPs

In section 1.7, the PL of QPs and the origin of the different spectral lines are explained. Charge carriers are excited by a laser and are captured by the QPs emitting characteristic PL lines. If an external electric field is applied to the sample, these charges are influenced and subsequently the PL emission from those nanostructures is altered (see also section 1.6). To apply an electric field however, the sample has to be contacted. For this purpose, nanostructures are part of a diode junction, and metallic contacts on top of the sample provide an electric connection to a voltage source. However, some drawbacks arise from this method. First, the surface of the sample is no longer free. Thus, the metallic layer on top must not cover the entire surface to ensure that optical excitation and emission is not impeded. Second, diode junctions have a finite capacitance which limits the switching speed of the electric field applied. To circumvent these drawbacks, another experimental method of applying electric field to the QPs is chosen. The dynamic piezoelectric field of a SAW is used for this purpose. In contrast to aforementioned method, the electric field is not static, as the SAW propagates with sound velocity ($v_{\mathrm{SAW}} = 2900$ m/s on GaAs). Therefore, the dynamic character of the SAW has to be considered. Moreover, it turns out that the propagation of the SAW can be used for a controlled charge carrier transport.

All PL measurements provided in this section are performed under direct excitation of the nanostructure, which means that the laser focus and the studied nanostructure are aligned and lie in the middle of the microscope aperture. Figure 4.1 shows this experimental configuration schematically.

4.1.1 Quenching of QW luminescence

The QP structures are embedded in a matrix with an indium concentration of about $c_{\mathrm{In}} = 10$ %. The thickness of this matrix layer is the same as the height of the grown QPs. Since the matrix is surrounded by pure GaAs, it can be considered as a QW. In the case of the $d_{\mathrm{QP}} = 23$ nm QP sample, the matrix emits PL light at a wavelength of $\lambda = 875$ nm ($E = 1418$ meV).
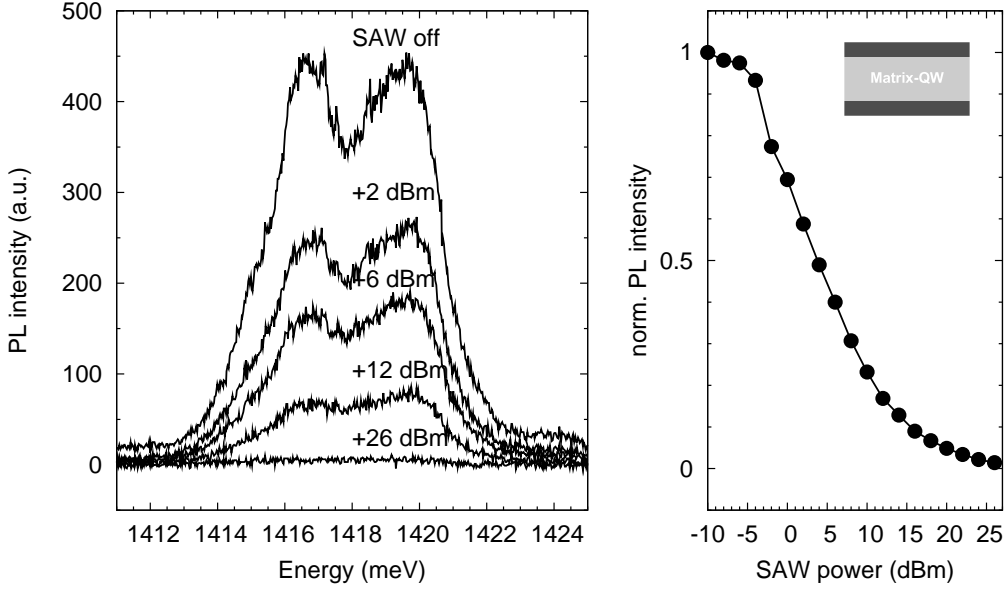
Figure 4.2: Quenching of the matrix-QW luminescence. Left: Spectral data for various SAW power levels. The double peak structure is likely artefactual since etaloning of the spectrometer CCD modulates the PL data significantly. Right: Integrated and normalized PL intensities plotted as a function of SAW power. The SAW frequency is $f_{\mathrm{SAW}} = 192.9$ MHz. Laser parameters: $\lambda_{\mathrm{L}} = 661$ nm, $P_{\mathrm{L}} = 72$ nW.

The left diagram in figure 4.2 shows matrix PL spectra. The curve with maximum intensity corresponds to the measurement without SAW. By increasing the SAW power P_{SAW}, the PL signal is quenched. At the highest power $P_{\mathrm{SAW}} = +26$ dBm almost no PL is detected from the matrix. The quenching behaviour is analyzed quantitatively by integrating the entire QW peak and plotting these integral intensities as a function of the SAW power as shown in the right panel of figure 4.2. Quenching already sets in at the lowest power levels, but from $P_{\mathrm{SAW}} = -4$ dBm on, a drastic decrease of PL emission is detected which continues with increasing SAW power. At a power of $P_{\mathrm{SAW}} = +4$ dBm, the signal drops to 50 % relative to the level without a SAW present. From $P_{\mathrm{SAW}} = +12$ dBm on, the slope of the integrated PL intensity reduces. The double peak structure observed for the matrix luminescence is likely artefactual, since the detector shows a etalon-like behaviour in the near infrared. Reflections between the nearly parallel front and back surfaces of the CCD cause unwanted fringes of constructive and destructive interferences which artificially modulate the spectrum.

The observed quenching behaviour of the matrix-QW luminescence can be explained by the charge conveyance effect [63] described in section 2.3.2. The piezoelectric field of a SAW dynamically modulates the band edges of the QW giving rise to a local dissociation of charge carriers at the point of laser excitation and PL emission/detection. Due to the spatial separation of electrons and holes, recombination and subsequently PL emission is reduced.
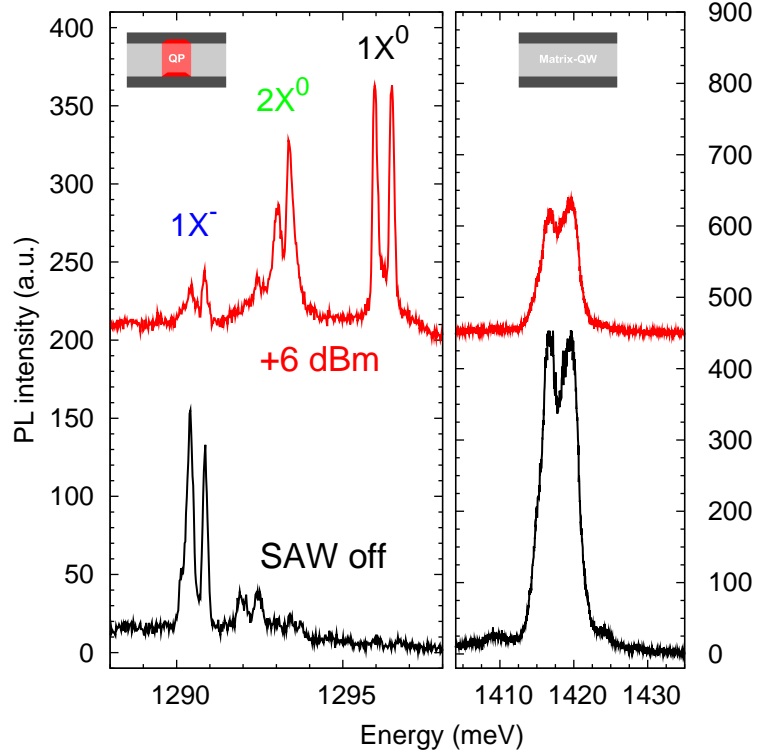
Figure 4.3: PL spectra with (top) and without (below) SAW. Left panel: Switching between different exciton transitions emitted by an individual QP. Right panel: Quenching of QW luminescence. $f_{SAW} = 193$ MHz, $P_L = 72$ nW.

4.1.2 Switching of QP lines

The quenching behaviour of the 2-dimensional matrix is well understood. For systems with lower dimensionality such as QPs, the situation becomes more complicated. According to the discussion in section 2.3.2, the piezoelectric field of a SAW dominates the interaction with excited charges. Therefore, similar experimental findings are expected as when the sample is exposed to a static electric field realized through diode structures [41]. In contrast to those experiments, the piezoelectric field of a SAW oscillates periodically at high frequencies f_{SAW}. Moreover, the SAW period T_{SAW} possibly becomes comparable to exciton recombination times τ.

In order to investigate the influence of a SAW on the QP luminescence, first the configuration of direct excitation shown in figure 4.1 is applied. The left panel of figure 4.3 shows PL spectra of an individual QP for two cases: The lower spectrum is measured without SAWs and the upper spectrum with SAWs propagating across the laser focus. Supplementary, PL spectra of the matrix-QW are shown on the right panel, again with and without SAWs. The matrix PL shows the well known quenching behaviour explained above, whereas the characteristic of the QP is completely different, and a switching between different emission lines is observed. Without SAW, the QP emits more light from the
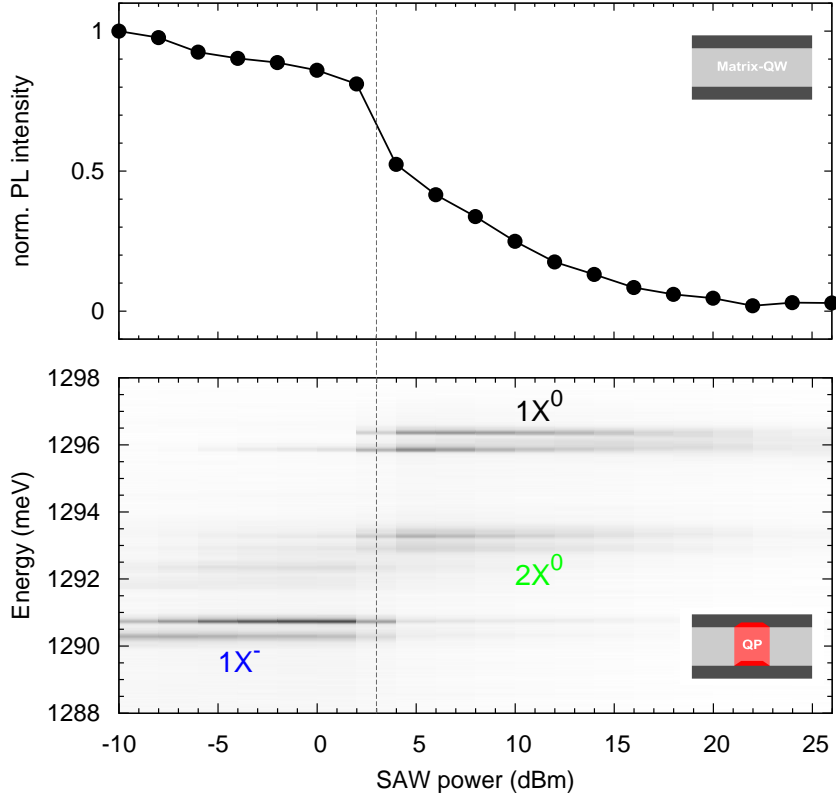
Figure 4.4: Upper panel: Integrated PL of the matrix-QW ($E = 1418$ meV) plotted as a function of SAW power. Lower panel: SAW power series of a single QP. The vertical line indicates the threshold SAW power for the PL switching. $f_{SAW} = 193$ MHz, $P_L = 72$ nW.

lower energetic transitions, i.e. peaks of the $1X^-$ exciton. With SAWs applied, the emission is redistributed from the transitions with lower energy towards those with higher energy. The $2X^0$ and $1X^0$ transition are enhanced and the afore dominant $1X^-$ transition is strongly suppressed.

For a detailed analysis, the SAW power P_{SAW} is varied over a wide range from $P_{SAW} = -10$ dBm to $P_{SAW} = +26$ dBm. Measured spectra are plotted in a grey scale representation (lower panel of figure 4.4) as a function of the SAW power. The data clearly shows that the PL switching occurs around a very narrow power range at $P_{SAW} = +3 \pm 1$ dBm. The switching of the QP emission lines coincides with the simultaneous decrease of the matrix intensity at its steepest slope as indicated by the vertical line in figure 4.4. This strongly suggests that both processes are linked to each other.

The observed behaviour can essentially be explained by a charge conveyance effect in the matrix-QW layer. Figure 4.5 illustrates this process schematically. Because of the deeper QP confinement potential, excited charge carriers
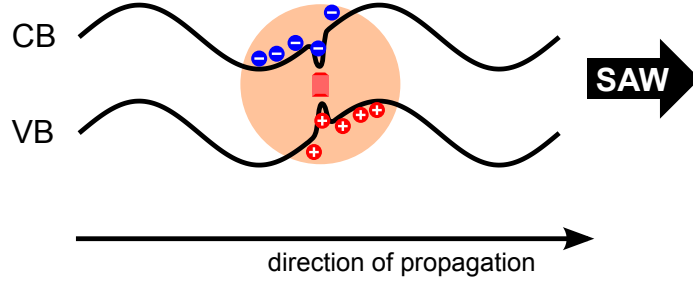
Figure 4.5: Schematic of SAW induced band modulation of a directly excited QP. The orange circle illustrates the laser spot. Electrons (blue) and holes (red) are acoustically conveyed and eventually trapped by the deeper QP potentials.

are trapped by these nanostructures. In contrast to previous PL measurements without SAW, the potential of the surrounding QW matrix is modulated by the piezoelectric field of the SAW. As indicated in the schematic, the spatial carrier distribution is different for each species, since negatively charged electrons and positively charged holes relax to opposite half cycles of the SAW. Due to the propagation of the SAW, the QP is preferably filled with one carrier species, and after $T_{\mathrm{SAW}}/2$ with the other species. Therefore, predominantly neutral exciton complexes are observed. As the charges are driven into the QP by the SAW, the SAW assisted carrier capture is rather deterministic in contrast to a direct excitation by the laser where the distinct capture probabilities of electrons and holes are determined by the particular composition of the QP.

To further demonstrate the change of carrier capture, two PL series of the same individual QP are compared in figure 4.6. In the left series, the laser intensity is varied and no SAW is present, whereas in the series shown on the right side of figure 4.6, the laser intensity P_{L} is kept constant and the SAW power P_{SAW} is varied. There are mainly two differences between both series. The first one refers to the biexciton. An increase of laser intensity produces a disproportionately large increase of the $2X^0$ emission relatively to the $1X^-$ and $1X^0$ emission, as already seen in section 1.7. This is not the case for the SAW power series. On the other hand, the SAW enhances the emission from the $1X^0$ peak drastically which cannot be achieved to the same degree if the laser intensity is increased and no SAW is applied. Furthermore, a $1X^0$ doublet is observed, which probably arises from localized excitons at the two ends of the post. Both lines are comparably enhanced for a SAW power of $P_{\mathrm{SAW}} = +6$ dBm. For the laser intensity series, no pronounced $1X^0$ enhancement is observed and the low energy part of the $1X^0$ transition is always more prominent than the high energy part even for high laser intensities. If the laser intensity is increased beyond the maximum value of $P_{\mathrm{L}} = 18$ µW displayed in the left panel of figure 4.6, the background of the spectrum rises exponentially and any information about particular transitions is lost.

Despite the observed differences between both series, the two middle spectra recorded at $P_{\mathrm{L}} = 2.16$ µW and $P_{\mathrm{SAW}} = 0$ dBm, respectively, look remarkably
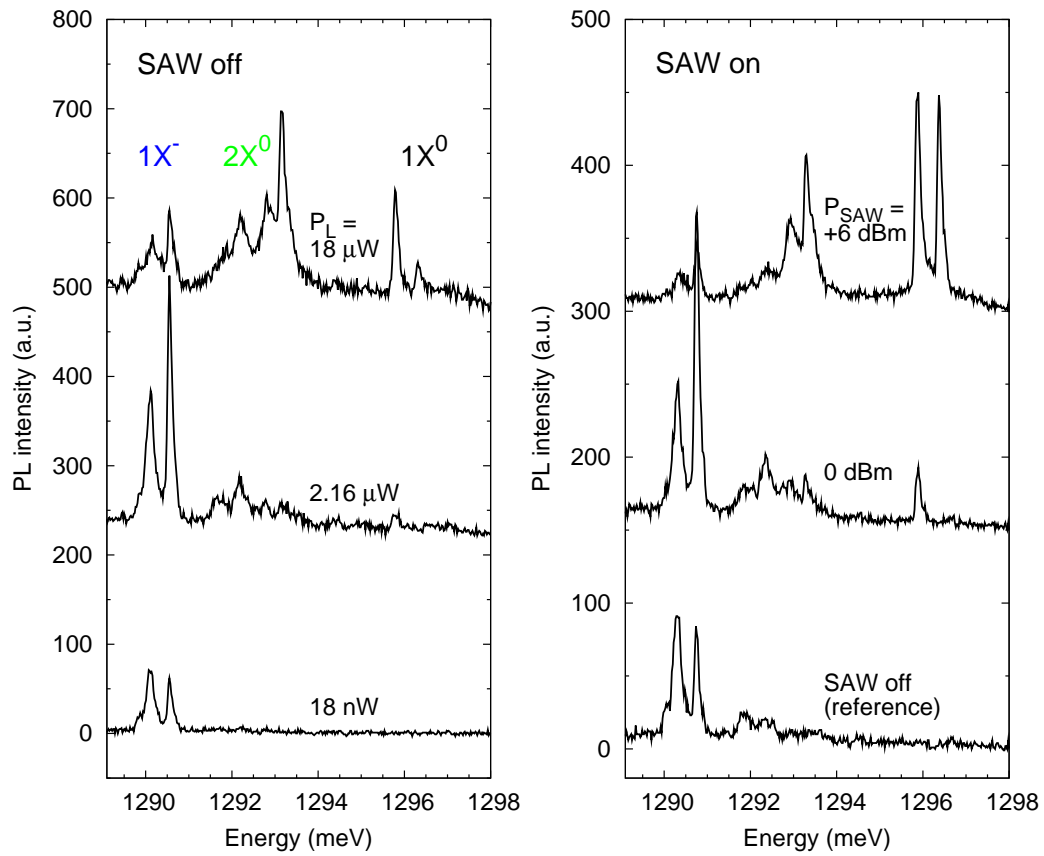
Figure 4.6: Comparison of PL spectra of the same individual QP. Left Panel: Laser intensity series, no SAW is applied. Right panel: SAW power series ($f_{SAW} = 193$ MHz), laser intensity is kept constant at $P_L = 72$ nW.

similar. According to the SAW power series on the matrix PL (see upper panel of figure 4.4), $P_{SAW} = 0$ dBm is still lower than the PL switching threshold power $P_{SAW} = +3$ dBm marked by the vertical line. However, weak quenching of the matrix PL is already observed at lower SAW power. The piezoelectric field of the SAW dissociates electron-hole pairs giving rise to an enhanced density of free carriers. These carriers are captured by the QP which subsequently emits more PL than without SAWs. A higher carrier density can also be achieved without SAW by simply increasing the laser intensity P_L. Therefore, both processes can be compared, at least for low SAW power P_{SAW}. For a SAW power higher than the threshold power, bipolar charge transport and sequential carrier injection sets in. In this power regime, the involved mechanisms are no longer similar to a simple increase of laser power P_L.

4.1.3   Splitting of QP lines

Apart from the observed switching behaviour, some nanostructures of the QP sample ($d_{QP} = 23$ nm) show additional features. In the left panel of figure 4.7, the PL of a single nanostructure is plotted as a function of the applied SAW power and the spectral energy. For this particular nanostructure, also PL switching is observed. However, a lower threshold power $P_{SAW} \approx -2.5$ dBm is required. Remarkably, some PL lines split into two separate lines, as the SAW power is increased. The splitting sets in at $P_{SAW} \approx +12$ dBm. For the transition at $E = 1321.4$ meV, the splitting energy is $\Delta E = 0.34$ meV at the highest SAW power applied.

The majority of the studied QPs do not show any splitting behaviour. Splitting is only observed for a few nanostructures and the PL emission energy of these structures is relatively high ($E > 1305$ meV). A possible explanation for the exceptional behaviour could be a strain-induced effect which has also been assumed for the splitting of QD emission lines observed by Gell et. al. [24] (see also section 2.3.1). In contrast to the larger QPs, the particle wave functions in QDs are more confined which could explain an enhanced influence of strain effects on the particular energies.

This interpretation is supported by ensemble spectra of the QP sample ($d_{QP} = 23$ nm) shown in the right panel of figure 4.7. Apart from the peak at $E_{QW} = 1395$ meV which is attributed to the QW luminescence, three pronounced emission maxima at $E_s = 1270$ meV, $E_p = 1300$ meV and $E_{QD} = 1325$ meV are observed. The peaks with energy E_s and E_{QD} are already present for the lowest laser intensity (lower spectrum), whereas the emission maximum around E_p is only observed for increased laser intensity. The peak with lowest energy is attributed to the emission from s-shell excitons occupying the quantum posts. This is also supported by a theoretical model reported in reference [30]. Since the emission maxima at E_p is only present for higher laser intensities, this peak can be attributed to p-shell excitons of the quantum posts. The peak observed at E_{QD} is also present for the lowest laser intensities and cannot be reproduced by quantum post states in the model. Probably, this emission peak is caused
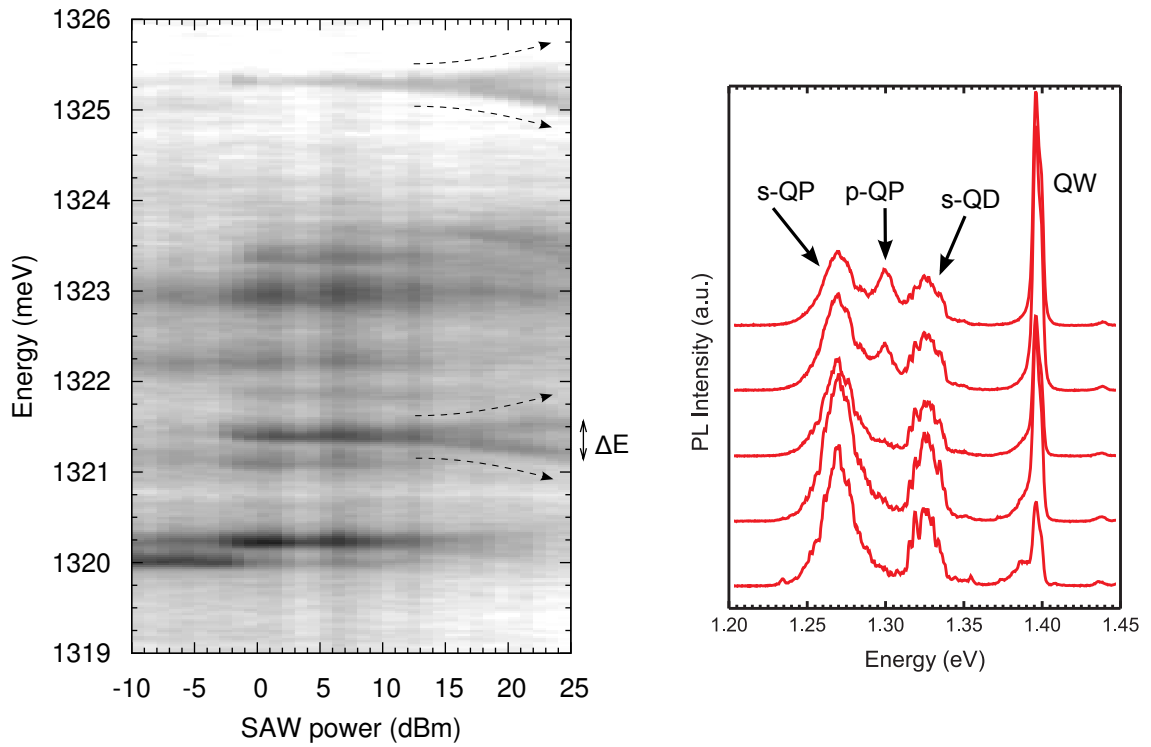
Figure 4.7: Left: SAW power series of a dot-like nanostructure ($f_{\text{SAW}} = 193$ MHz). The labeled splitting energy is $\Delta E = 0.34$ meV. Right: Ensemble spectra of $d_{\text{QP}} = 23$ nm QP sample for different laser intensities (reproduced after [30]).
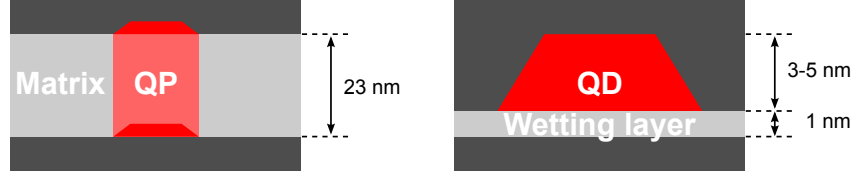
Figure 4.8: Schematic overview of the QP and QD systems. In both systems, charges are transported by the SAW within a 2-dimensional layer (matrix-QW and wetting layer). Note the different scales.

by excitons occupying dot-like nanostructures which additionally develop in the growth process, e.g. at the interfaces of the matrix-QW. Since the splitting occurs only for the dot-like structures, a similar mechanism as described in reference [24] could account for the unusual splitting characteristic.

4.1.4 Comparison with conventional QDs

QPs are coupled to a 2-dimensional QW. As already discussed, the matrix-QW plays a crucial role for the observed PL switching of individual QPs. The QW width d_{QW} is determined by the QP height which can be adjusted with nanometer precession from $d_{QP} \approx 3$ nm to $d_{QP} > 60$ nm. Here, a sample with $d_{QP} = 23$ nm high QPs is studied. In contrast, conventional self-assembled QDs are flat $d_{QD} = 3 - 5$ nm high In-rich islands with a diameter of about $D_{QD} \approx 20$ nm. QDs nucleate on a $d_{WL} \approx 1$ nm thick InGaAs wetting layer resembling a thin QW with a larger effective band gap than the QDs themselves. A schematic of the two systems is provided in figure 4.8.

The QPs and the QDs are both coupled to a 2-dimensional layer. Since the layer widths and the aspects of the QD and QP are different, the PL emission is expected to differ between both systems when a SAW is applied. To proof the distinct characteristics for QDs and QPs, SAW power sweeps are performed for both samples. The SAW power is increased from $P_{SAW} = -10$ dBm to $P_{SAW} = +26$ dBm and is decreased vice versa. The results of the QD sample are shown in figure 4.9 and those of the QP sample in figure 4.10. The QD sample, primarily emitting light from the $1X^0$ transition, shows additional lines originating form the $1X^+$ and $2X^0$ excitons when SAWs are applied. In order to assign the emission peaks of the QD sample properly, laser intensity series are performed and binding energies are compared with values from literature, as shown before for the posts.

Surprisingly, the QD emission lines differ completely for up- and down-sweeps. There is a strong hysteretic behaviour of the wetting layer PL in panel (a) of figure 4.9 which shows a non-monotonic characteristic. As for the SAW power series on directly excited QPs, a switching of the QD emission lines is observed. The threshold SAW power required to switch the PL lines is $P_{SAW} = +19$ dBm during up-sweep and is then reduced to $P_{SAW} = +10$ dBm during down-sweep. Moreover, the intensities of the QD peaks do not remain constant. A quanti-

tative analysis of selected PL lines is provided in panel (d). The QD emission lines show again a clear hysteretic behaviour. More surprisingly, the $2X^0$ peak is drastically enhanced during down-sweep. The integrated $2X^0$ intensity at its maximum is nearly a triple during down-sweep compared to the maximum PL intensity during up-sweep.

In the case of the QP sample, a conversion from the $1X^-$ to the neutral excitons $1X^0$ and $2X^0$ is observed (panels (b) and (c) in figure 4.10). This has already been shown in the power series of figure 4.4. For the QP sample, there is almost no difference in the PL pattern if the SAW power is increased or decreased. The relatively weak switching threshold power $P_{\text{SAW}} \approx +0.5$ dBm remains constant for up- and down-sweep, as indicated by a vertical dashed line. Only small deviations are observed at low SAW power for the matrix PL shown in panel (a) of figure 4.10. The curves of the integrated $1X^0$ and $1X^-$ intensities shown in panel (d) further support the non-hysteretic behaviour of the QP system.

The observed differences between the two systems can be explained by the distinct dimensions of the wetting layer and the matrix-QW, respectively. QWs have extensively been studied over the last decades. It is well known that carrier mobilities are decreased in thinner QWs due to interface roughness [66]. Moreover, for thin QWs, width variations lead to random local potential fluctuations similar to *natural* QDs localizing excitons and individual charges [4, 12]. The piezoelectric field of a SAW dissociates this additional binding to the local potential fluctuations resulting in a conversion of *bound* to *free* excitons [79]. The SAW amplitude required for this conversion is reduced for thicker QWs since weaker localization occurs due to width fluctuations. Since $d_{\text{WL}} << d_{\text{QW}}$, a stronger modification of PL switching is observed for the QD sample due to interface roughness effects. Moreover, these localization effects and the overall reduction of the mobility in the WL is more pronounced for holes compared to electrons, due to their higher effective masses.

In the thin WL, carrier mobilities are drastically reduced compared to those of the matrix-QW. As mentioned before, the transport of charge carriers in a 2-dimensional layer plays a crucial role for the PL switching assisted by SAWs. Because of the reduced carrier mobilities in the WL, switching starts at much higher power levels. On the other hand, carriers in the wide matrix-QW scatter little at the boundaries of the interfaces. They are transported by the SAW without pronounced resistance within the well. This alone cannot explain the hysteretic behaviour observed for the PL of the WL and the QD peaks. Probably, random local potential fluctuations at the interfaces of the WL trapping excitons and individual charges have significant influence on the observed hysteresis. Since the PL of a QD is sensitive to carriers trapped closely spaced to the QD or at the boundaries of the WL, the QD luminescence is modified if these charges are removed by a SAW which has been applied before.

Further experiments demonstrate that the QD system requires a time constant of $\tau \approx 1$ min. in order to relax to the primary configuration. Probably, trapping
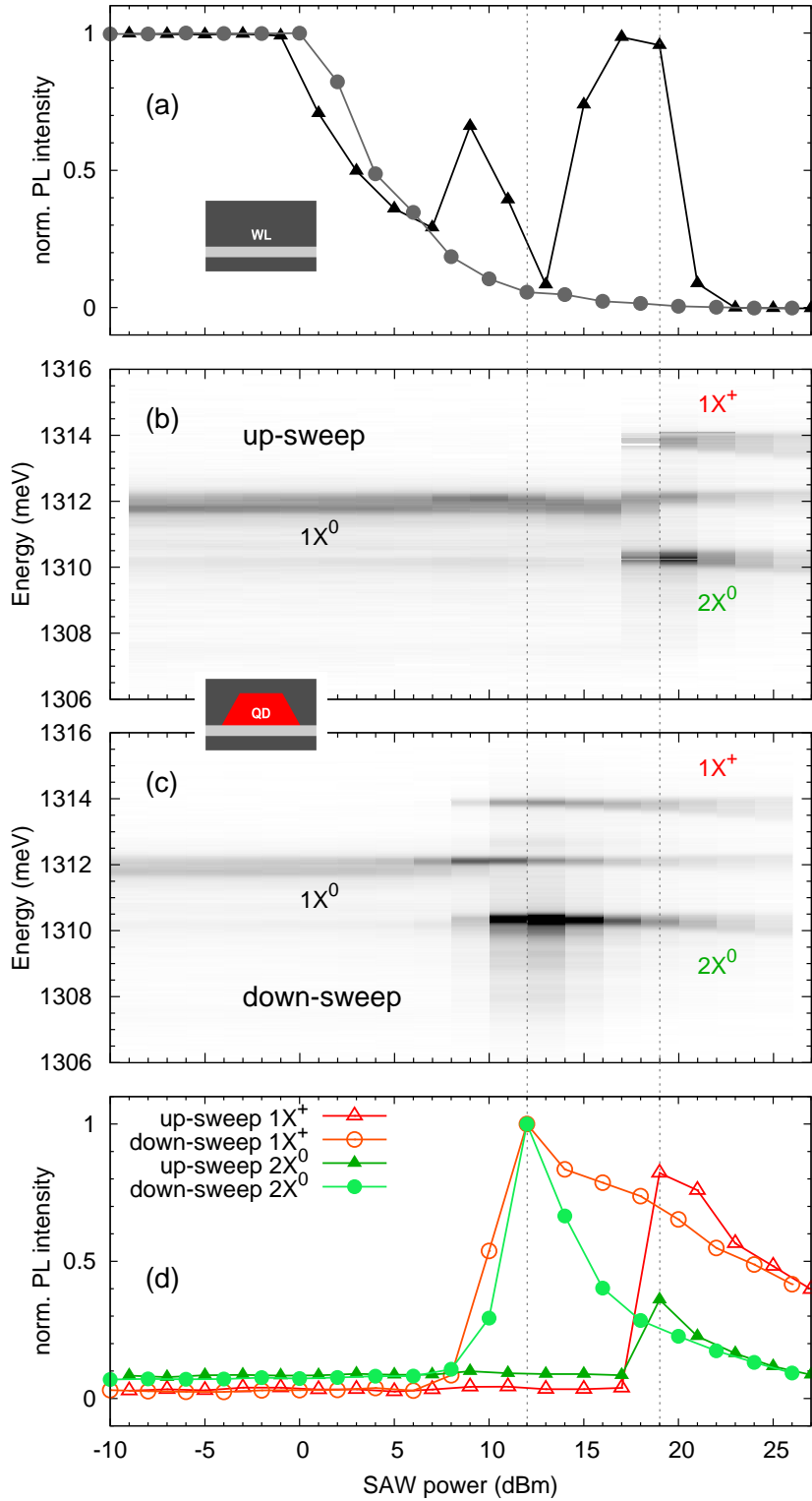
Figure 4.9: SAW power dependent PL spectra of the QD system ($f_{\mathrm{SAW}} = 251.5$ MHz). The SAW power is increased (up-sweep) and subsequently decreased (down-sweep). Panels (b) and (c) show the raw data, panel (d) the integrated PL of the $1X^+$ and $2X^0$ transitions, panel (a) the integrated WL PL. The curves are normalized with respect to the highest PL value found for each transition.

Figure 4.10: SAW power dependent PL spectra of the QP system ($f_{\mathrm{SAW}} = 192.9$ MHz, $P_{\mathrm{L}} = 72$ nW). The SAW power is increased (up-sweep) and subsequently decreased (down-sweep). Panels (b) and (c) show the raw data, panel (d) the integrated PL of the $1X^0$ and $1X^-$ transitions, panel (a) the integrated matrix PL. The curves are normalized with respect to the highest PL value found for each transition.
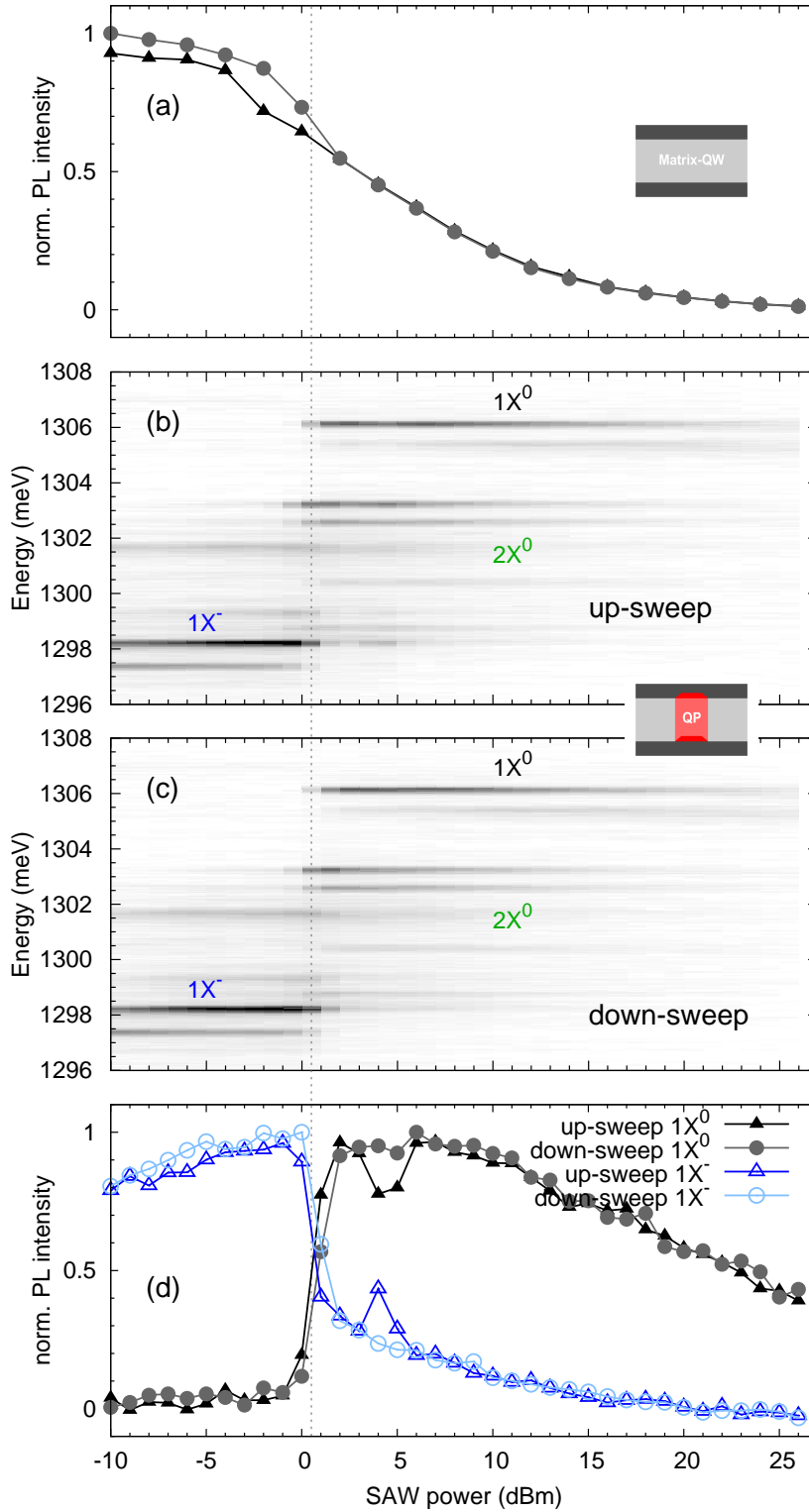
potentials play a significant role for this observation. The long relaxation times explain the hysteresis observed in the QD spectra. Because of the hysteresis, the actual PL emission depends on the SAW power applied before and possible waiting times. A way to circumvent the hysteresis and to reset the system to a defined state is applying a short SAW pre-pulse with sufficient high amplitude. In the case of the QP system, no SAW pre-pulses are required. PL switching is non-hysteretic, although interface roughness may also exist. In contrast to the QD system, the QW is significantly wider than the WL. Therefore, the surface-volume-ratio is smaller and carrier mobilities in the matrix-QW are higher than in the QD system.

4.1.5   Temporal monitoring of QW luminescence

The *phase locking* method explained in section 3.4 allows for temporal resolution of PL spectra. In a phase locked experiment, the SAW and the laser pulses are synchronized having a fixed relative phase. Temporal resolution is achieved by altering the phase successively from $\phi = 0$ to $\phi = 2\pi$.

Before performing the phase locked experiment, a suitable SAW power must be chosen. Therefore, a SAW power scan on the studied luminescence emission is done first. First, the matrix PL of the QP sample with $d_{QP} = 23$ nm is measured. A power scan for the matrix PL can be found for example in upper panel of figure 4.4. The chosen SAW power P_{SAW} should be well above the quenching edge. Then, the piezoelectric fields are expected to be high enough, in order to influence the QW luminescence significantly. On the other hand, the power level should be not too high in order to avoid complete PL quenching.

For the phase locked measurements on the matrix PL, two IDTs with periods $\lambda_{SAW} = 12.5$ µm ($f_{SAW} = 232.2$ MHz) and $\lambda_{SAW} = 5.4$ µm ($f_{SAW} = 538.3$ MHz) are used, respectively . For both SAW frequencies, a SAW power of $P_{SAW} = +10$ dBm is chosen fulfilling the afore explained conditions. Moreover, the matrix PL is measured in low density regions where no QP is excited simultaneously. Then, the pulsed laser and the SAW are synchronized as explained in section 3.4 and the relative phase is altered over a full period. The absolute phase between the laser and the SAW at the point of PL detection is unknown. Therefore, the measured PL is plotted as function of the relative phase ϕ which is set through the HF generator feeding the IDT and synchronizing the laser trigger. The upper panel of figure 4.11 exemplary shows PL data for the SAW with lower frequency and longer period.

For a quantitative analysis, the PL is integrated and normalized with respect to the integrated luminescence when no SAW is applied. The resulting data points are also plotted as a function of the relative phase between the laser and the SAW, as shown in the lower panel of figure 4.11. Blue diamonds correspond to the data shown in the upper panel and green circles correspond to a measurement with the higher SAW frequency. Solid curves are sine fits. For the low SAW frequency, a modulation depth of about 25 % with respect to the average
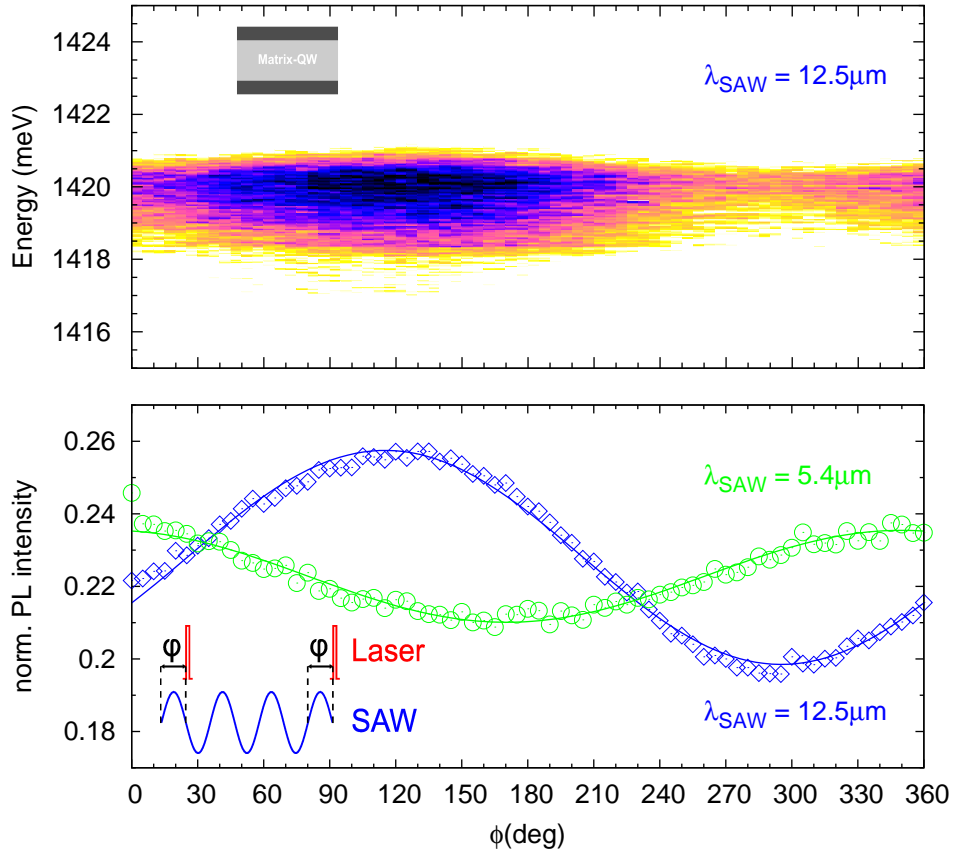
Figure 4.11: Matrix PL measured in *phase locked mode* ($P_L = 72$ nW). Upper panel: Spectra of matrix-QW as a function of relative phase between laser and SAW. SAW parameters: $P_{SAW} = +10$ dBm, $\lambda_{SAW} = 12.5$ µm ($f_{SAW} = 232.2$ MHz). Lower panel: Integrated and normalized matrix PL of spectra shown above (blue diamonds) and of a second data set with different SAW parameters (green circles): $P_{SAW} = +10$ dBm, $\lambda_{SAW} = 5.4$ µm ($f_{SAW} = 538.3$ MHz). Solid curves are sine fits. A PL intensity of 1 corresponds to the integrated QW luminescence when the SAW is switched off.
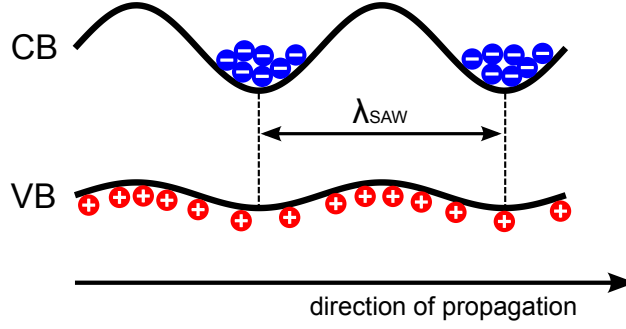
Figure 4.12: Schematic of asymmetric modulation of conduction and valence band giving rise to a $\Delta\phi = 2\pi$ PL modulation.

PL intensity is observed. For the high SAW frequency, the modulation depth is reduced to 10 %. The oscillation frequencies of both curves correspond to $\Delta\phi = 2\pi$ on the phase scale, i.e. the matrix PL shows one maximum and one minimum per cycle.

However, the absolute value of the piezoelectric field shows two maxima and two nods per SAW cycle. Since exciton dissociation is caused by the piezoelectric field, two maxima and minima are also expected in the PL signal. This discrepancy can only be solved, if the asymmetry of the two carrier species is taken into account. Due to different mobilities and effective masses of the two species, electrons and holes are influenced differently by the band modulation. Since holes have higher effective masses m^*, they cannot follow the dynamic modulation [2] to the same degree as electrons. Thus, holes are distributed more uniformly over a SAW cycle, whereas electrons are confined to one half cycle of the SAW. This situation can be expressed by different modulation amplitudes for conduction and valence band, as sketched in figure 4.12. Because of the enhanced confinement of electrons with respect to holes, the PL modulation is dominated by the phase dependent distribution of electrons. Therefore, the frequency of the modulation corresponds to $\Delta\phi = 2\pi$.

As demonstrated in figure 4.11, the PL modulation is distinct for different SAW wavelengths λ_{SAW}. That can be explained by taking into account both, the *spatial* and the *temporal* propagation of the SAW.

Important parameters are the wavelength of the SAW λ_{SAW}, the diameter of the laser spot $D_{\mathrm{L}} \approx 5$ µm and the exciton recombination time τ. The interplay of these parameters can be simulated by a mathematical model. For the *spatial* PL modulation, the time t is considered to be constant. Figure 4.13 shows the electronic potentials for two distinct SAW frequencies at a fixed time. For the high SAW frequency, the laser spot size D_{L} is comparable to the wavelength of the SAW λ_{SAW}. The emitted PL is then an average of different SAW phases. As the laser spot size D_{L} is smaller than the SAW wavelength λ_{SAW}, there is still a (small) modulation, when the relative phase between laser and SAW is altered. For the low SAW frequency, the laser illuminates only a small segment
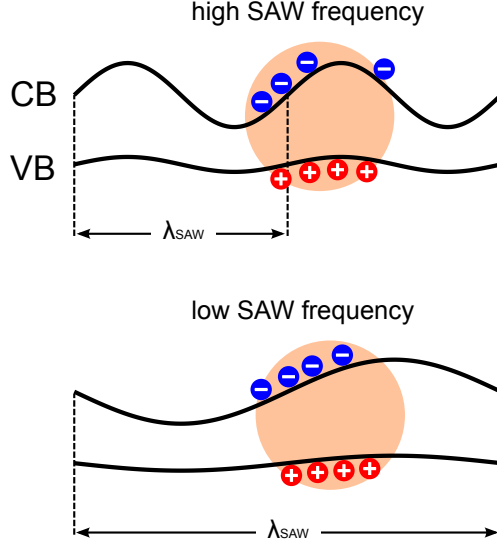
Figure 4.13: Schematic of type II band modulation induced by SAWs with different frequencies. Black curves are band potentials. Orange circles illustrate the diameter of the laser spot. Laser and SAW are synchronized such that the depicted configurations are iterated for each laser pulse (*phase locking*).

of the SAW cycle and therefore, a higher phase contrast is observed in the QW luminescence. For a quantitative analysis, the intensity distribution of the laser spot must be considered. It follows a Gaussian distribution:

$$g(x) = \frac{1}{\sigma\sqrt{2\pi}} \exp\left(-\frac{x^2}{2\sigma^2}\right) \tag{4.1}$$

where σ is the standard deviation of the Gaussian curve. This parameter is obtained from spatially resolved images of the QW luminescence (see appendix D).

For the *temporal* part of the PL modulation, the involved time constants have to be considered. The laser pulse width $\Delta t_\text{L} \approx 50$ ps is short compared to the subsequent processes and can be neglected. After excitation and before exciton formation, excited carriers relax to states with wave vectors $\mathbf{k} = 0$. The carrier relaxation processes occur on timescales between several and hundreds of picoseconds [17, 44, 64] and can be neglected in the model, too. However, the exciton recombination time $\tau \approx 1$ ns is in the order of the SAW period T_SAW, at least for higher SAW frequencies [21]. Therefore, the temporal evolution of the radiative exciton recombination have to be considered carefully. The radiative exciton recombination follows an exponential decay law:

$$d(t) = \exp\left(\frac{-t}{\tau}\right) \tag{4.2}$$

In the following, the event of one single laser pulse is considered. For comparison, the emitted luminescence intensity without SAW PL_norm is calculated by

integrating the decay curve $d(t)$ multiplied by the Gaussian distribution $g(x)$. The integration limits are chosen sufficiently large, in order to include (almost) all PL counts:

$$PL_{\mathrm{norm}} = \int_{-4\sigma}^{+4\sigma} \int_{0}^{T_{\mathrm{int}}} g(x)d(t)\,dxdt \approx \int_{0}^{T_{\mathrm{int}}} \exp\left(\frac{-t}{\tau}\right)\,dt \approx \tau \qquad (4.3)$$

A SAW with amplitude α modulates the electronic potentials temporally and spatially giving rise to an oscillating variation of luminescence which is proportional to:

$$osc(x,t,\phi) = \frac{1}{2}\alpha \sin\left(k_{\mathrm{SAW}}x - \omega_{\mathrm{SAW}}t - \phi\right) + \frac{1}{2}\alpha \qquad (4.4)$$

where

$$k_{\mathrm{SAW}} = \frac{2\pi}{\lambda_{\mathrm{SAW}}}$$
$$\omega_{\mathrm{SAW}} = 2\pi f_{\mathrm{SAW}}$$

are the wave vector and the angular frequency of the SAW. The adjusted relative phase between laser and SAW ϕ introduces a phase shift of the PL modulation. Finally, the relative change of PL intensity with respect to the luminescence without SAW is derived by integrating over the Gaussian distribution, the decay curve and the oscillating function:

$$PL(\phi) = 1 - \frac{\int_{-4\sigma}^{+4\sigma} \int_{0}^{T_{\mathrm{int}}} osc(x,t,\phi)g(x)d(t)\,dxdt}{PL_{\mathrm{norm}}} \qquad (4.5)$$

The function $PL(\phi)$ depends on the relative phase between the laser and the SAW. Generally, the values of this function are in the range between 0 (complete PL quenching) and 1 (same PL as without SAW). In order to calculate $PL(\phi)$, the exciton relaxation time τ and the standard deviation of the Gaussian laser beam profile have to be measured. The wavelength λ_{SAW} and the frequency of the SAW f_{SAW} are known parameters. The amplitude of the SAW modulation α cannot derived from physical identities and must be figured out in a heuristic manner.

According to appendix D, a standard deviation of $\sigma = 2.5$ µm is determined for the illumination spot on the sample. Using the single photon counting module together with the time-correlated single photon counting board, a recombination time of $\tau = 1.242$ ns is measured. However, the simulated $PL(\phi)$ curves do not reproduce the measured data in the lower diagram of figure 4.11 if these parameters are used. The resulting amplitudes of the simulation are too low. In contrast, the simulated curves are in good agreement with the experimental data if a long recombination time of $\tau = 8.0$ ns is assumed. In figure 4.14,
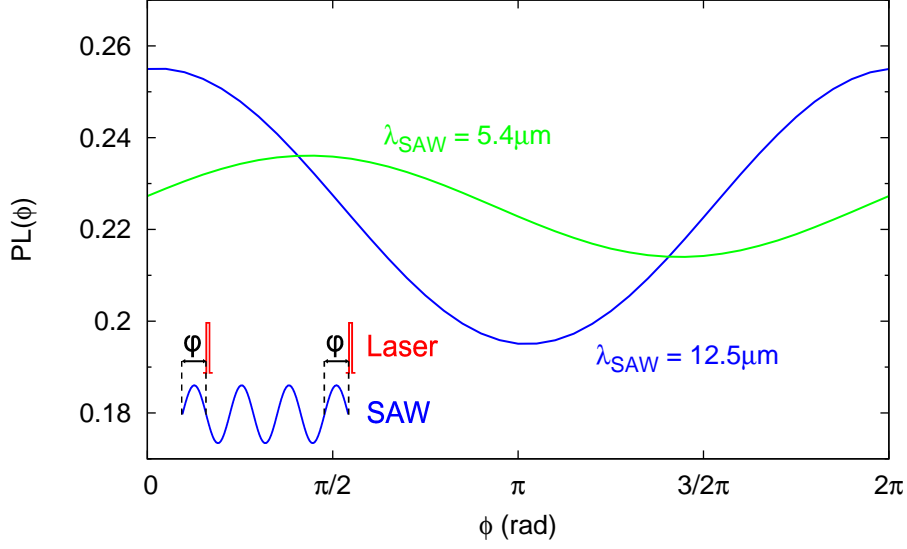
Figure 4.14: Simulated PL modulation. Used parameters: $\sigma = 2.5$ µm, $\tau = 8.0$ ns, $\alpha = 1.55$

the simulated PL for the two SAW frequencies and for the long recombination time is plotted as a function of the relative phase between laser and SAW. The measured recombination time $\tau = 1.242$ ns has been determined without SAW applied. Basically, a SAW separates electrons and holes spatially. This lowers the recombination probability and increases the average recombination time τ. Therefore, the assumption of an extended recombination time is reasonable. More precise modelling and calculations, however, are still to be done.

4.1.6 Temporal monitoring of QP luminescence

In order to resolve the temporal behaviour of the QP luminescence, the *phase locked mode* is also applied to the PL of an individual QP. Again, a SAW power scan is performed in order to determine a suitable SAW power, as shown in the upper panel of figure 4.15. Here, the luminescence energy is higher ($E \approx 1336$ meV) than the emission energies of single QPs shown before ($E \approx 1300$ meV). The higher transition energy suggests a different composition or shape of the nanostructure compared to the posts studied before, e.g. a more dot-like shape. The PL of the present structure shows the characteristic switching behaviour with a threshold SAW power of $P_{\text{SAW}} = +3$ dBm. For the phase locked measurements, a SAW power higher than the threshold power is chosen ($P_{\text{SAW}} = +8$ dBm).

In the center panel of figure 4.15, two examples with distinct relative phases ϕ_0 and $\phi_0 + \pi$ are given. For a quantitative analysis, the PL intensities of four transitions, namely the $1X^0$, $1X^-$ excitons and the two peaks $2X_{\text{l}}$ and $2X_{\text{h}}$ belonging to the biexciton are evaluated. The intensities are determined by integrating the PL over the corresponding spectral regions as indicated by the
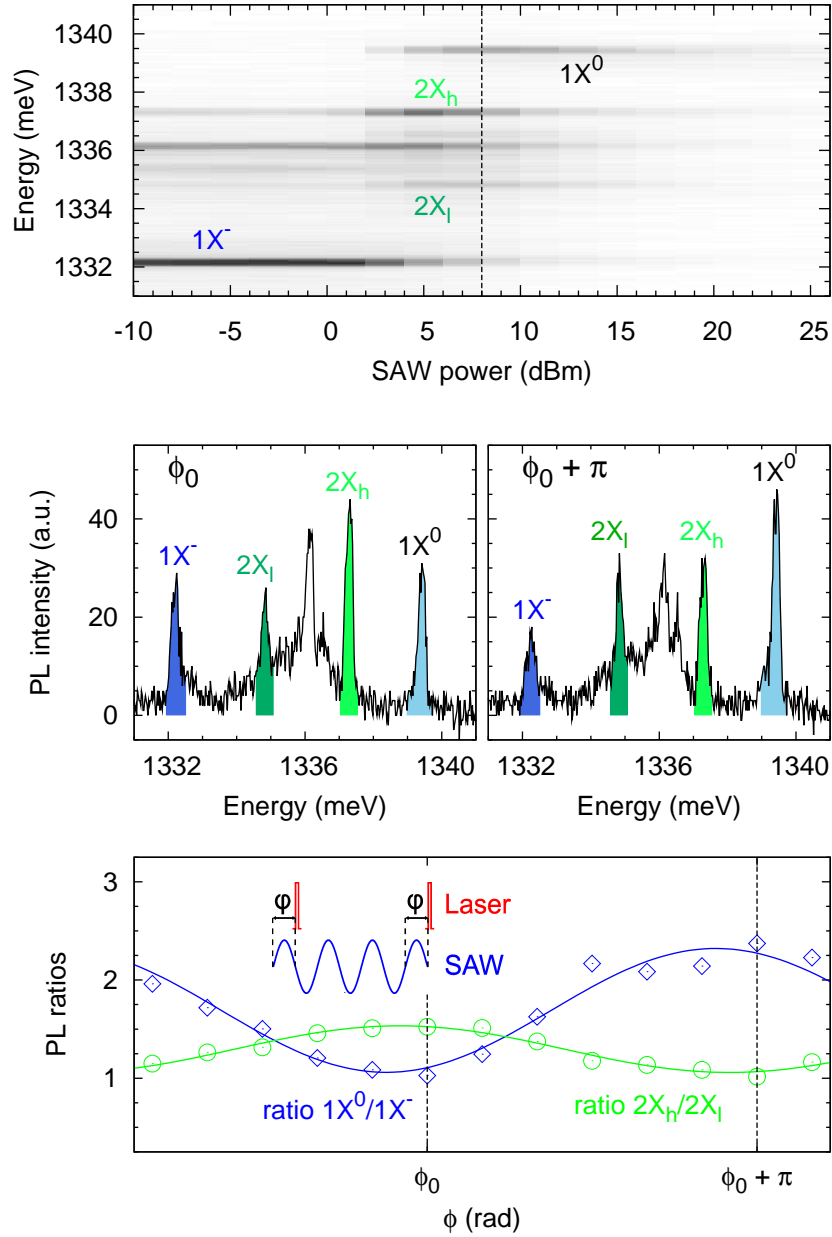
Figure 4.15: Upper panel: SAW power scan of a single QP, not phase locked. The neutral exciton (black), the negatively charged exciton (blue) and two biexciton transitions (dark green: *low* energy peak, light green: *high* energy peak) are labeled. The vertical dotted line at $P_{\mathrm{SAW}} = +8$ dBm indicates the SAW power used in the subsequent PL measurements. Center panels: two QP spectra measured with different relative phases between the SAW and the laser trigger (phase locking). Lower panel: intensity ratios of blue ($1X^0/1X^-$) and green ($2X_{\mathrm{h}}/2X_{\mathrm{l}}$) shaded PL peaks. Solid curves are sinusoidal fits. $f_{\mathrm{SAW}} = 192.9$ MHz, $P_{\mathrm{L}} = 100$ nW.
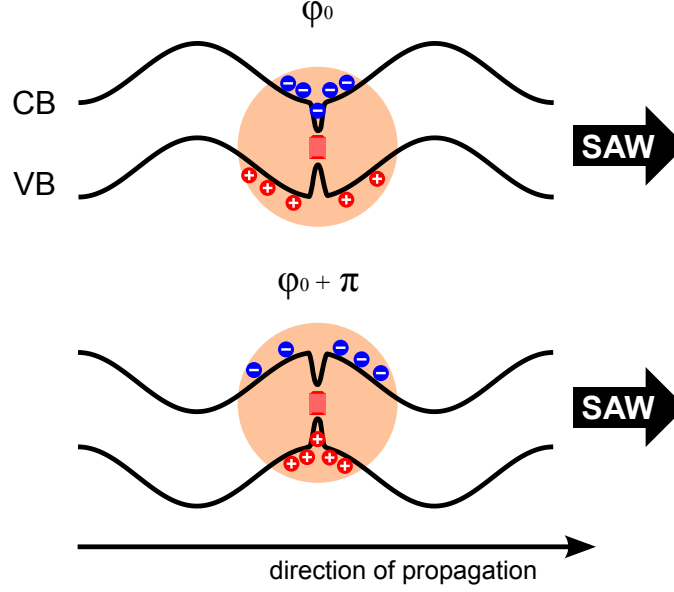
Figure 4.16: Type II band modulation of conduction and valence band caused by the *lateral* field component of the SAW propagating to the right. Two relative phases between laser and SAW are shown. For a given phase, the laser pulse excites the sample only for the sketched configuration, during the remaining time the laser is turned off. The occupation of the QP with electrons and holes depends on the relative phase giving rise to distinct emission probabilities for the neutral exciton/biexciton and negatively charged exciton. The asymmetric modulation of conduction and valence band is neglected in this sketch.

shaded areas. Then, the evaluated intensities are compared dividing the $1X^0$ intensity by the intensity of the negatively charged exciton $1X^-$ and plotting the ratios as a function of the relative phase. Accordingly, ratios of the high $(2X_h)$ and low $(2X_l)$ energy biexciton transition are calculated and plotted in the lower panel of figure 4.15. The measured intensity ratios follow sine functions which are fitted to the data points.

The oscillatory behaviour of both peak ratios supports that the SAW induces a band modulation which subsequently manipulates the PL peaks. The periods of the fitted sinusoidal curves correspond exactly to one phase cycle. Qualitatively, the oscillations can be understood by taking into account the phase dependent band modulation of the matrix and QP potential. At the position of the QP, the conduction and valence bands are locally altered resulting in potential dips as shown in the schematic 4.16. The location of these dips is directly related to the QP and therefore, these dips are fixed in space. However, the SAW also modulates the band edges of the surrounding matrix-QW, and this modulation is not fixed in space but propagates with the SAW. Hence, the piezoelectric field oscillates with frequency f_{SAW} around the QP position. The SAW period used here is $\lambda_{SAW} = 15$ µm and the diameter of the exciting laser spot is $D_L \approx 5$ µm. Since for the relatively long SAW period, the laser illuminates only a segment of an entire SAW cycle, the relative phase between SAW and laser

strongly influences the PL emission. Figure 4.16 shows two examples of band potentials with opposite phases. It illustrates particular snapshots when the laser is turned on. The laser pulse width is $\Delta t_{\mathrm{L}} \approx 50$ ps which is significantly shorter than the SAW period ($T_{\mathrm{SAW}} = 5.2$ ns, $f_{\mathrm{SAW}} = 192.9$ MHz). Carrier relaxation processes take place on timescales of several picoseconds. Thus, the SAW is a quasi-static perturbation for these processes.

In upper part of figure 4.16, the bands are bend such that the QP is preferably occupied by electrons (blue), whereas the holes (red) are displaced. The lower schematic illustrates the opposite situation. Here, the QP is filled preferably with holes. Both configurations are extreme cases, for other relative phases the occupation with electrons and holes is rather balanced.

Apart from the relative phase between the laser and the SAW, the probability of capturing an electron or hole is also determined by the potential of the QP itself. The particular compositions and shapes of the posts are statistically distributed. That explains distinct capture probabilities for the two carrier species. For example, the formation of negatively charged excitons is preferred for the QP shown in figure 1.9, whereas for a different post (figure 1.10) neutral exciton transitions are preferred. The SAW power scan in figure 4.15 reveals an enhanced probability of capturing electrons which is reflected by a dominant $1X^-$ peak at the lowest SAW power.

If the phase difference between the laser and the SAW corresponds to the configuration depicted in the upper sketch of figure 4.16, then, more electrons than holes are injected into the QP which explains that the $1X^-$ transition is stronger for this particular phase ϕ than for the opposite phase. For the phase $\phi + \pi$, the injection of holes is preferred. Taking into account a generally enhanced probability of capturing electrons for the particular QP, then, an enhanced formation of neutral excitons is expected and coevally, the emission of the $1X^-$ exciton is reduced. That would explain the different $1X^0/1X^-$ ratios for the two relative phases ϕ_0 and $\phi_0 + \pi$.

The origin of the different biexciton peaks $2X_{\mathrm{l}}$ and $2X_{\mathrm{h}}$ is still under investigation. The oscillating behaviour of their ratio supports that, similar to the single exciton, differently charged biexciton complexes account for the different peaks. Depending on the phase configurations, either PL emission from negatively or positively/neutral charged excitons is preferred.
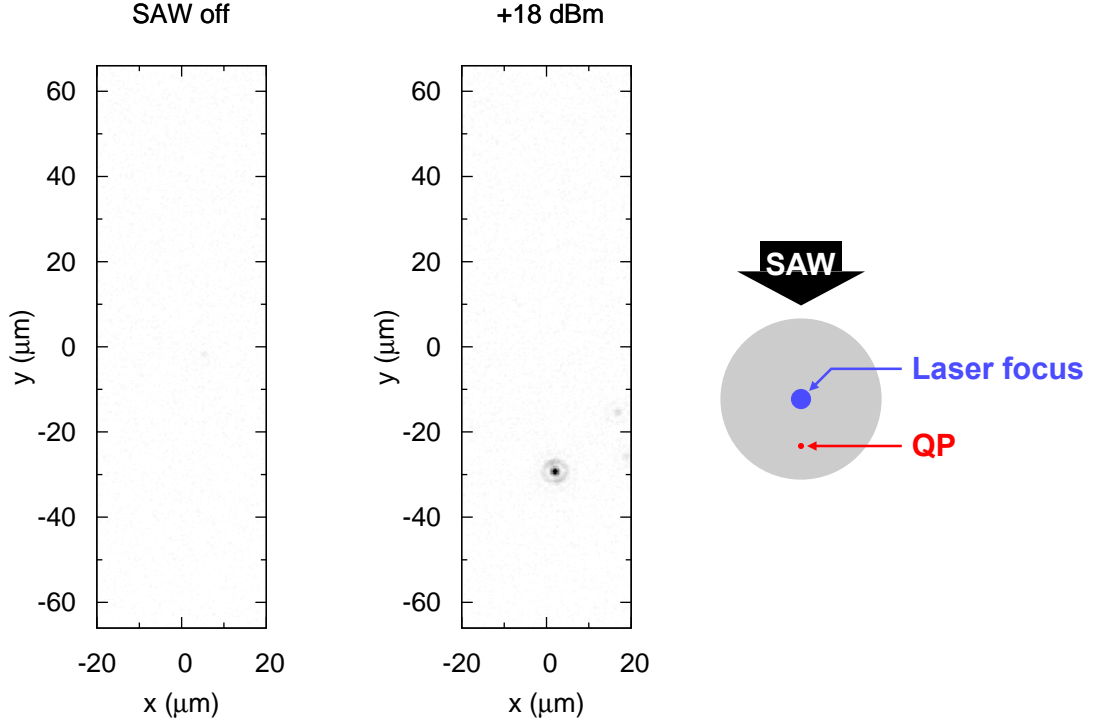
Figure 4.17: The position of the QP lies $\Delta d = 30$ µm below the Laser focus. Consequently, no PL is detected without SAW. For a SAW power of $P_{\mathrm{SAW}} = +18$ dBm, a pronounced emission of the QP is detected explained by SAW driven carrier injection. $f_{\mathrm{SAW}} = 192.9$ MHz, $P_{\mathrm{L}} = 72$ nW.

4.2   Remote carrier injection into individual QPs

The QPs are coupled to a matrix which forms a 2-dimensional layer. The piezoelectric field modulation of a SAW dissociates excitons and transports the carriers within this layer. Therefore, the matrix PL measured directly at the laser focus is quenched, as shown before. However, charge carriers trapped in the dynamically modulated band potentials are transported with sound velocity in direction of the SAW propagation. Each carrier species is separated from the other at intervals of $\lambda_{\mathrm{SAW}}/2$. The propagation of the SAW causes a *bipolar charge transport*, as already explained in section 2.3. If the band gap is locally lowered, for example by a QD lying in the sound path of the SAW, the charge carriers can be captured by such inhomogeneities. This allows for carrier injection into remote nanostructures by SAWs.

In figure 4.17, two spatially resolved PL images are shown (see also section 3.2). Additionally, a longpass filter is used, in order to block light emitted by the matrix-QW. The laser illuminates a spot of diameter $D_{\mathrm{L}} \approx 5$ µm in the center

of the aperture ($x = y = 0$ µm). Since there is no QP present, no luminescence is detected without SAW (left image). When a SAW is applied, a QP located $\Delta d = 30$ µm below the laser focus emits PL light supporting the underlying mechanism of *bipolar charge transport* (right image). In figure 4.17, the SAW propagates downwards as indicated by the arrow.

The images have been recorded by reading out the entire CCD chip and positioning the spectrometer grating to the 0th order of diffraction. Hence, no spectral information is obtained and the spectrometer is used like a conventional camera. If the grating is positioned to the first order of diffraction, a modified imaging mode can be realized achieving a combination of spatial and spectral resolution (see section 3.2). This configuration is depicted schematically in upper inset of figure 4.18.

In figure 4.18, the same injection experiment as in figure 4.17 is performed, but the grating is positioned to the first order of diffraction. The two distinct spectral regions for the matrix-QW and QP emissions are color coded. In the upper panels emission from the matrix is displayed in blue, whereas QP emission is displayed in red in the lower panels. At the position of the laser focus ($\Delta d = 0$ µm in vertical direction), direct PL from the matrix-QW around $E = 1417$ meV is measured. The PL signal of the matrix has full intensity when no SAW is applied as shown in the left part of figure 4.18. When the SAW is applied, the matrix-QW peak is quenched.

At a distance of $\Delta d = 12$ µm below the laser focus, there is a single QP. The SAW coming from the upper part transports charge carriers excited at the position of the laser and injects them into the single post. The QP then shows PL emission which is absent when no SAW is applied. In contrast to the experiment shown above, additional information about the spectral lines is provided.

Figures 4.17 and 4.18 show spatially resolved luminescence and demonstrate that the emitted PL light comes from a remote QP, i.e. the QP is not directly excited by the laser and the luminescence is only present when a SAW is applied. Once the remotely injected post has been resolved spatially, more information can obtained by measuring PL spectra as a function of applied SAW power which is shown in figure 4.19. As indicated by the insets, two experimental configurations are used. In the lower panel, the QP and the laser focus are aligned, i.e. the QP is measured under direct excitation. For direct excitation, the typical switching behaviour of PL lines is observed (see also section 4.1.2). At a SAW power of $P_{\mathrm{SAW}} \approx +2$ dBm, the $1X^-$ exciton line vanishes and simultaneously, the transition of the neutral exciton $1X^0$ arises. The biexciton $2X^0$ also shows a SAW power dependency.

In the upper panel of figure 4.19, the same QP is shifted outside the laser focus. The distance between laser focus and post is $\Delta d \approx 20$ µm. For low SAW power, no luminescence is detected. Beginning from $P_{\mathrm{SAW}} \approx +2$ dBm, peaks originating from the neutral exciton and the biexciton are observed. The absence of
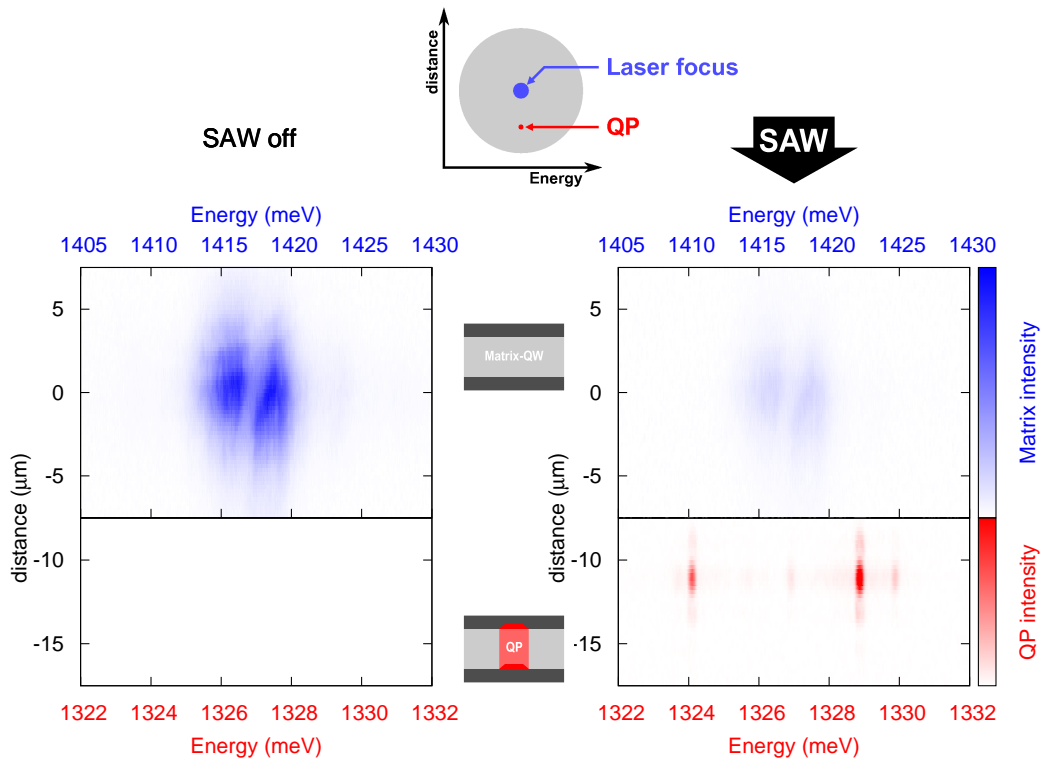
Figure 4.18: Spatially and spectrally resolved luminescence pattern ($P_{\mathrm{L}} = 300$ nW). PL from the matrix (blue, upper panels) and the QP (red, lower panels) are color coded. When no SAW is applied, only the matrix shows emission (left panels). With SAW ($f_{\mathrm{SAW}} = 193$ MHz, $P_{\mathrm{SAW}} = +8$ dBm), this emission is quenched and charge carriers are transported to a single QP at $\Delta d = 12$ µm below the laser focus (right panels). The inset at the top of the figure illustrates the combination of spatial and spectral resolution.

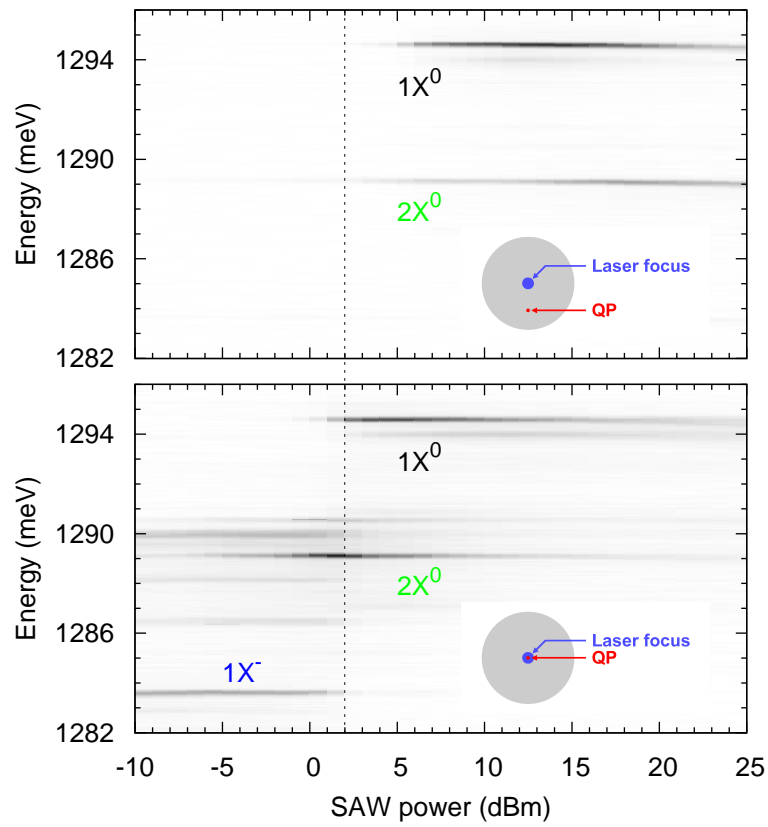Figure 4.19: Upper panel: SAW power scan of a remote QP. The distance between laser focus and QP is $\Delta d \approx 20$ µm. According to the inset, the SAW propagates from the top to the bottom and injects carrier into the QP lying below the laser focus. Lower panel: SAW power scan of the same QP under direct laser excitation. $f_{SAW} = 193$ MHz.

luminescence at low SAW power is in agreement with the measurements shown before. The remote QP emits luminescence light only if charge carriers are injected into it by SAWs. Remarkably, the spectral lines appearing for higher SAW power match to those of direct laser excitation. Clearly, the same neutral exciton line(s) $1X^0$ and biexciton line $2X^0$ are observed, indicating that the same PL switching mechanism applies for both experimental configurations. Since for the remotely pumped QP, the emission of PL light is a consequence of charge carriers which have been transported and injected from the QW, obviously, carrier capture from the QW plays an important role for the directly excited QP, too. Considering the cross-sectional area of the illuminated sample surface and that of the QP, it seems plausible that most of the charges occupying the QP are captured from the surrounding material. Only a marginal fraction is excited directly in the QP itself, otherwise the PL intensities would not be comparable for the two configurations. The crucial role of the carrier transport within the QW is underlined by the fact that the SAW power required for PL switching and remote pumping coincidences with the slope of the QW quenching curve (compare for example upper panel in figure 4.4).

In conclusion, the injection of charge carriers into individual QPs is demonstrated in an experimental configuration where the position of the post is outside of the laser focus and the SAW propagates in direction from the focus to the position of the post. The principle of *remote carrier injection* is verified by spatially resolved recordings taken in *image mode*. Detailed information is provided by SAW power scans of the two experimental configurations (direct excitation and remote carrier injection). Both scans are almost identical for power levels above a critical SAW power where PL switching and carrier injection sets in confirming the mechanism of charge conveyance and carrier capture from the QW into the QP.

4.3   Spatial monitoring of PL modulation

The piezoelectric field of a SAW dissociates excitons within a QW structure giving rise to the observed PL quenching. Since the field strength oscillates temporally and spatially, the PL emission of the matrix and the QPs is modulated. The temporal part of PL modulation has already been shown for the directly excited QW and individual QPs in sections 4.1.5 and 4.1.6. In the following, spatially resolved images of the SAW induced modulation are presented.

Figure 4.20 shows a series of PL images measured with the spectrometer CCD under 0th order of diffraction (see section 3.2). A longpass filter at the spectrometer entrance ensures that the laser line is blocked, but emission from the matrix-QW and from QPs can be detected. The pulsed laser and the SAW are both operated without duty cycle, but are synchronized using the afore described phase locking method (see section 3.4). Additionally, the laser beam is expanded to a diameter of $D_{\mathrm{L}} \approx 15$ µm on the sample. The left PL image is measured without SAW applied. Then, the SAW power P_{SAW} is successively increased. At the upper part (blue box), PL from the directly excited QW is detected, and for applied SAW, PL from remote QPs is measured at the lower part (red box). A lamellar pattern is observed for the matrix PL when the SAW is turned on. The period of this pattern corresponds to $\lambda_{\mathrm{SAW}}/2$. The overall matrix PL intensity decreases when the SAW power is increased. Vice versa, the intensity of the remotely pumped QPs increases.

The quenching behaviour of the matrix luminescence and the increasing PL intensity of the remotely pumped QPs are explained by exciton dissociation and remote carrier injection which have already been discussed. Surprisingly, the period of the observed stripes in the QW luminescence is $\lambda_{\mathrm{SAW}}/2$ which contradicts the phase locked measurements shown before. There, clearly a 2π modulation is observed. By varying the relative phase between the laser and the SAW, the QW luminescence patter turns out to be stationary to a large extent. Additionally, a smaller phase dependent PL modulation is observed which is superimposed to this stationary pattern.

A further experiment is performed without synchronization of laser and SAW and a similar stationary modulation pattern is found for the matrix PL. Since the synchronization is lifted, the luminescence pattern cannot be caused by a propagating SAW. Probably, the SAW is reflected by the second IDT or the sample edge and interferes with the SAW generated by the first IDT. Thus, a standing wave pattern is observed. This observation is supported by experiments from Kutschera et. al., where a standing wave was generated by applying a HF signal to both IDTs [46]. There, the same periodicity was observed and the bright areas of the luminescence pattern were interpreted as regions of enhanced hole confinement. Since the hole mobility is much lower than that of electrons, exciton recombination preferably occurs at locations where holes are first confined during constructive interference and then released during destructive interference. Similar observations have also been reported for
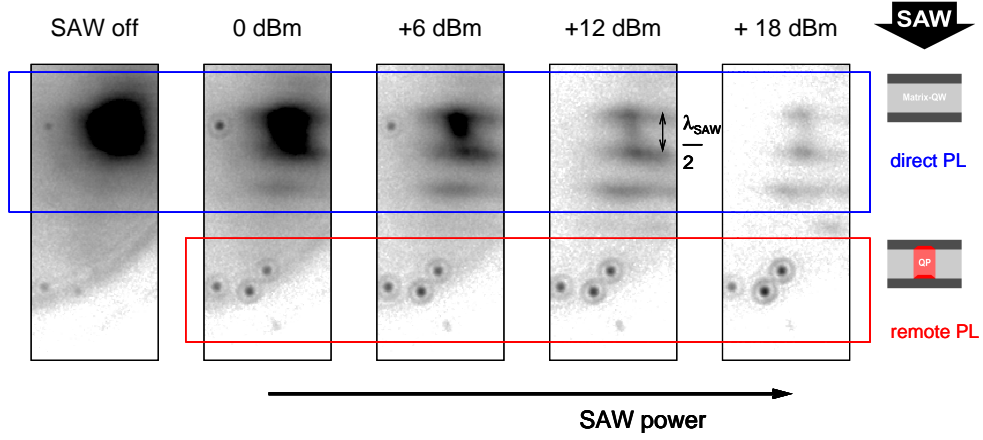
Figure 4.20: SAW power series of directly modulated matrix PL and remotely pumped QPs. The laser wavelength is blocked by a longpass filter ($\lambda_L = 661$ nm, $P_L = 85$ nW). In the upper part, direct matrix-QW luminescence is visible. When the SAW is turned on ($f_{SAW} = 192.9$ MHz), a stripe pattern with period $\lambda_{SAW}/2 = 7.5$ µm is generated, for higher SAW power, the QW luminescence is quenched. At the lower part of the images, luminescence from remote QPs is detected which is absent without SAW. The distance between the laser spot and the remotely pumped QPs is $\Delta d \approx 30$ µm. The black/white coded PL is plotted on a logarithmic scale.

voltage-controlled lateral potential superlattices [38, 39] where the influence of distinct carrier mobilities was shown in temporally and spatially resolved PL measurements.

An interesting experimental configuration can be prepared for two orthogonally propagating SAWs. For the spatially resolved PL measurement shown in the left image of figure 4.21, the signal of the HF generator has been split and applied to two orthogonally oriented IDTs. In the region of exciton generation, both SAW beams interfere giving rise to the observed QW luminescence pattern. As for the stripe pattern observed for plane acoustic waves, the pattern generated by orthogonally interfered SAWs is stationary to a large extent and superimposed by a smaller phase dependent PL modulation. The stationary part of the pattern is probably due to standing acoustic waves caused by reflections at the opposite IDTs or at the sample edges. The potential modulation of two orthogonally interfered SAWs gives rise to a 3-dimensional confinement for charges excited in a QW. This results from the combination of vertical confinement caused by the QW and the lateral piezoelectric band modulation caused by the SAWs. The right picture in figure 4.21 illustrates the resulting potential forming a dot-like pattern. Since the potential minima for electrons and holes move in lateral (diagonal) direction, these minima are called dynamic potential dots [3, 74]. Several applications have been reported for the dynamic dots, e.g. spin transport [75] and quantization effects which are expected for intense SAWs with short period λ_{SAW} [25].
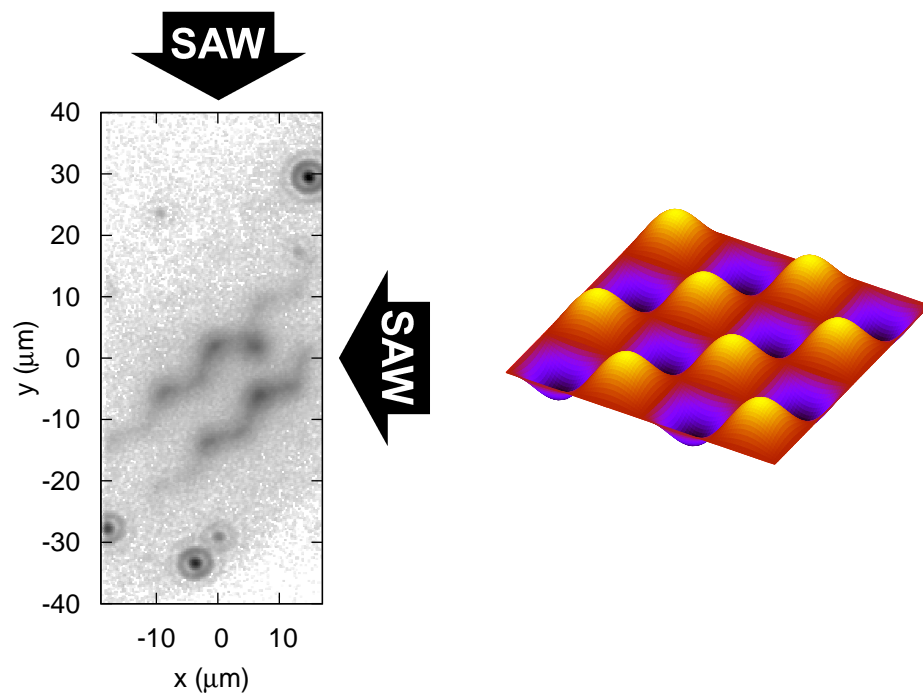
Figure 4.21: Left: Spatially resolved image of matrix and QP luminescence ($P_L =$ 85 nW). The pattern in the center of the image is caused by the interference of two orthogonally travelling SAWs. $f_{SAW} = 192.9$ MHz and $P_{SAW} = +17$ dBm for each IDT. The black/white coded PL intensities are plotted on a logarithmic scale. Right: Illustration of dynamic potential dots.

Chapter 5

Conclusion and Outlook

The main focus of this work was the investigation of carrier capture and optical emission properties of semiconductor nanostructures and in particular of self-assembled QPs and their manipulation using SAWs. An important result of this work is the demonstration of PL switching for single QPs. The switching occurs around a very narrow power range at a critical SAW power and coincides with a simultaneous decrease of the matrix-QW luminescence. This switching behaviour is only present if SAWs are applied. By varying other experimental parameters, e.g. the laser intensity, no similar effect is observed. Furthermore, some nanostructures of the QP sample show a PL splitting behaviour. Since the PL energies of these structures are higher than for QPs showing no PL splitting, a dot-like character of these structures is assumed. Finally, the QP system is compared with self-assembled embedded QDs performing SAW power series. For the conventional self-assembled QDs, a hysteretic PL behaviour is observed when the SAW power is increased and subsequently decreased, whereas the QP luminescence is non-hysteretic.

These results point out that the matrix-QW and the WL play a fundamental role for the observed findings. Carriers, which have been excited within these layers, are separated into stripes of electrons and holes due to a charge conveyance effect [63], and are then acoustically conveyed and eventually trapped in the 0-dimensional levels of QDs and QPs. Thus, electrons and holes are captured sequentially which explains the switching of PL lines when compared to PL spectra without SAWs. Both systems, QPs and QDs, are coupled to a 2-dimensional layer enabling SAW assisted charge conveyance. In contrast to the matrix-QW, the WL is much thinner giving rise to reduced carrier mobilities within the WL and additional binding to random local potential fluctuations, e.g. at the interfaces of the WL.

By synchronizing the pulsed laser excitation and the SAW, temporal resolution is achieved. For the matrix and the QP, a $\Delta\phi = 2\pi$ modulation is observed in the PL intensity which is not in accordance with a comparable confinement and conveyance of electrons and holes. However, since the carrier species have different effective masses and mobilities, charge conveyance is not symmetric
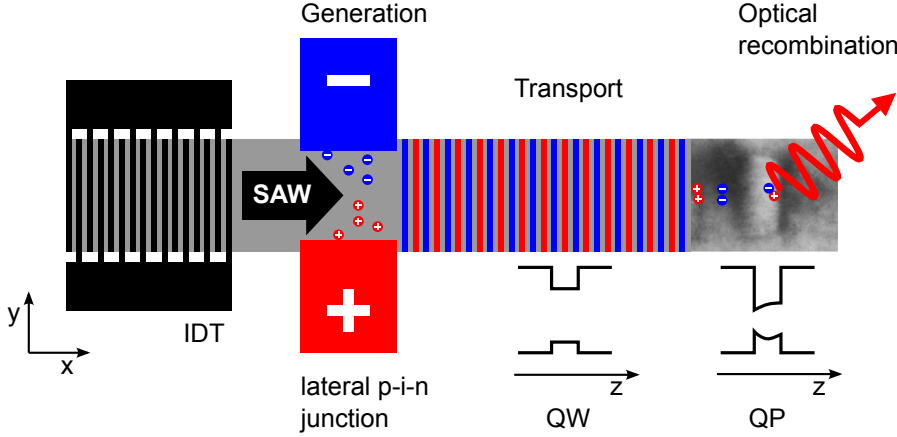
Figure 5.1: Electric-SAW-triggered SPS

which is consistent with the observed period of 2π. If the SAW is excited in cw mode, spatially resolved images of the matrix luminescence reveal a stripe pattern with a period corresponding to half of the SAW wavelength. That effect can mainly be explained by the formation of standing SAW waves due to reflections at a second IDT or the sample edge.

Finally, remote carrier injection into individual QPs is demonstrated for the first time using SAWs. Spatially resolved PL detection shows luminescence from remote nanostructures only if a SAW is applied. The observed PL lines of a remotely pumped QP correspond to those lines of a directly excited QP for a SAW power higher than the critical switching power which is another evidence for the underlying mechanism of acoustic charge conveyance. As the charges are acoustically injected into the QP by the SAW, SAW assisted carrier capture and light emission is rather deterministic in contrast to a direct excitation.

In order to use the SAW induced carrier injection for the realization of a SPS, further steps have to be taken. In particular, photon-correlation measurements have to be performed to prove the properties as a non-classical light source. In such experiments, so-called photon antibunching is expected for a quantum light emitter. Moreover, polarization entanglement between photons could be realized by using the biexciton decay cascade $2X \rightarrow 1X$. This method was proposed by Benson et. al. [8] and experimentally realized by several groups [1,27,54,73].

For any practical implementation, *deterministic* generation of the initial $2X$ state of the cascade has to be ensured. This requisition is in particular challenging using a Coulomb blockade in an LED-type structure, as proposed originally by Benson et. al. and has not been realized until now. The results of this work clearly indicate that the inherently sequential injection of electron and holes by a SAW is a promising approach towards this goal since spurious charge exciton generation can be strongly suppressed.

For future realizations of a SAW-triggered SPS and sources of entangled photons, carriers could be generated electrically instead of using a laser, as depicted schematically in figure 5.1. In the sketched configuration, a lateral p-i-n junction injects electrons and holes into the sound path of an IDT. The SAW separates and acoustically conveys the two carrier species within the QW. Then, the carriers are sequentially injected into a QP giving rise to a periodic emission of single photons.

Bibliography

[1] N. Akopian, N. H. Lindner, E. Poem, Y. Berlatzky, J. Avron, D. Gershoni, B. D. Gerardot, and P. M. Petroff. Entangled photon pairs from semiconductor quantum dots. *Phys. Rev. Lett.*, 96(13):130501, Apr 2006.

[2] F. Alsina, P. V. Santos, R. Hey, A. García-Cristóbal, and A. Cantarero. Dynamic carrier distribution in quantum wells modulated by surface acoustic waves. *Phys. Rev. B*, 64(4):041304, Jun 2001.

[3] F. Alsina, J. A. H. Stotz, R. Hey, and P. V. Santos. Acoustically induced potential dots in GaAs quantum wells. *Solid State Communications*, 129(7):453 – 457, 2004.

[4] A. Babinski, J. Borysiuk, S. Kret, M. Czyz, A. Golnik, S. Raymond, and Z. R. Wasilewski. Natural quantum dots in the InAs/GaAs wetting layer. *Applied Physics Letters*, 92(17):171104, 2008.

[5] J. Bardeen and W. Shockley. Deformation potentials and mobilities in non-polar crystals. *Phys. Rev.*, 80(1):72–80, Oct 1950.

[6] M. Bayer, O. Stern, P. Hawrylak, S. Fafard, and A. Forchel. Hidden symmetries in the energy levels of excitonic artificial atoms. *Nature*, 405:923–926, 2000.

[7] C. Bennett and G. Brassard. Public key distribution and coin tossing. *Proceedings of the IEEE International Conference on Computers, Systems and Signal Processing*, page 175, 1984.

[8] O. Benson, C. Santori, M. Pelton, and Y. Yamamoto. Regulated and entangled photons from a single quantum dot. *Phys. Rev. Lett.*, 84(11):2513–2516, Mar 2000.

[9] G. Bir and G. Pikus. *Symmetry and Strain Induced Effects in Semiconductors.* J. Wiley, New York, 1974.

[10] M. Bödefeld. *Opto-akustisches Pumpen von Halbleiter-Quantenpunkten, Dissertation.* Ludwig-Maximilians-Universität München, 2003.

[11] D. Bouwmeester, J.-W. Pan, K. Mattle, M. Eibl, H. Weinfurter, and A. Zeilinger. Experimental quantum teleportation. *Nature*, 390:575 – 579, 1997.

[12] K. Brunner, G. Abstreiter, G. Böhm, G. Tränkle, and G. Weimann. Sharp-line photoluminescence and two-photon absorption of zero-dimensional biexcitons in a GaAs/AlGaAs structure. *Physical Review Letters*, 73(8):1138–1141, 1994.

[13] M. Califano and P. Harrison. Approximate methods for the solution of quantum wires and dots: Connection rules between pyramidal, cuboidal, and cubic dots. *Journal of Applied Physics*, 86(9):5054–5059, 1999.

[14] M. Califano and P. Harrison. Composition, volume, and aspect ratio dependence of the strain distribution, band lineups and electron effective masses in self-assembled pyramidal $In_{1-x}Ga_xAs$/GaAs and Si_xGe_{1-x}/Si quantum dots. *Journal of Applied Physics*, 91(1):389–398, 2002.

[15] O. D. D. Couto, S. Lazic, F. Iikawa, J. A. H. Stotz, U. Jahn, R. Hey, and P. V. Santos. Photon anti-bunching in acoustically pumped quantum dots. *Nat Photon*, 3(11):645–648, 2009.

[16] M. A. Cusack, P. R. Briddon, and M. Jaros. Electronic structure of InAs/GaAs self-assembled quantum dots. *Phys. Rev. B*, 54(4):R2300–R2303, Jul 1996.

[17] T. C. Damen, J. Shah, D. Y. Oberli, D. S. Chemla, J. E. Cunningham, and J. M. Kuo. Dynamics of exciton formation and relaxation in GaAs quantum wells. *Phys. Rev. B*, 42(12):7434–7438, Oct 1990.

[18] S. Datta. *Surface acoustic wave devices.* Prentice-Hall, New Jersey, 1986.

[19] J. Davies. *The physics of low-dimensional semiconductors.* Cambridge University Press, 1998.

[20] A. Einstein. Über einen die Erzeugung und Verwandlung des Lichtes betreffenden heuristischen Gesichtspunkt. *Annalen der Physik*, 322(6):132 – 148, 1905.

[21] J. Feldmann, G. Peter, E. O. Göbel, P. Dawson, K. Moore, C. Foxon, and R. J. Elliott. Linewidth dependence of radiative exciton lifetimes in quantum wells. *Phys. Rev. Lett.*, 59(20):2337–2340, Nov 1987.

[22] F. Findeis. *Optical Spectroscopy on Single Self-assembled Quantum Dots, Dissertation.* Walter Schottky Institut, Technische Universität München, 2001.

[23] F. Findeis, M. Baier, A. Zrenner, M. Bichler, G. Abstreiter, U. Hohenester, and E. Molinari. Optical excitations of a self-assembled artificial ion. *Phys. Rev. B*, 63(12):121309, Mar 2001.

[24] J. R. Gell, M. B. Ward, R. J. Young, R. M. Stevenson, P. Atkinson, D. Anderson, G. A. C. Jones, D. A. Ritchie, and A. J. Shields. Modulation of single quantum dot energy levels by a surface-acoustic-wave. *Applied Physics Letters*, 93(8):081115, 2008.

[25] A. O. Govorov, A. V. Kalameitsev, V. M. Kovalev, H.-J. Kutschera, and A. Wixforth. Self-induced acoustic transparency in semiconductor quantum films. *Phys. Rev. Lett.*, 87(22):226803, Nov 2001.

[26] M. Grundmann, O. Stier, and D. Bimberg. InAs/GaAs pyramidal quantum dots: Strain distribution, optical phonons, and electronic structure. *Phys. Rev. B*, 52(16):11969–11981, Oct 1995.

[27] R. Hafenbrak, S. M. Ulrich, P. Michler, L. Wang, A. Rastelli, and O. G. Schmidt. Triggered polarization-entangled photon pairs from a single quantum dot up to 30 K. *New Journal of Physics*, 9(9):315, 2007.

[28] P. Harrison. *Quantum wells, wires and dots: theoretical and computational physics.* Wiley, New York, NY, 2000.

[29] P. Hawrylak. Excitonic artificial atoms: Engineering optical properties of quantum dots. *Phys. Rev. B*, 60(8):5597–5608, Aug 1999.

[30] J. He, H. J. Krenner, C. Pryor, J. P. Zhang, Y. Wu, D. G. Allen, C. M. Morris, M. S. Sherwin, and P. M. Petroff. Growth, structural and optical properties of self-assembled (In, Ga)As quantum posts on GaAs. *Nano Letters*, 7(3):802–806, 2007.

[31] J. He, R. Notzel, P. Offermans, P. M. Koenraad, Q. Gong, G. J. Hamhuis, T. J. Eijkemans, and J. H. Wolter. Formation of columnar (In,Ga)As quantum dots on GaAs(100). *Applied Physics Letters*, 85(14):2771–2773, 2004.

[32] P. B. Joyce, T. J. Krzyzewski, G. R. Bell, T. S. Jones, S. Malik, D. Childs, and R. Murray. Effect of growth rate on the size, composition, and optical properties of InAs/GaAs quantum dots grown by molecular-beam epitaxy. *Phys. Rev. B*, 62(16):10891–10895, Oct 2000.

[33] P. B. Joyce, T. J. Krzyzewski, G. R. Bell, B. A. Joyce, and T. S. Jones. Composition of InAs quantum dots on GaAs(001): Direct evidence for (In,Ga)As alloying. *Phys. Rev. B*, 58(24):R15981–R15984, Dec 1998.

[34] I. Kegel, T. H. Metzger, A. Lorke, J. Peisl, J. Stangl, G. Bauer, J. M. García, and P. M. Petroff. Nanometer-scale resolution of strain and interdiffusion in self-assembled InAs/GaAs quantum dots. *Phys. Rev. Lett.*, 85(8):1694–1697, Aug 2000.

[35] H. J. Kimble, M. Dagenais, and L. Mandel. Photon antibunching in resonance fluorescence. *Phys. Rev. Lett.*, 39(11):691–695, Sep 1977.

[36] T. Kita, N. Tamura, O. Wada, M. Sugawara, Y. Nakata, H. Ebe, and Y. Arakawa. Artificial control of optical gain polarization by stacking quantum dot layers. *Applied Physics Letters*, 88(21):211106, 2006.

[37] E. Knill, R. Laflamme, and G. J. Milburn. A scheme for efficient quantum computation with linear optics. *Nature*, 409:46–52, 2001.

[38] J. Krauß. *Photonische Speicherzellen in lateralen Potentialübergittern, Dissertation.* Ludwig-Maximilians-Universität München, 2003.

[39] J. Krauß, A. Wixforth, A. V. Kalameitsev, A. O. Govorov, W. Wegscheider, and J. P. Kotthaus. Nonlinear charge spreading visualized in voltage-controlled lateral superlattices. *Phys. Rev. Lett.*, 88(3):036803, Jan 2002.

[40] H. J. Krenner, C. Pryor, J. He, and P. M. Petroff. A semiconductor exciton memory cell based on a single quantum nanostructure. *Nano Letters*, 8:1750 – 1755, 2008.

[41] H. J. Krenner, C. Pryor, J. He, J. P. Zhang, Y. Wu, C. M. Morris, M. S. Sherwin, and P. M. Petroff. Growth and optical properties of self-assembled InGaAs quantum posts. *Physica E: Low-dimensional Systems and Nanostructures*, 40(6):1785 – 1789, 2008. 13th International Conference on Modulated Semiconductor Structures.

[42] H. J. Krenner, S. Stufler, M. Sabathil, E. C. Clark, P. Ester, M. Bichler, G. Abstreiter, J. J. Finley, and A. Zrenner. Recent advances in exciton-based quantum information processing in quantum dot nanostructures. *New Journal of Physics*, 7:184, 2005.

[43] C. Kurtsiefer, S. Mayer, P. Zarda, and H. Weinfurter. Stable solid-state source of single photons. *Phys. Rev. Lett.*, 85(2):290–293, Jul 2000.

[44] J. Kusano, Y. Segawa, Y. Aoyagi, S. Namba, and H. Okamoto. Extremely slow energy relaxation of a two-dimensional exciton in a GaAs superlattice structure. *Phys. Rev. B*, 40(3):1685–1691, Jul 1989.

[45] A. Kuther, M. Bayer, A. Forchel, A. Gorbunov, V. B. Timofeev, F. Schäfer, and J. P. Reithmaier. Zeeman splitting of excitons and biexcitons in single $In_{0.60}Ga_{0.40}As$/GaAs self-assembled quantum dots. *Phys. Rev. B*, 58(12):R7508–R7511, Sep 1998.

[46] H.-J. Kutschera. *Lineare und nichtlineare akustophotoelektrische Wechselwirkung, Dissertation.* Ludwig-Maximilians-Universität München, 2003.

[47] P. G. Kwiat, K. Mattle, H. Weinfurter, A. Zeilinger, A. V. Sergienko, and Y. Shih. New high-intensity source of polarization-entangled photon pairs. *Phys. Rev. Lett.*, 75(24):4337–4341, Dec 1995.

[48] D. Leonard, K. Pond, and P. M. Petroff. Critical layer thickness for self-assembled InAs islands on GaAs. *Physical Review B*, 50(16):11687–11692, 1994.

[49] L. H. Li, P. Ridha, G. Patriarche, N. Chauvin, and A. Fiore. Shape-engineered epitaxial InGaAs quantum rods for laser applications. *Applied Physics Letters*, 92(12):121102, 2008.

[50] H. Lipsanen, M. Sopanen, and J. Ahopelto. Luminescence from excited states in strain-induced $In_xGa_{1-x}As$ quantum dots. *Phys. Rev. B*, 51(19):13868–13871, May 1995.

[51] N. Liu, J. Tersoff, O. Baklenov, J. A. L. Holmes, and C. K. Shih. Nonuniform composition profile in $In_{0.5}Ga_{0.5}As$ alloy quantum dots. *Physical Review Letters*, 84(2):334–337, 2000.

[52] P. Michler, A. Kiraz, C. Becher, W. V. Schoenfeld, P. M. Petroff, L. Zhang, E. Hu, and A. Imamoglu. A quantum dot single-photon turnstile device. *Science*, 290(5500):2282–2285, 2000.

[53] D. A. B. Miller, D. S. Chemla, T. C. Damen, A. C. Gossard, W. Wiegmann, T. H. Wood, and C. A. Burrus. Band-edge electroabsorption in quantum well structures: The quantum-confined stark effect. *Phys. Rev. Lett.*, 53(22):2173–2176, Nov 1984.

[54] A. Mohan, M. Felici, P. Gallo, B. Dwir, A. Rudra, J. Faist, and E. Kapon. Polarization-entangled photons produced with high-symmetry site-controlled quantum dots. *Nat Photon*, 4(5):302–306, 2010.

[55] D. Morgan. *Surface-Wave Devices for Signal Processing*. Elsevier Science Publishers B.V., Amsterdam, 1991.

[56] D. J. Mowbray and M. S. Skolnick. New physics and devices based on self-assembled semiconductor quantum dots. *Journal of Physics D Applied Physics*, 38(13):2059–2076, 2005.

[57] T. Nakaoka, T. Kakitsuka, T. Saito, and Y. Arakawa. Manipulation of electronic states in single quantum dots by micromachined air-bridge. *Applied Physics Letters*, 84(8):1392–1394, 2004.

[58] T. Nakaoka, T. Kakitsuka, T. Saito, S. Kako, S. Ishida, M. Nishioka, Y. Yoshikuni, and Y. Arakawa. Strain-induced modifications of the electronic states of InGaAs quantum dots embedded in bowed airbridge structures. *Journal of Applied Physics*, 94(10):6812–6817, 2003.

[59] A. Oliner. *Acoustic Surface Waves*. Springer Verlag, 1973.

[60] E. O'Reilly. Valence band engineering in strained-layer structures. *Semiconductor Science and Technology*, 4:121, 1989.

[61] D. V. Regelman, E. Dekel, D. Gershoni, E. Ehrenfreund, A. J. Williamson, J. Shumway, A. Zunger, W. V. Schoenfeld, and P. M. Petroff. Optical spectroscopy of single quantum dots at tunable positive, neutral, and negative charge states. *Physical Review B*, 64(16):165301, 2001.

[62] C. Rocke. *Dynamische Modulation der Lumineszenz von Quantentopfstrukturen durch akustische Oberflächenwellen, Dissertation*. Ludwig-Maximilians-Universität München, 1997.

[63] C. Rocke, S. Zimmermann, A. Wixforth, J. P. Kotthaus, G. Böhm, and G. Weimann. Acoustically driven storage of light in a quantum well. *Phys. Rev. Lett.*, 78(21):4099–4102, May 1997.

[64] P. Roussignol, C. Delalande, A. Vinattieri, L. Carraresi, and M. Colocci. Dynamics of exciton relaxation in GaAs/Al$_x$Ga$_{1-x}$As quantum wells. *Phys. Rev. B*, 45(12):6965–6968, Mar 1992.

[65] J. Rudolph, R. Hey, and P. V. Santos. Long-range exciton transport by dynamic strain fields in a GaAs quantum well. *Phys. Rev. Lett.*, 99(4):047602, Jul 2007.

[66] H. Sakaki, T. Noda, K. Hirakawa, M. Tanaka, and T. Matsusue. Interface roughness scattering in GaAs/AlAs quantum wells. *Applied Physics Letters*, 51(23):1934–1936, 1987.

[67] M. Scheibner, I. V. Ponomarev, E. A. Stinaff, M. F. Doty, A. S. Bracker, C. S. Hellberg, T. L. Reinecke, and D. Gammon. Photoluminescence spectroscopy of the molecular biexciton in vertically stacked InAs − GaAs quantum dot pairs. *Physical Review Letters*, 99(19):197402, 2007.

[68] A. Schliwa, M. Winkelnkemper, and D. Bimberg. Few-particle energies versus geometry and composition of In$_x$Ga$_{1-x}$As/GaAs self-organized quantum dots. *Phys. Rev. B*, 79(7):075443, Feb 2009.

[69] F. J. R. Schülein. *Diplomarbeit, Energie- und zeitaufgelöste Spektroskopie an einzelnen verspannungs-induzierten Halbleiter-Quantenpunkten.* 2009.

[70] F. J. R. Schülein, A. Laucht, J. Riikonen, M. Mattila, M. Sopanen, H. Lipsanen, J. J. Finley, A. Wixforth, and H. J. Krenner. Cascaded exciton emission of an individual strain-induced quantum dot. *Applied Physics Letters*, 95(8):083122, 2009.

[71] G. Sek, P. Podemski, J. Misiewicz, L. H. Li, A. Fiore, and G. Patriarche. Photoluminescence from a single InGaAs epitaxial quantum rod. *Applied Physics Letters*, 92(2):021901, 2008.

[72] P. D. Siverns, S. Malik, G. McPherson, D. Childs, C. Roberts, R. Murray, B. A. Joyce, and H. Davock. Scanning transmission-electron microscopy study of InAs/GaAs quantum dots. *Phys. Rev. B*, 58(16):R10127–R10130, Oct 1998.

[73] R. M. Stevenson, R. J. Young, P. Atkinson, K. Cooper, D. A. Ritchie, and A. J. Shields. A semiconductor source of triggered entangled photon pairs. *Nature*, 439:179–182, 2006.

[74] J. Stotz, F. Alsina, R. Hey, and P. Santos. Acoustically induced dynamic potential dots. *Physica E: Low-dimensional Systems and Nanostructures*, 26(1-4):67 − 71, 2005. International Conference on Quantum Dots.

[75] J. Stotz, R. Hey, P. Santos, and K. Ploog. Coherent spin transport through dynamic quantum dots. *Nat Mater*, 4(8):585 − 588, 2005.

[76] I. Stranski and L. v. Krastanow. *Abhandlungen der Mathematisch-Naturwissenschaftlichen Klasse*, 146:797, 1939.

[77] M. Streibl. *Statische und dynamische Potentialgitter auf Halbleiterheterostrukturen für optoelektronische Anwendungen, Dissertation.* Ludwig-Maximilians-Universität München, 2000.

[78] M. Sugawara, K. Mukai, Y. Nakata, K. Otsubo, and H. Ishilkawa. Performance and physics of quantum-dot lasers with self-assembled columnar-shaped and 1.3-µm emitting InGaAs quantum dots. *Selected Topics in Quantum Electronics, IEEE Journal*, 6(3):462 – 474, 2000.

[79] S. Völk, A. Wixforth, D. Reuter, A. D. Wieck, and J. Ebbecke. Conversion of bound excitons to free excitons by surface acoustic waves. *Phys. Rev. B*, 80(16):165307, Oct 2009.

[80] R. J. Warburton, B. T. Miller, C. S. Durr, C. Bodefeld, K. Karrai, J. P. Kotthaus, G. Medeiros-Ribeiro, P. M. Petroff, and S. Huant. Coulomb interactions in small charge-tunable quantum dots: A simple model. *Physical Review B*, 58(24):16221–16231, 1998.

[81] R. J. Warburton, C. Schäflein, D. Haft, F. Bickel, A. Lorke, K. Karrai, J. M. Garcia, W. Schoenfeld, and P. M. Petroff. Optical emission from a charge-tunable quantum ring. *Nature (London)*, 405:926–929, 2000.

[82] C. Wiele, F. Haake, C. Rocke, and A. Wixforth. Photon trains and lasing: The periodically pumped quantum dot. *Phys. Rev. A*, 58(4):R2680–R2683, Oct 1998.

[83] Y. Zhang. Motion of electrons in semiconductors under inhomogeneous strain with application to laterally confined quantum wells. *Phys. Rev. B*, 49(20):14352–14366, May 1994.

[84] D. Zhi, H. Davock, R. Murray, C. Roberts, T. S. Jones, D. W. Pashley, P. J. Goodhew, and B. A. Joyce. Quantitative compositional analysis of InAs/GaAs quantum dots by scanning transmission electron microscopy. *Journal of Applied Physics*, 89(4):2079–2083, 2001.

Appendix A

Samples

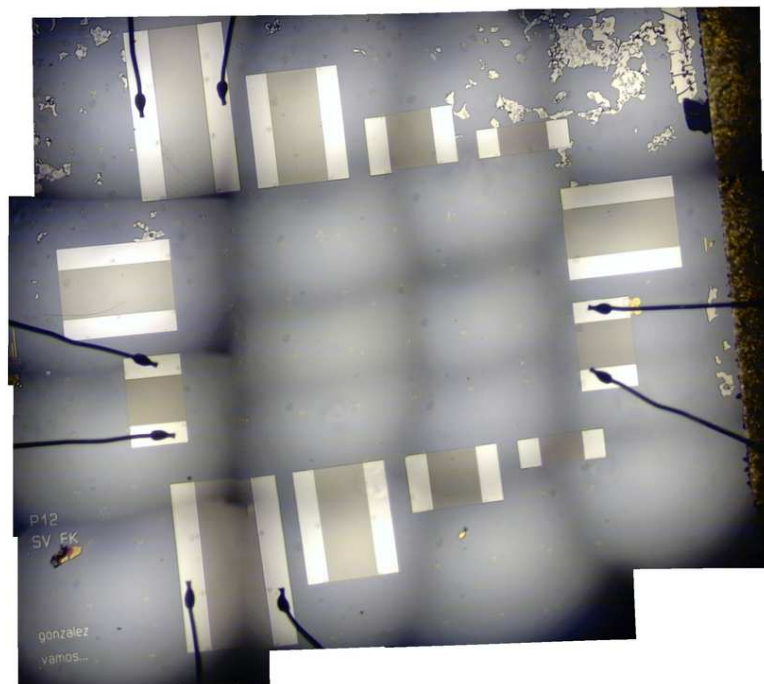| Sample name	Wafer	IDTs
P10	060809A (Santa Barbara) $d_{\mathrm{QP}} = 23$ nm	two crossing delay lines $\lambda_{\mathrm{SAW}} = 15.0$ µm
P12	060809A (Santa Barbara) $d_{\mathrm{QP}} = 23$ nm	four vertical delay lines $\lambda_{\mathrm{SAW}} = 12.5, 5.4, 3.0, 1.8$ µm two horizontal delay lines $\lambda_{\mathrm{SAW}} = 5.4, 3.0$ µm
SKQD1 (Florian Schülein)	13630 (Bochum) embedded QDs	$\lambda_{\mathrm{SAW}} = 11.6$ µm

Figure A.1: Photograph of sample P12. Several delay lines have been fabricated in a crosswise configuration allowing for the excitation of SAWs with different frequencies at identical positions on the sample.

Appendix B

Sample processing

Cleaning:
acetone (ultrasonic power 100%) 5 min.
isopropanol (rinsing)

Electron beam lithography:
lower resist: PMMA 150k 4%
upper resist: PMMA 500k 2%
spin coating: 5000 s^{-1}, 30 s
bake out: 160°C, 60 min.
aperture: 30 µm
EHT: 10 kV
dose factor: 0.8
area dose: 100 $\frac{\mu As}{cm^2}$
line dose: 300 $\frac{\mu As}{cm^2}$
dot dose: 0.08 $\frac{pAs}{cm^2}$
write field size: 400 µm x 400 µm
developing: IMBK:isopropanol [1:3], 30 s

Metallization:
HCl [1:5] dip 25 s, H$_2$O (rinsing)
Labash: 200 W, 500 mTorr O$_2$, 18 s
IDTs: 5 nm Ti, 50 nm Al
marker: 5 nm Ti, 30 nm Au

Lift off:
acetone (ultrasonic power 10%) 20 s

Appendix C

IDT parameters

f_{SAW} (MHz)	λ_{SAW} (µm)	η	N	f_{L} (MHz) for phase locking
192.9	15.0	0.5	80	64.3 ($= 1/3 f_{\mathrm{SAW}}$)
232.2	12.5	0.5	96	77.4 ($= 1/3 f_{\mathrm{SAW}}$)
251.5	11.6	0.5	80	
538.3	5.4	0.5	148	76.9 ($= 1/7 f_{\mathrm{SAW}}$)
968.5	3.0	0.3	133	74.5 ($= 1/13 f_{\mathrm{SAW}}$)

The resonance frequencies of the IDTs f_{SAW} are measured at temperatures $T < 10$ K. The transducer aperture for the IDT with period $\lambda_{\mathrm{SAW}} = 11.6$ µm is $W = 300$ µm. The aperture for the other IDTs is $W = 350$ µm$-\lambda_{\mathrm{SAW}}$.

Appendix D

Estimation of optical intensity

The laser intensities P_L quoted in this thesis are absolute values. The laser intensity P_L is the value taken from the power meter multiplied by a conversion factor c_L taking into account different intensities at the power meter and on the sample surface (see also setup diagram 3.1). The absolute intensities P_L are not comparable for different experimental setups, e.g. different lasers or different microscope magnifications. Therefore, an other parameter, the optical intensity, is introduced providing comparable intensities for different experimental configurations. The optical intensity I_L is the optical power per unit area.

The intention of this appendix is to give an estimate for the optical intensity I_L. To this end, the diameter of the laser spot must be known. In the left panel of figure D.1, luminescence originating from the matrix-QW is displayed spatially resolved. Since the QW is extended over the entire sample, its PL is a direct measure of the incoming laser intensity. In the right panel, a cross section of the grey scale plot is shown, as indicated by the dotted blue line. A gauss curve is fitted to the intensity profile and the standard deviation σ is calculated from the fit. The mathematical properties of the Gaussian curve reveal, that 68.3 % of the incoming laser intensity is deposited within the radius σ. Thus, the optical intensity is:

$$I_\mathrm{L} = \frac{0.683 P_\mathrm{L}}{\pi \sigma^2} \tag{D.1}$$

In the particular example, the laser intensity is $P_\mathrm{L} = 76$ nW which is a typical value used for the SAW experiments. For this intensity, a standard deviation of $\sigma \approx 2.5$ µm is obtained. Therefore, the average optical intensity within σ is $I_\mathrm{L} = 2600$ W/m^2 (0.26 W/cm^2). It should be noted that this is an estimate for a particular laser intensity P_L and that the radius σ depends also on P_L.
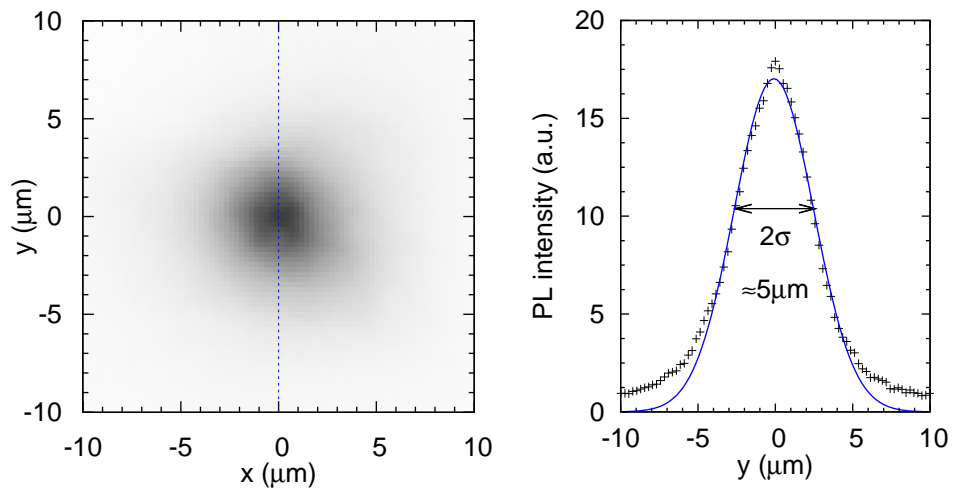
Figure D.1: Matrix-QW luminescence excited by laser *LDH-P-660, PicoQuant* ($\lambda_\mathrm{L} =$ 661 nm, $P_\mathrm{L} = 76$ nW, $f_\mathrm{L} = 80$ MHz). Left panel: PL recorded in image mode, 0th order of diffraction. Right Panel: Intensity profile at the center of the laser focus (blue dotted line in left panel) and Gaussian fit.

Appendix E

List of variables

variable	description
α	SAW amplitude
$B(f)$	susceptance
β	polarizability
C_{IDT}	IDT capacitance
c_{In}	Indium concentration
c_{L}	conversion factor for laser intensity
c_i^+, c_i	creation, annihilation operator for electron
D_{c}	number of confined directions
D_{f}	degrees of freedom
D_{L}	diameter of laser spot
D_{QD}	QD diameter
D_{QP}	QP diameter
d_{QD}	QD height
d_{QP}	QP height
d_{QW}	QW width
d_i^+, d_i	creation, annihilation operator for hole
Δd	spatial distance
ΔE	energy shift
$\Delta \phi$	difference between phases
ΔT_{L}	laser pulse (duty cycle)
ΔT_{prop}	SAW propagation delay
ΔT_{SAW}	SAW pulse (duty cycle)
Δt	time interval
Δt_{L}	laser pulse width
E	(PL) energy
E_{b}	binding energy
$\mathbf{E}_{\parallel}$	lateral component of piezoelectric field
$\mathbf{E}_{\perp}$	vertical component of piezoelectric field
F	electric field
f_{c}	center frequency
f_{L}	laser repetition frequency (pulsed laser)
f_{rep}	repetition frequency duty cycle

f_{SAW}	SAW frequency
ϕ	phase
$G(f)$	radiation conductance
H	Hamiltonian
η	metallization ratio
I_{L}	optical intensity
l, m	quantum numbers
$\mathbf{k}$	wave vector
k_{SAW}	SAW wave vector
L	angular momentum
l_x, l_y, l_z	dimensions of nanostructures
λ	PL wavelength
λ_{L}	laser wavelength
λ_{SAW}	SAW period
M	optical magnification
m^*	effective electron mass
N	number of finger pairs
NA	numerical aperture
n_x, n_y, n_z	quantum numbers
P_{av}	available power
P_{L}	laser intensity
P_{SAW}	acoustic power
P^-	polarization operator for annihilation
$\mathbf{p}$	dipole moment
R_{g}	source impedance
r_{B}	exciton Bohr radius
$S(\omega)$	probability for optical transition
σ	standard deviation, laser spot size
T	temperature
T_0	trigger delay for SAW
T_{int}	time interval for integration
T_{SAW}	SAW period
τ	relaxation time
$\mathbf{u}_{\parallel}$	lateral displacement
$\mathbf{u}_{\perp}$	vertical displacement
V	electronic potential
V_{xy}	interparticle interaction potential
V_{s}	source voltage
V_{IDT}	voltage across IDT
v_{SAW}	SAW velocity
W	transducer aperture
Y	complex admittance
Ψ	Schrödinger wave function
Z	complex resistance
Ω	oscillator energy
ω_{SAW}	SAW angular frequency

Danksagung

Ein herzliches Dankeschön an alle, die zum Gelingen dieser Arbeit beigetragen haben! Mein besonderer Dank gilt:

Lebenslauf

Stefan Völk, geboren am 10. Januar 1978 in Augsburg.

1984-1988	Grundschule Usterbach
1988/89	Hauptschule Dinkelscherben
1989-1998	Ringeisen-Gymnasium Ursberg
1998/99	Zivildienst im Marienheim Baschenegg
1999-2005	Studium der Physik an der Universität Augsburg
2006	Wissenschaftlicher Mitarbeiter am
	Instituto de Microelectrónica de Madrid (IMM,CSIC)
2007-2010	Wissenschaftlicher Mitarbeiter am Lehrstuhl für
	Experimentalphysik I, Universität Augsburg